11-6-2018

A Systematic Investigation of Condensation Heat Transfer Using Asymmetric Micro-Scale Surfaces

Emily Brown
Louisiana State University and Agricultural and Mechanical College

A SYSTEMATIC INVESTIGATION OF CONDENSATION HEAT TRANSFER USING MICROSCALE ASYMMETRIC SURFACES

A Thesis

Submitted to the Graduate Faculty of the
Louisiana State University and
Agricultural and Mechanical College
in partial fulfillment of the
requirements for the degree of
Masters of Materials Science and Engineering

in

The Department of Mechanical and Industrial Engineering

by
Emily Elizabeth Brown
B.S. Southeastern Louisiana University, 2014
December 2018

Acknowledgments

I would like to acknowledge Dr. Sunggook Park for constructive criticism and unyielding patience in all of my graduate study endeavors as well as my committee members Dr. Murphy, Dr. Schoegl, and Dr. Gartia for helping make this thesis possible.

I would like to thank my colleagues, Dr. Junseo Choi, Mohammad Beheshti, and Zheng Jia for the countless hours of discussions and helpful guidance in scientific research and sometimes even life.

This work would not have been possible without the aid of the LSU professors who have persistently pushed me in my studies and thirst for knowledge.

Most of all, I need to extend my deepest and most sincere gratitude to my friends and family who have always seen the best in me even when I couldn't.

This thesis is partial supported by Chevron assistantship and NASA GSRA fellowship.

Table of Contents

List of Figures

Abstract

Asymmetric surfaces been shown to inducing unidirectional motion in the Leidenfrost regime; however, very minimal research has been conducted to investigate whether these surface can enhance condensation through the same means. The investigation of heat transfer of ratchets in condensation is a relatively untapped area of study, specifically ratchets with superhydrophobic properties. Anticipated difficulty lies in creating surfaces features or coatings that retain the ratchets and can adequately sustain optimal wetting state of Cassie-Baxter required to improve heat transfer performance during condensation. This study serves to investigate whether ratchets are a feasible surface feature to enhance condensation heat transfer.

First, fabrication protocols for microscale superhydrophobic asymmetric structures with high throughput and at low cost are devised. Then, droplet behavior during condensation is directly observed under an optical microscope and quantified. Finally, heat transfer is performance is investigated using a custom built chamber and a liquid crystal thermography technique.

Superhydrophobic coating reduced the droplet area coverage by about 25% as well as reduced the average droplet area which remained consistent regardless of ratchet period,. For non-ejected coalescence, displacement vectors showed a slight increase in preferring either ratchet direction or opposite of ratchet direction with increasing ratchet period. In the case of coalescence induced ejection, average ejection diameter remained constant at approximately 10um yet event count increased with increasing ratchet period seemingly attributed to the increased potential configurations due to the increased ratchet surface area. No individual droplets were readily identified using the surface plots extracted from MatLab image processing, however heat transfer coefficients were found and showed a trend opposite to what was anticipated. Uncoated PMMA without ratchets yielded the highest HTC and the coated 10um ratchets yielded the lowest.

Potential investigations into surface manipulation without the use of coatings can eliminate the added thermal resistance potentially produced by the coating itself, this would also eliminate the need to have a strong bonding between the substrate surface and the coating eliminating a source of mechanical instability. Finally, improvements to the condensation chamber design can be made, specifically including a reservoir in which the flow rate of vapor that the substrate is exposed to can be controlled.

Chapter 1. Introduction

1.1. General Background

Heat transfer due to phase change from vapor to liquid is a widely used phenomenon in everyday life, specifically in industrial applications involving energy, thermal management, water harvesting, as well as filtration systems. To reap the benefits; specifically, low cost and high throughput, scientists have continuously studied how to enhance heat transfer in these applications. It was realized early on (Rose, Dropwise condensation theory and experiment: a review, 2002) (Schmidt, Schurig, & Sellschopp, 1930) that dropwise condensation performance proves superior compared to film-wise due to the lower thermal resistances compared to the liquid films. Lower resistance allows for more rapid condensation cycles of nucleation, growth, and departure (also referred to as sweeping); consequently, improving one or all of these stages will improve heat transfer. One controllable parameter is droplet departure which entails inducing and catalyzing coalescence events. The most rapid form of coalescence events achievable is characterized by spontaneous droplet removal or jumping droplets. Condensate micro-drop self-propelling (CMDSP) (Zhu, Luo, Tian, Li, & Gao, 2015), (Boreyko & Chen, Vapor Chambers with Jumping-Drop Liquid Return from Superhydrophobic Condensers, 2013) (Boreyko, Zhao, & Chen, Planar Jumping-Drop Thermal Diodes, 2011) (Miljkovic N. , et al., 2013) (Hou, Yu, Chen, Wang, & Yao, 2015) surfaces enable departure of small-scale condensates due to the spontaneous release of surface energy in the absence of external forces. These surfaces have the potential to be used along with asymmetric surface features, which have been shown to induce unidirectional motion to allow for a more controllable droplet motion (Boreyko, Zhao, & Chen, Planar Jumping-Drop Thermal Diodes, 2011) (Brumfield, 2014) (Chamakos, Karapetsas, & Papathanasiou, 2016) (Comanns, et al., Direction, passive liquid transport: the Texas horned lizard as a model for a biomimetic 'liquid diode', 2015) (Daniel &

Chaudhury, 2002) (Guo, Zheng, Liu, Ju, & Jiang, 2012) (Ok, May 2011) (Yu, 2014). Potential applications include thermal management, power generation, water harvesting, desalination, and general heating and cooling. Understanding how these surfaces behave both on the droplet scale as well as the global scale is necessary in extracting the full potential of these surfaces.

1.2. Goals and Objectives

The goal of this study is to systematically investigate the feasibility of using a passive mass transport technique in the form of asymmetric surfaces, to increase the rate of coalescence in a unidirectional manner.

The objectives to achieve this goal are as follows:

1. Devise a fabrication process to produce microscale ratchets on large area substrates (cm scale) with various ratchet periods using combined UV and thermal imprinting along with a technique that will improve the wetting behaviors of these substrates.
2. Investigate liquid droplet behavior and quantify heat transfer on various wetting and non-wetting ratchet periods.
3. Reveal the relationship between coalescence behavior and ratchet period and correlate to heat transfer coefficients.

This study is subdivided into 6 chapters. Chapter 2 contains the literature reviews of the background information of condensation heat transfer, superhydrophobic surfaces, and asymmetric surfaces or passive transport mechanisms. Following in Chapter 3, the fabrication process which involves optical grating replication using UV imprinting followed by stamp fabrication using thermal imprinting is outlined as well as a dip coating technique for creating superhydrophobic microscale ratchets on PMMA substrates. Here, the experimental setup for

direct observation of condensation behavior using an optical light microscope is discussed as well.) Chapter 4 involves essentially two methods of surface characterization, observation using scanning electron microscope or SEM and characterization of wetting behavior via contact angle analysis. Chapter 5 is broken down into sections pertaining to how coating and ratchet period influences droplet size, area coverage, ejection events, coalescence without ejection, and the displacement of droplets after coalescence. In chapter 6, condensation experiments results using liquid crystal thermography are discussed. The fabrication of a custom built condensation chamber inspired by (Bansal, Khandekar, & Muralidhar, 2009) is detailed as well as the calibration procedure followed by the data processing of hue to temperature transformation. Using the calibration data, information regarding temperature distribution is extracted in Chapter 7 and used to find the heat transfer coefficient or HTC performance of treated and untreated substrates with and without ratchet surface feature. Following the discussion of HTC, surface wetting behavior variations due to exposure to a condensing environment is investigated and discussed. Finally, Chapter 8 states the conclusions and discusses potential future works regarding different techniques in creating superhydrophobic surface as well as improvements that can be made to the custom condensation chamber.

Chapter 2. Literature Survey

2.1. Introduction

This study focuses on droplet coalescence and heat transfer behavior on wetting and non-wetting microscale PMMA ratchets. Droplet coalescence behavior is observed in condensation conditions, where the substrate is at a lower temperature than the ambient surroundings. The heat transfer quantifications are done in a controlled environment still in the saturated vapor. In order to understand and further analyze the behavior of condensation on microscale ratchets, in depth surveys on a broad field of topics is required such as fundamentals of condensation heat transfer, superhydrophobic wetting behaviors, as well as passive transport mechanisms associated with ratchets. This chapter provides a summary of such literature surveys.

2.2. Condensation

When a surface is at a lower temperature than the saturation temperature of a vapor, a phase change can occur. The vapor will change from a gaseous form into a liquid. In this case, there are two specific types of condensates that can form, either filmwise or dropwise. Filmwise condensation is characterized by the liquid wetting the entire surface and forming a film, whereas dropwise condensation produces spherical or nearly spherical droplets. The heat transfer behaviors of these two types differ, with dropwise condensation being the more efficient of the two due to the rapid departure from the condensing surface (Schmidt, Schurig, & Sellschopp, 1930), (Rose, Dropwise condensation theory and experiment: a review, 2002). As film thickness or droplet sizes for respectively film and dropwise condensation increases, so does the thermal resistance and subsequently the capability to transfer heat between the vapor and the surface of interest. In summary, promotion of dropwise condensates with relatively small droplet sizes proves to be favorable in heat transfer. When heat transfer rates are optimized for

condensation applications such in the case of a condenser, significant savings in natural resources and energy can occur due to enhanced efficiency of condenser surfaces saving fuel and minimizing potentially harmful emissions. The difficulty lies in maintaining dropwise condensation for long-term operating periods especially for high sub-cooling conditions.

2.2.1. Dropwise Condensation

Dropwise condensation mode first studied in the 1930's, (Schmidt, Schurig, & Sellschopp, 1930) produces a significantly larger (5 to 7 times) heat transfer coefficient compared to that of filmwise condensation. From 1960-1980 (Rose, Dropwise condensation theory and experiment: a review, 2002) measurements involving the presence of air in steam were identified as potential sources of data error showing that dropwise condensation had lower heat transfer coefficient compared to filmwise condensation, demonstrating the importance of purging the testing environment of non-condensable gases (NCGs). Another source of difficulty is finding a promoter that can withstand the high demands of industrial applications, specifically longevity in harsh environments. Initially, layers of polytetrafluorethylene (PTFE) showed excellent promise with the exception of durability; when thickness is increased so is the thermal resistance of the surface. Surfaces with monolayers, for example dioctadecyl disulphide on copper, have only proved useful for a manner of hours rather than days. Miljkovic et al. showed increases of 30% and Hou et al. showed further improvement to 63% higher heat transfer rates. The most significant note of improvement is by Zhu et al. improving heat transfer coefficient by 125%. The significant increase can be attributed to several factors including high density nucleation sites, low surface adhesion, and small droplet size maintained over time. The most common mechanism for droplet removal is gravity and this depends on the orientation of the substrate, the drawback however, is that droplet diameter is comparable to capillary length. Allowing droplet

growth the capillary length scale can induce unwanted thermal resistance, for this reason research focus has shifted towards removal of micro-drops.

2.2.2. Jumping Droplets

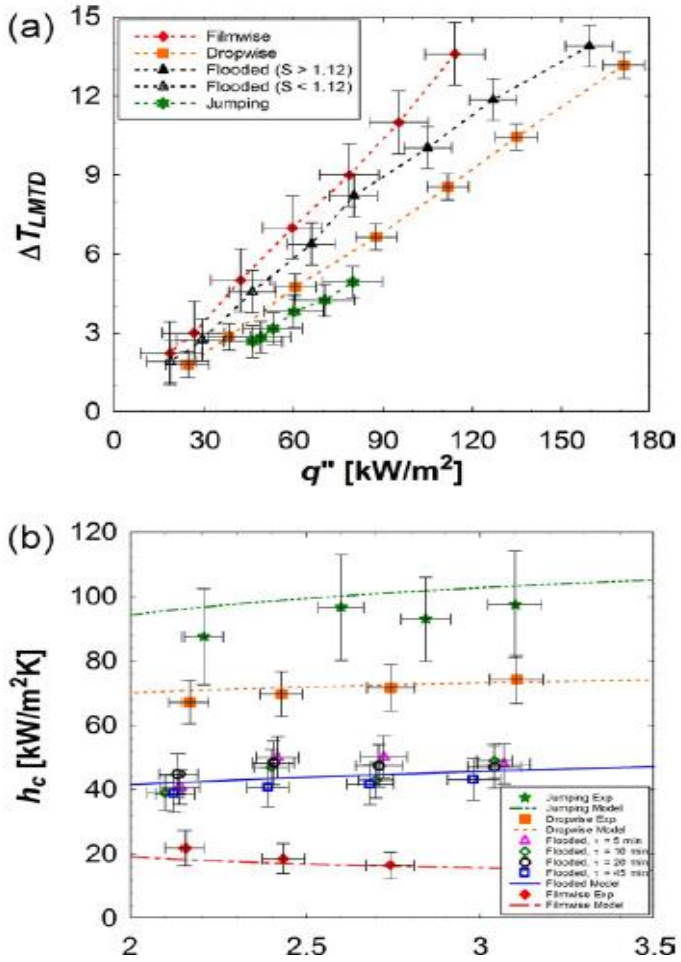

Figure 1. Heat transfer performance as a function of supersaturation and vapor pressure a) characterization of various condensing behaviors as a funciton of heat flux and log mean water to vapor temperature difference. b) experimental and theoretical steady state condesation coefficent measured as a function of vapor pressure (Miljkovic N. , et al., 2013).

Steady state conditions for dropwise condensation with droplet removal aided by gravity typically have droplet diameters above 100μm (Rose, Dropwise condensation theory and experiment: a review, 2002). Condensate micro-drop self-propelling (CMDSP) surfaces are capable of efficient self- departure of small or micro-drops (~10-100μm) (Miljkovic, Enright, &

Wang, 2012) without requiring external forces such as gravity or steam shear force. (Luo, Li, Zhu, Zhao, & Gao, 2015). These self-propelling droplets are also referred to as jumping droplets and typically have droplet ranges $\geq 10\mu m$ (Boreyko & Chen, 2009). The jumping behavior is a result of the release of excess surface energy. Such behavior is possible on surfaces with nanostructures with surface roughness in the range of 100nm (Miljkovic, Enright, & Wang, 2012) which allows a reduced adhesion beneath coalescing droplets through minimization of solid fraction and asymmetry of droplet coalescence (Miljkovic N. , et al., 2013). Through rapid coalescence induced ejection, there are an increased number of small droplets which can more efficiently transfer heat from the surface (Glicksman & Hunt, 1972), (Graham & Griffith, 1973), and (Rose, On the Mechanism of Dropwise Condensation., 1967). The benefit of promotion of jumping droplets becomes evident when observing the results of (Miljkovic N. , et al., 2013) in Figure 1 due to the higher heat transfer performance; however, this is only realized at lower heat fluxes. At higher heat flux values, the behavior transitions from jumping to a sticky Wenzel state and is not reversible. As Miljkovic N., et al. stated "once flooding initiated, reduction of the supersaturation did not revert the behavior to droplet jumping". Where the "S" denotes the ratio of vapor pressure divided to the saturation pressure at the specific sample surface temperature. When the vapor pressure is varied (shown in Figure 1b), jumping droplets still maintain the higher heat transfer coefficient. It is also worth noting that with changing pressure, the heat transfer coefficients remain relatively constant for all forms of condensation shown. The various modes observed are shown clearly in Figure 2, arguably with the exception of the noticeable variations between flooding and dropwise (at least at the image scale presented). The variation stated is the larger average droplet size resulting in an approximate 40% lower heat transfer (Miljkovic N. , et al., 2013).

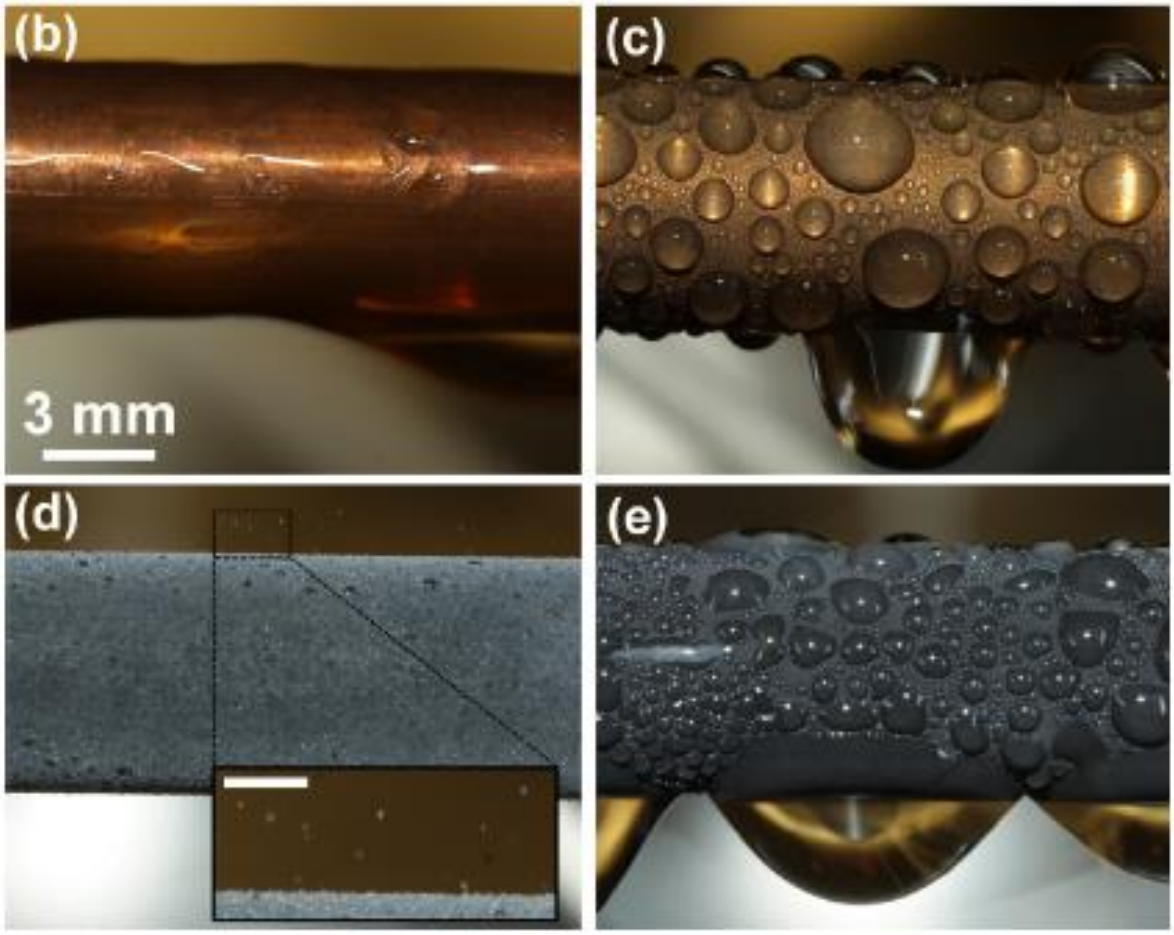

Figure 2. Wetting modes demonstrated by (Miljkovic N. , et al., 2013) b) filmwise condensation on smooth hydrophilic Cu tube c) dropwise condensation on Silane coated smooth Cu tube d) jumpingdroples on nanostructed CuO tube (inset of jumping phenomena, scale bar is 500 um) e) flooded condensation on nanostructured CuO tube.

These high heat transfer rates are achieved on metallic substrates. However; there are studies that do consider enhanced condensation properties on polymers. The interest in polymers lies in ease of production in the proof-of-concept phase. Primary methods of promoting dropwise condensation on polymers involve coating with organic compounds (Tanner, Potter, Pope, & West, 1965) (Tanner, Pope, Potter, & West, 1965), nanostructures via nanolithography or imprinting (Chen, et al., 2007), and use of self-assembly monolayers (Vemuri & Kim, An experimental and theoretical study on the concept of dropwise condensaiton, 2006) (Vemuri, Kim, Wood, Govindaraju, & Bell, 2006).

2.2.3. Thermal Resistance in Single Droplet

To increase heat transfer, it is beneficial to minimize if not eliminate thermal resistances. According to (Hu & Tang, 2014), heat transfer resistance can be broken down into two parts: resistance through the droplets independent of size and resistance through the condensate film. This reference concludes that for single droplet, temperature drop due to interfacial resistance of the vapor and fluid and the thermal resistance through the droplet itself are related to the contact angle. More explicitly small droplet radius coupled with a large contact angle can produce high

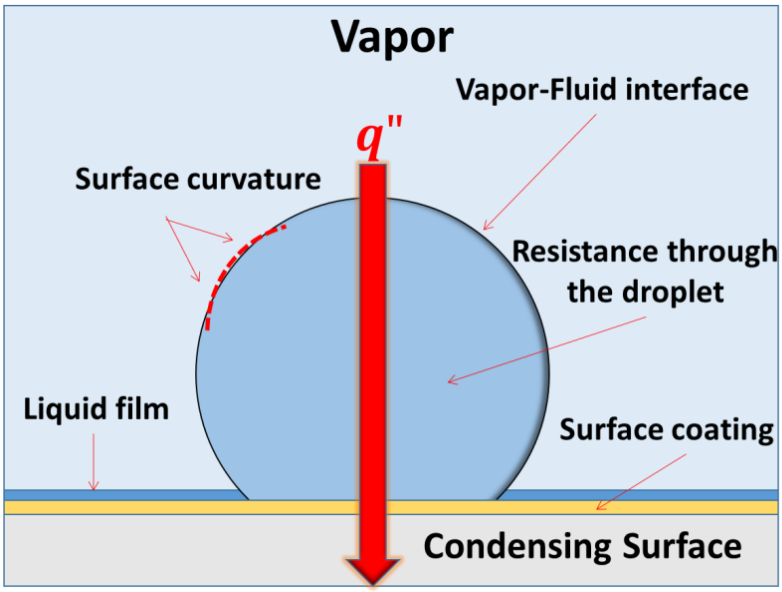

Figure 3. Thermal resistance associated with a single droplet on a condensing surface.

heat transfer resistance. Illustrated in Figure 3 are thermal resistance variables that can be manipulated: coating thickness, the presence of a liquid film, surface curvature, and liquid properties.

In terms of surface fabrication, minimization of thermal resistance due to surface coating is of primary interest simply because it is the easiest to control, this can also affect the presence or more beneficially, the absence of a liquid film. The larger the droplet, the greater the cumulative thermal resistance due to the interface and the amount of liquid contained within the droplet are.

Surface coating can directly affect the maximum achievable droplet size, if the surface adhesion force is low, droplets will coalesce more rapidly and thus leave the surface at a faster rate improving the efficacy of heat transfer.

2.2.4. Measuring Heat Transfer

Primary means of measurement of heat transfer involve temperature difference between surface of interest and the vapor and heat flux. Most literature plot heat transfer coefficient against the driving force, i.e. the temperature difference; where the heat transfer coefficient is not constant for dropwise condensation due to the fact that heat flux is not proportional the temperature gradient.

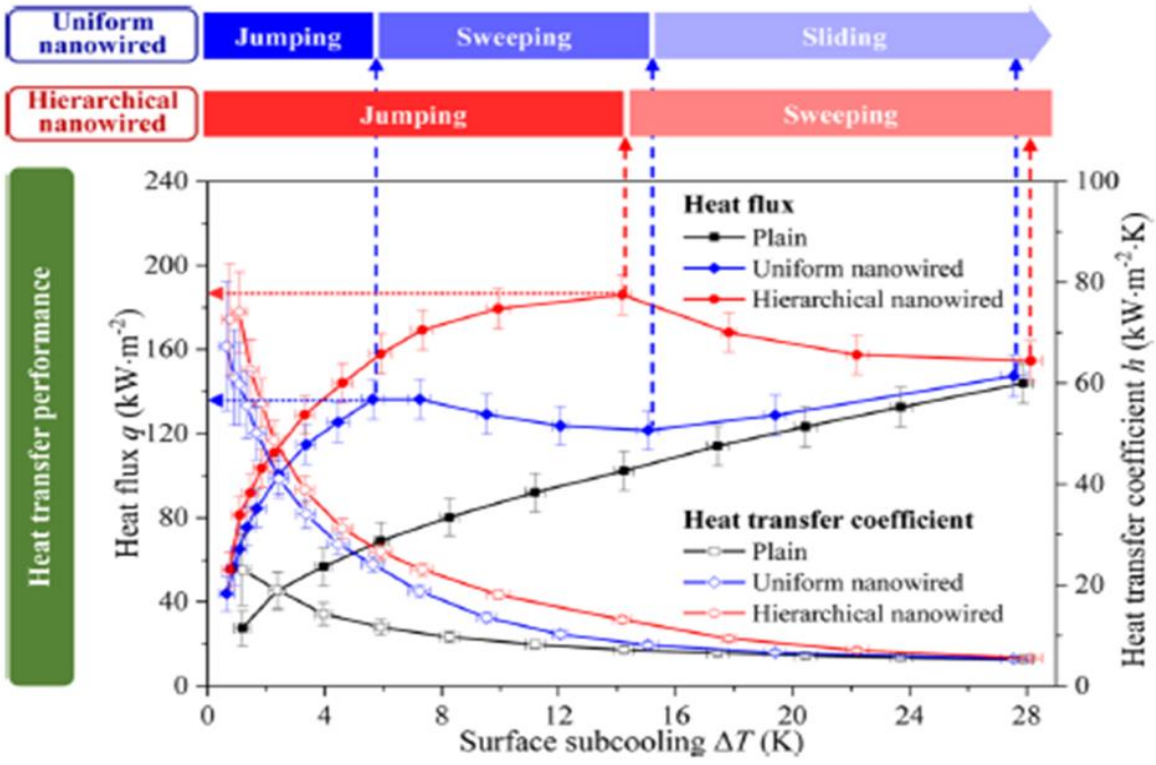

Figure 4. Results of (Wen, et al., 2017) showing the effect of subcooling on HTC and heat flux various treated substrates.

In the occurrence of dropwise condensation, the temperature gradient is relatively small and in some cases, comparable to the degree of error this can results in inappropriate interpretations

when “plotting a quantity involving its reciprocal” (Rose, Dropwise condensation theory and experiment: a review, 2002) . In most cases, the heat flux is the adjusted quantity, usually controlled by flow rate, and the temperature difference is the measured quantity. Some literature sources show conflicting results but this is potentially due to the variations in how the surfaces are treated. Wen et al. show a higher heat transfer coefficient for superhydrophobic surfaces containing hierarchical nano-wires made of copper, with the highest achievable value at low subcooling temperatures (Wen, et al., 2017).The results for which are displayed in Figure 4. These results more explicitly show that superhydrophobic surfaces with hierarchical nanowires structures retain higher heat transfer rates over a plain hydrophobic surface and the uniformed nanowire surface due their ability to spatially control nucleation. Hwang et al. result in Figure 5 show a different behavior for superhydrophobic surfaces created on zirconium alloy plates which were modified by anodic oxidation and sanding (Hwang, et al., 2016). It is observed that

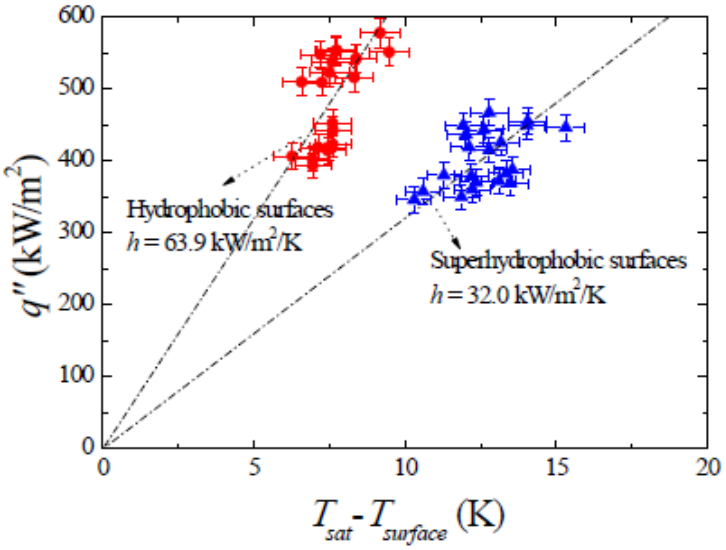

Figure 5. Heat transfer coefficient achieved through sticky nucleation sites on superhydrophobic surfaces fabricated by (Hwang, et al., 2016).

these surfaces have sticky nucleation sites, which would allow droplets to grow to sizes larger

than that the Wen et al. group. These two sources alone show the strong dependence of heat transfer on the droplet nucleation behavior.

The presence of non-condensable gases introduces a layer of thermal resistance affecting the surface temperature difference. Contributing factors include the geometry of the housing environment, the amount of gas present and how it vented, along with the condensation rate. (Rose, Dropwise condensation theory and experiment: a review, 2002) Ideally, the heat transfer coefficient increases with the increasing difference between vapor and surface temperature. This is due to the increase in active nucleation sites. Heat transfer coefficient is also measured as a function of pressure, with the trend showing decreasing HTC with decreasing pressure. (Rose, Dropwise condensation theory and experiment: a review, 2002)

2.2.4.1. Liquid thermal Crystals: Imaging technique

Heat transfer measurement techniques traditionally consist of thermocouple measurements in a controlled environment (Cheng, Vandadi, & Chen, 2012), (Lee, Cheng, Palmre, Bhuiya, & Kim, 2013), (Xiao , Milijkovic, Enright, & Wang, 2013). The use of thermocouples makes the assumption that the condensing surface is behaves isothermally and the temperature of the substrate/ condensing surface is often extrapolated from temperature gradients in the normal direction from thermocouples located somewhere normal to the surface these calculations yield averaged condensation heat transfer coefficients and cannot inherently provide local measurements. For surfaces with microscale features, this conventional technique makes spatial temperature profiles difficult, if not impossible to obtain. To provide spatial data on temperature distribution liquid crystal thermography has shown to be a promising technique (Bansal, Khandekar, & Muralidhar, 2009), (Rao & Xu, Liquid Crystal Thermograpy Measurement Uncertainty Analysis and Its Application to Turbulent Heat Transfer

Measurements, 2012) and (Kakade V. U., Lock, Wilson, Owen, & Mayhew, 2009) , an example of which is shown in Figure 6.

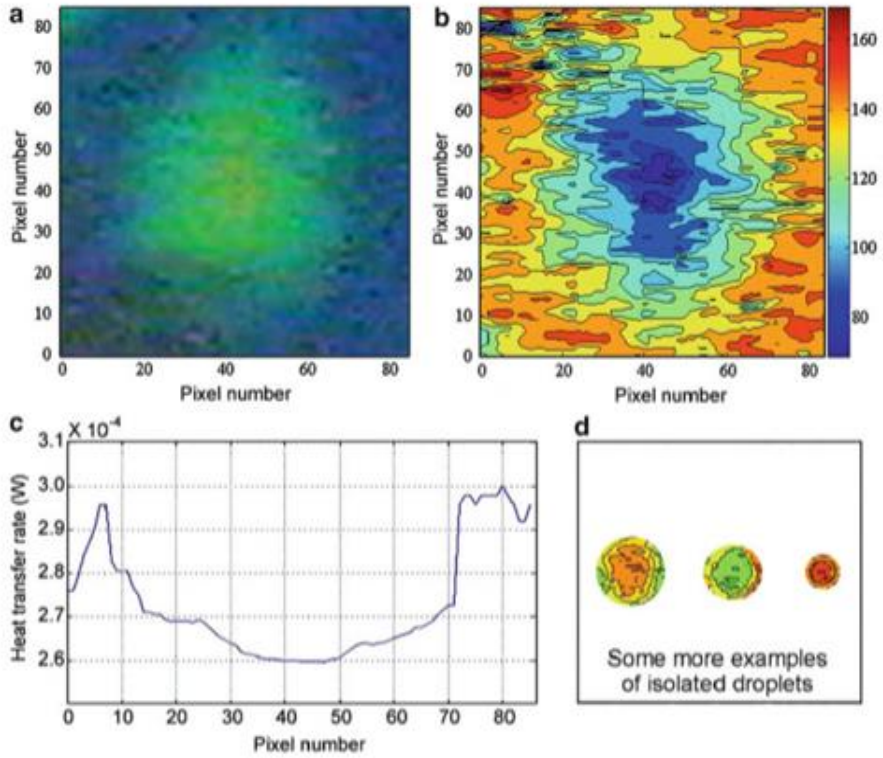

Figure 6. Post processing used by Bansal et al. a) the direct image captured from the CCD camera, b) the processed hue contour plot, c) heat transfer rate along the center horizontal of the droplet, and d) hue distributions of isolated droplet.

To investigate the condensation behavior of all fabricated surfaces a custom chamber was fabricated based on the design by Bansal et al. (Bansal, Khandekar, & Muralidhar, 2009). Conventional thermal measurement cannot provide spatial information of temperature distribution. Consequently, more accurate measurements are needed to show consistency of heat transfer measurement in dropwise condensation. Bansal et al. (2009) used liquid crystal thermography (LCT) for this purpose in hopes of providing a more accurate description of temperature distribution in dropwise condensation. Bansal et al. used a liquid thermal crystal

technique on single condensate droplet with diameters in the range of 2mm to visualize the temperature distribution on the backside of a substrate.

Liquid thermal crystals (LTC), otherwise known as cholesteric liquid crystal, change orientation at different temperatures, which results in reflection of different wavelengths and commonly display variations of the RGB color band (Rao & Xu, Liquid Crystal Thermography Measurement Uncertainty Analysis and Its Application to Turbulent Heat Transfer Measurements, 2012). This is an inexpensive and highly versatile technique for 2D visualization of temperature distributions. Bandwidth (active temperature range) can range from 1℃ to 20℃ with relatively rapid response times of about 3ms (Ireland, Neely, Gillespie, & Robertson, 1999). Since microencapsulated LTC is the most stable, it is one of the most widely used forms; however, the LTC can be directly spray coated onto a region of interest (Rao & Xu, Liquid Crystal Thermography Measurement Uncertainty Analysis and Its Application to Turbulent Heat Transfer Measurements, 2012).

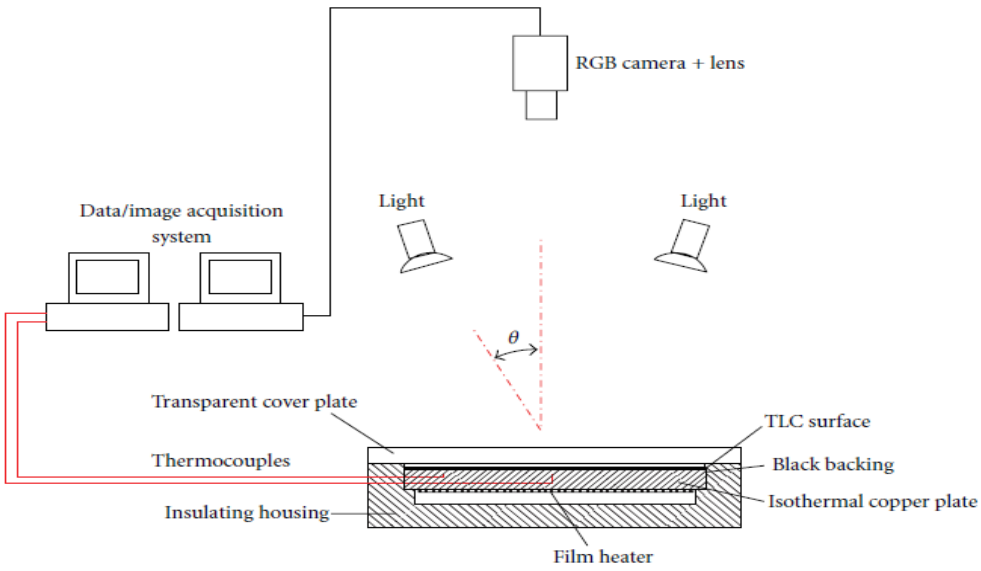

Figure 7. Example of a calibration setup for an LTC (Rao & Xu, 2012).

Since wavelength is highly dependent on light interactions, proper and consistent lighting plays a vital role. Experiments have been conducted to determine the effects of viewing and lighting angle on the calibration curve and conclude that there is significant dependence (Kakade V. U., Lock, Wilson, Owen, & Mayhew, 2009). These factors are depicted in Figure 7. This specific experiment shows that a direct view, lighting angle close to 0 will not produces shifts in the hue temperature relationship. This effect was not observed for narrow band crystals (those with activation ranges of 1℃) but rather only for wide bands (activation ranges of 5-20℃). Normalizing the temperature allows the hue curve to collapse irrespective of lighting angle, illustrating that if the normalized temperature is not used then lighting angle must be kept constant.

Hay and Hollingsworth (Hay & Hollingsworth, 1998) established a prominent procedure for calibration using hue and angle and a dimensionless temperature. The difficulty with LTC is establishing a relationship between image pixel identity/color and the corresponding temperature. Hue angle, the polar space which is determined by RGB (red green and blue color space) intensities, is one method that many researchers have used consistently, yet there can be many variations to this method alone due to variations in definitions of hue. According to Hay and Hollingsworth (Hay & Hollingsworth, 1998) (2. 1 "yields the lowest average uncertainty while retaining computational simplicity". Where h is the hue angle, and G, B, and R represent the green, blue, and red intensities respectively.

(2. 1)

$$h = \arctan\left(\frac{\sqrt{3}(G-B)}{2R-G-B}\right)$$

First, the liquid thermal crystals must be calibrated, to establish a relationship between hue and measured temperature. This calibration step is done by heating an isothermal block and the back side of the liquid thermal crystal is measured using a calibrated K-type thermal couple (Kakade V. U., Lock, Wilson, Owen, & Mayhew, 2009), (Hay & Hollingsworth, 1998),and (Baughn,

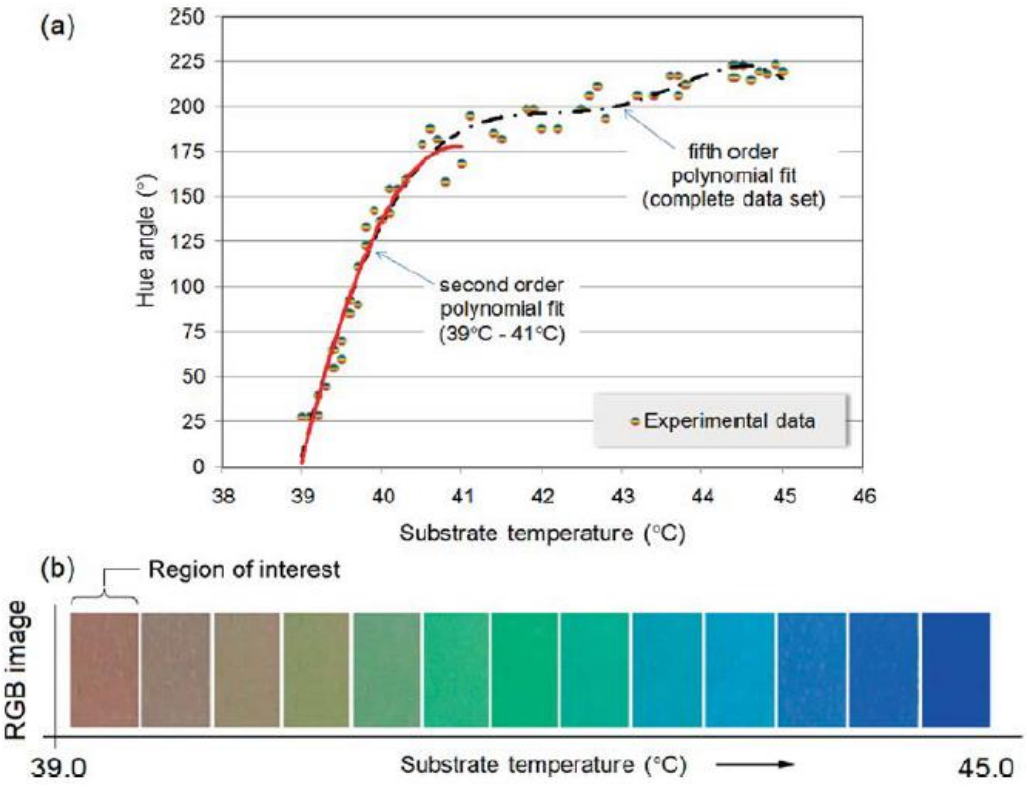

Figure 8. Calibration curve and RGB images for the activation range of liquid thermal crystals (Bansal, Khandekar, & Muralidhar, 2009) a) hue to temperature conversion showing polynomial fits for portions of the curve b) the variations of RGB intensities as temperature changes for liquid thermal crystals **.**

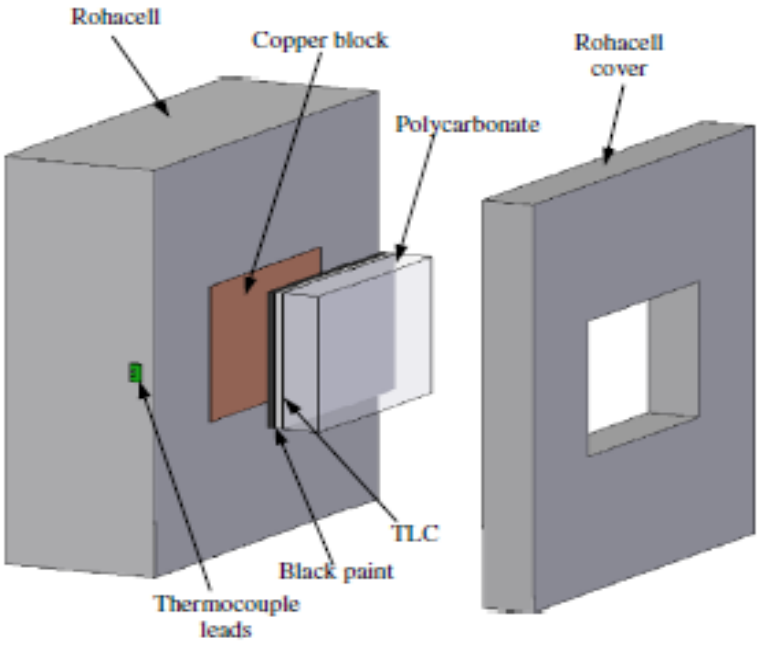

Figure 9. Example calibration setup for liquid crystal thermography (Kakade V. U., Lock, Wilson, Owen, & Mayhew, 2009)

Anderson, Mayhew, & Wolf, 1999) using an experimental setup similar to that in Figure 9. Calibration is conducted in a dark room with uniform illumination at a given angle and images are recorded using a CCD camera at a known angle. Images are then processed using any imaging process technique, for example, Matrox MAGIC-Color imaging board (Hay & Hollingsworth, 1998) or MATLAB (Kakade V. U., Lock, Wilson, Owen, & Mayhew, 2009)[1]. For the calibration purposes, the images are sectioned into 50x50 pixels at the image center to minimize the potential effects due to variations in surface thickness. A median filter is applied on individual RGB channels to replace the value individual pixel values with the median values of its surroundings. The filtered RGB image is then converted to hue and then averaged over the 50x50 pixel area. The calibration data will yield results similar to those in Figure 8 inset a which shows a fifth order polynomial behavior for the entire dataset range. This relationship is used to directly convert hue to temperature under any experimental conditions the substrate may be

[1] Followed method outlined by (Baughn, Anderson, Mayhew, & Wolf, 1999)

subjected to with the requirement that light source and angle remain constant as well as viewing angle remains constant.

2.3. Superhydrophobic Surfaces

Surface properties of a substrate, specifically wettability, can be manipulated via chemical or

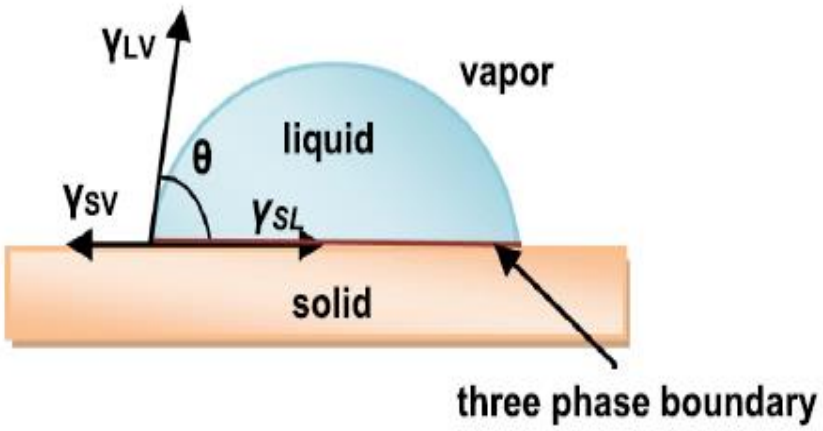

Figure 10. Interfacial tension of a droplet on a substrate (Celia, Darmanin, Givenchy, Amigoni, & Guittard, 2013).

physical texturing to create a wetting behavior tailored to the application of interest. The primary means of measuring the wettability of a surface is the static and dynamic contact angle; this can be directly related to interfacial tension at any boundary (outlined in Figure 10) via Young's equation:

(2. 2)

$$\cos\theta = \frac{(\gamma_{SV} - \gamma_{SL})}{\gamma_{LV}}$$

Where, $\gamma_{SV}, \gamma_{SL}, \gamma_{LV}$, and θ refer to the interfacial energy of the solid-vapor, solid-liquid, and the liquid-vapor regions respectively and finally the contact angle. Generally, if a surface has low wettability the static contact angle is less than 90°; these surfaces are hydrophilic. Hydrophobic surfaces are typically within the range of $90° - 150°$ and the boundaries are further pushed with superhydrophobic surfaces in which contact angles can exceed 150° with a sliding angle less than 5° (Zhang & Lv, 2015). Arguably, the most important measurement for surface wettability

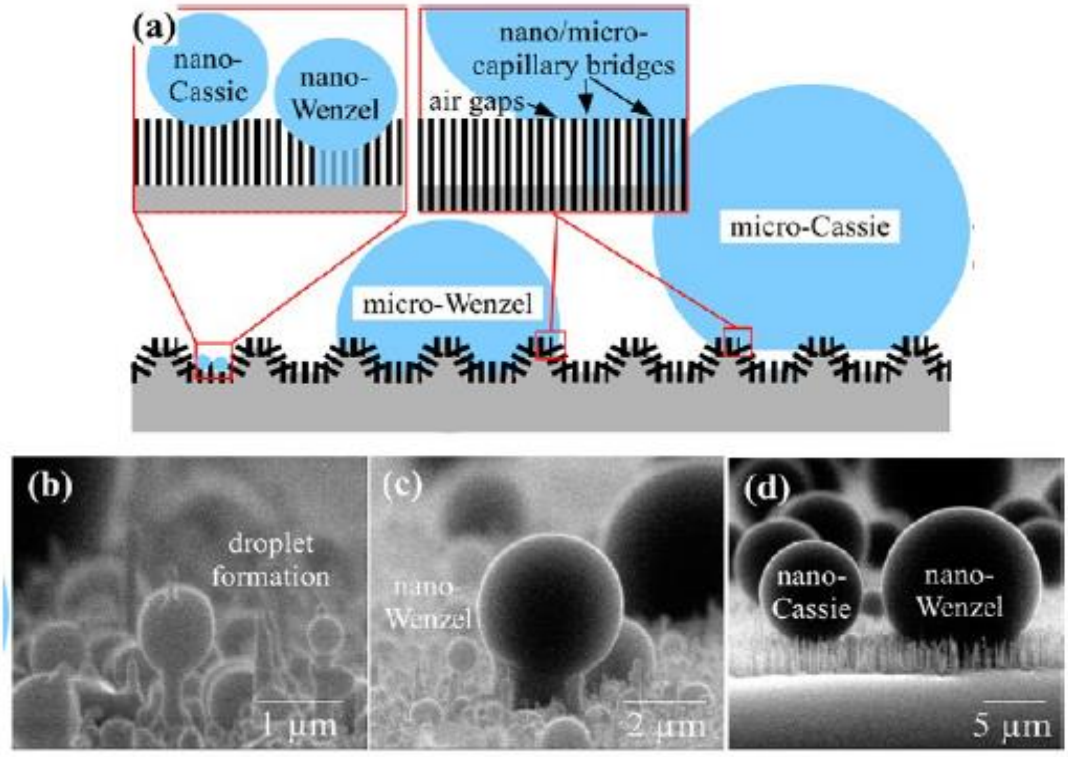

Figure 11. The two wetting states that can be present on superhydrophobic surfaces (Rykaczewski, et al., 2013).

is the dynamic contact angle. There are several methods that are applicable for measuring the dynamic contact angle. In the sessile drop method, the advancing contact angle is determined by increasing the volume of the droplet on the substrate and then the receding contact angle is found by decreasing the droplet volume. A more widely used method is determining the contact angle

hysteresis by tilting the substrate with respect to a horizontal reference and measuring the droplet hysteresis or the difference between the advancing and receding contact angles. The mobility of a droplet on a superhydrophobic surface can vary from very low adhesion, i.e. the static contact angle is greater than 150 and there is a sliding angle close to 0, to "sticky" in which a high static angle is still maintained however there is a relatively high hysteresis.

In the latter case, the droplet penetrates the surface roughness increasing the contact area and these droplets are considered being in Wenzel state. When there is no liquid-substrate contact and a boundary layer of air separates them, this is referred to as Cassie state. Many surfaces can display a transition from Cassie to Wenzel state due to surface heterogeneity in both chemical and physical texturing as well as a change in operating temperature. According to (Miljkovic, Enright, & Wang, 2012) Cassie stable surfaces has a subset of wetting morphologies which are suspended and partially wetted[2], these are observed on an array of equidistant superhydrophobic silicon nanopillars.

The most successful methods of fabrication with high droplet mobility include some form of hierarchical surfaces, which are combination of microstructures and nanostructure coated with hydrophilic groups such as Silane. Droplet repulsion is a primary characteristic, some surfaces have the capability promote coalescence-induced jumping events which were first studied by Boreyko and Chen. Coalescence on low-adhesion surfaces can result in spontaneous ejection due to the release of excess surface energy, this has been demonstrated on droplet sizes in the range of 10-100um, a behavior that is independent of gravity. The nanostructures on the surfaces allow for reduced surface adhesion by minimizing solid fraction which breaks the symmetry

[2] In this case (Miljkovic, Enright, & Wang, 2012) defines Wenzel state as those droplets that are partially wetted but are not ejected through coalescence

leading to unbalanced surface forces allowing the coalesced droplets to accelerate perpendicular to the surface. These surfaces have potential applications in self-cleaning, anti-icing, and heat transfer enhancement. Only micro-droplets on superhydrophobic surface have the capability to undergo coalescence induced jumping. Molecular dynamic simulations done by (Gao, Liao, Liu, & Liu, 2018) show that coalescence induced jumping is also possible in nanodroplets. A major drawback of these methods is the minimized sustainability. Under high stress conditions, the surface properties can diminish over time increasing maintenance cost. Typically these surfaces are relatively expensive to fabricate and are not easily implemented into arbitrarily shaped surfaces.

It appears that the vast majority of superhydrophobic surfaces that have been the subject of research are predominantly metals. In this research, polymers are preferred do to the ease of fabrication, ease of reproducibility, and the low cost. This method of fabrication is preferred for the developmental stages of the design concept of asymmetric superhydrophobic surfaces. The process of making polymers super-hydrophobic differs from that of metals. Lin & Chou (Lin & Chou, 2015) used an interesting method of pressing water-dissolvable fillers into acrylic to produce micro-scale structures achieving static angles greater than 150; however the sliding angle was greater than 10 showing low droplet mobility. Only after a supplemental coating of PDMS did they become superhydrophobic. (Chang, et al., 2015) used a PDMS mold from Xanthosoma *sagittifolium* leaf and then made patterns using a PMMA and silica composite on cold rolled steel. Although, the base substrate is not a polymer the superhydrophobic promoter is.

2.3.1. Biomimicry

Nature has always been quite the master designer; long before mankind could even fathom the wheel and the cart to go with it. In everyday life there are incredible design feats, such as insects walking on water, leaves repelling and redirecting water strategically to root systems, and even beetles harvesting droplets on their backs. Using nature for inspiration scientist in the field of biomimicry seek to replicate these surfaces for applications that require anti-fouling, anti-sticking, and anti-icing. Plant leaves have been used for inspiration for heat exchanger surfaces as well as their vascular systems and that of animals (Huang, Hwang, & Radermacher, 2017). In the case of water repelling surfaces in general, lotus leaves (Manzoor , 2013), water spiders (Wang, Yang, & Yang, 2014), cicadas (Chow, 2013), and butterfly wings (Liu, Ju, Zheng, & Jiang, 2014) have all be used as sources of inspiration. The common component present in these

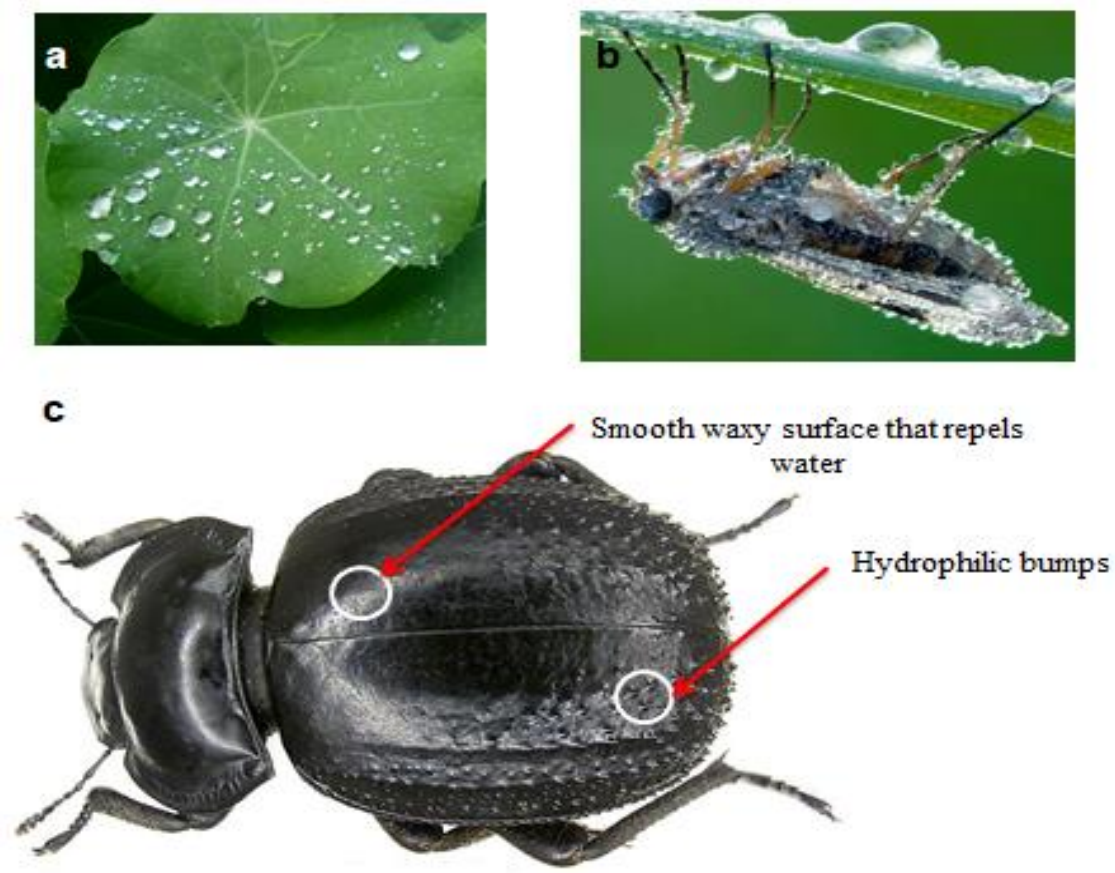

Figure 12. Example of naturally occurring hydrophobic surfaces a) lotus leaf (Why is a Lotus Rock pan so easy to clean? , 2014), b) cicada (Chow, 2013), and c) Stenocara beetle (Hiveminer).

surfaces for the specific application is their hierarchal features, that is the presence of both micro and nanoscale features. The way these surfaces have translated to everyday life includes the everyday anti-sticking household Teflon coated frying pan, anti-icing coating for aircrafts, and anti-fouling surfaces that do not allow attachment of harmful entities such as bacteria in environments that need to be sterile such as hospitals or corrosive salt in marine environments. These surfaces have characteristic wetting behavior, referred to hydrophobicity. This is also known as the strong aversion to water contact resulting in high static and low sliding angle. Droplets on these types of surfaces have relatively high mobility compared to those that are hydrophilic.

Researchers are constantly searching for long term solutions to enhance the mobility of fluids with various surface tensions on a variety of substrates with a variety of coatings and inspiration is drawn from nature. Biomimicry has served as a foundation for the fabrication of superhydrophobic surfaces which favor dropwise condensation over that of film-wise; furthermore research has shown there is an order of magnitude improvement in heat transfer if dropwise mode is prevalent on a surface (Rose, Dropwise condensation theory and experiment: a review, 2002). The surface energy of the substrate plays a crucial role in the behavior of a liquid droplet on the surface.

Minimization of surface energy through surface modification via chemical treatment and/or implementation of structures through etching or lithography, addition of nanotubes and/or nanoparticles, as well as even simple mechanical sanding (Nilsson, Daniello, & Rothstein, 2010) are some of the most common methods. More expensive and time consuming methods include CVD (Paxson, Yague, Gleason, & Varanasi, 2014) and femtosecond laser pulses (Vorobyev & Guo, 2015); nevertheless, the primary objective is to increase surface roughness are all processes

by which hydrophobic behavior can be enhanced. A combination of hierarchical structures and chemical treatment appears to be the most effective means of creating such a surface.

2.4. Asymmetric Surfaces

In order to promote coalescence, one needs to understand the transport mechanisms associated with droplets in condensation. Fluid transportation in general can occur actively or passively. Active transport includes external power sources such as mechanical vibrations, electric or magnetic field, and pressure gradient induced by a pump. Passive, also referred to as secondary active, transport utilizes gradients in the form of surface geometry, chemical treatment, or a combination of both. Surfaces with naturally anisotropic wetting behaviors include butterfly wings, pitcher plants, lizards, and water bugs. Surface features that allow these phenomena to occur include periodic but asymmetric potentials or surface ratchets that display high droplet mobility specifically in the form of hierarchical surface features consisting of both micro and nano-scale roughness. One well-known example of ratchets in application is Brownian ratchets

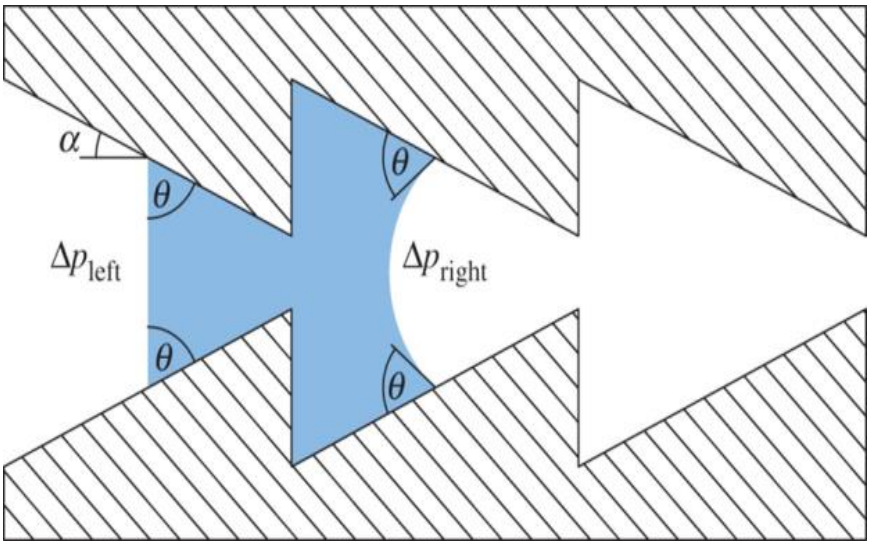

Figure 13. Microchannel with saw-tooth profile for liquid diode effect (Comanns, et al., Directional, passive liquid transport: the Texas horned lizard as a model for a biomimetic 'liquid diode', 2015)**.**

predominately used as a filtration method transporting particles of interest without transporting the bulk fluid. Other applications include lab on a chip, anti-fogging and fog harvesting, inkjet printing, cell-directing, and any application requiring liquid diodes and transportation. To supplement droplet mobility on a superhydrophobic surface, inclusion of passive mass transport via asymmetric surfaces or ratchets, has shown promise. (Brumfield, 2014) , (Chamakos, Karapetsas, & Papathanasiou, 2016), (Boreyko, Zhao, & Chen, Planar Jumping-Drop Thermal Diodes, 2011), (Comanns, et al., Direction, passive liquid transport: the Texas horned lizard as a model for a biomimetic 'liquid diode', 2015), (Daniel & Chaudhury, 2002), (Guo, Zheng, Liu, Ju, & Jiang, 2012), (Lagubeau, Le Merre, Clanet, & Quere, 2011), (Linke, et al., 2006), (Liu, Ju, Zheng, & Jiang, 2014), (Ok, May 2011), (Sheng & Jihua, 2011),and (Yu, 2014).

Past research (Ok, May 2011) on similar surfaces in the millimeter and sub micrometer scales has shown that asymmetric surfaces have the capability to induce unidirectional motion of Leidenfrost droplets shown in Figure 14 and it was concluded that the length of the moving path is strongly dependent on the droplet impact velocity. Another study (Brumfield, 2014) concluded that miniaturized ratchets rectified the convective motion of the liquid pool in subcooled nucleate bool boiling and showed promise in enhancement of heat transfer; yielding

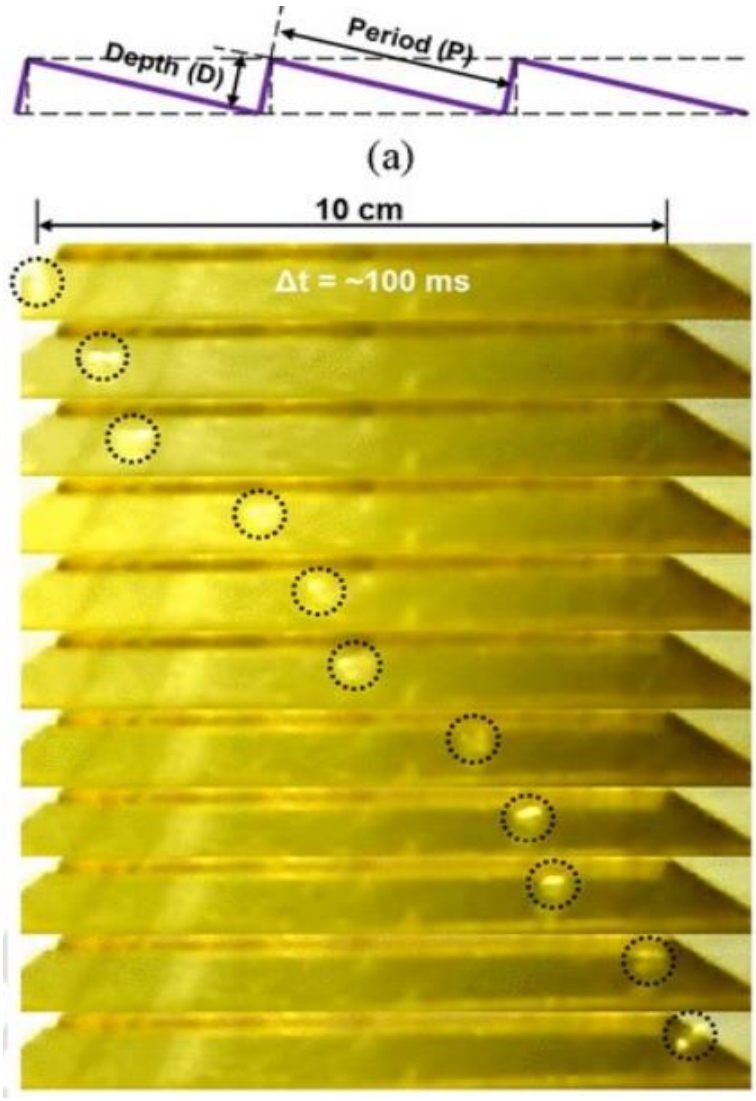

Figure 14. Leindenfrost droplets traveling on asymmetric surfaces.

heat transfer rates 30% higher than that of a polished surface. Channels fabricated with saw-tooth profiles such as illustrated Figure 13, are capable of transporting fluid from one end to another without the implementation of valves in the application of microfluidics (Yu, 2014) (Comanns, et al., Directional, passive liquid transport: the Texas horned lizard as a model for a biomimetic 'liquid diode', 2015). The key to rectifying motion lies in the unbalanced capillary force. Manipulating geometrical factors such as blaze angle and ratchet height are critical in achieving and optimizing anisotropic wetting behaviors (Sheng & Jihua, 2011). If the surface is indeed anisotropic, the droplet velocity becomes dependent on sliding direction. This unique characteristic of rectifying motion via asymmetric surface microstructures could increase the probability of events such as coalescence in condensation (Figure 15) and renewal of nucleation sites in boiling (Brumfield, 2014); two very important attributes in increasing heat transfer. The difficulty is in turning these surfaces tuning the wetting properties to be superhydrophobic. In the case of micron scale ratchets, problems can occur when the coating material is of a comparable scale to the ratchet size leading to obstructed ratchets or heterogeneous coating. Surface modification is a form of passive heat transfer techniques. Active forms include the use

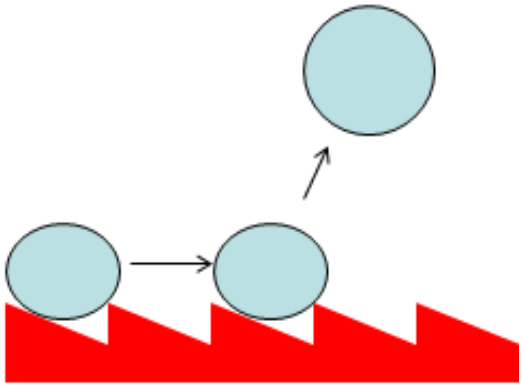

Figure 15. Cartoon displaying droplet ejection.

of a pump, acoustic vibrations, or even a magnetic field to circulate a fluid allowing cooling in systems such as CPU's in computers. Passive techniques prove to be more favorable due to the elimination of expenses associated with active techniques which can include external equipment to generate a power supply, for example.

Fins or heat sinks attached to CPUs or radiators in a vehicle, are the most common forms of extended surfaces which can also be classified as a means of passive transport, these allow for an increase in surface area; subsequently, increasing heat transfer to or from an area of interest (compared to that of a flat surface). If one considered shape of an asymmetric triangle as an extended surface, there is another contribution. For example a ball on a flat surface compared to a ball at the top most point of an inclined surface; the ball at the peak of the inclined surface has a higher potential than that of the ball on the flat surface. This potential can be used to induce unidirectional motion along the surface.

2.5. Conclusion

Many studies have primarily focused on heat transfer enhancement in condensation predominately using superhydrophobic surfaces. Very few have focused on incorporation of passive transport mechanisms to induce bulk fluid flow across a surface. Passive transport in the form of asymmetric potential, namely surface ratchets, have been studied along with the Leidenfrost effect as a promising method of rectifying otherwise arbitrary fluid flow. However, no studies were found specifically mentioning the application of superhydrophobic ratchets to rectify fluid flow primarily to induce coalescence events which could subsequently increase droplet removal rate and enhance heat transfer capabilities. Instead, a majority of the papers focus on transport mechanisms and wetting behaviors which highlights the novelty of this study.

Chapter 3. Experimental Methods

3.1. Introduction

Within this chapter, the methodology is explained in three subdivision of ratchet fabrication, manipulation of wetting properties, and methods used to characterize droplet behavior as well as heat transfer performance.

3.2. Fabrication of Microscale Ratchets

The techniques employed to produce stamps, replicate molds, and fabricate the final substrate include UV and thermal imprinting. Different sized ratchets are fabricated which are used to systematically investigate droplet and heat transfer behaviors. The general procedure uses a commercially available optical grating that is replicated using PUA in UV imprinting, this master stamp is then coated with non-sticking agent PDMS and can then be used to reproduce new PUA molds. These molds are then used in thermal imprinting of PMMA which is then coated in a superhydrophobic surface layer.

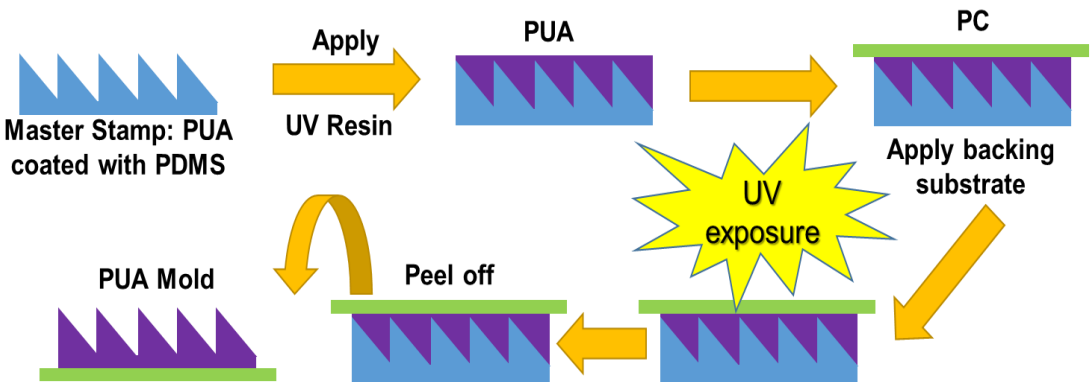

Figure 16. UV imprinting technique used to fabricate molds for PMMA ratchet substrates.

3.2.1. Replication of Optical Gratings

First, three optical gratings from Richardson Gratings™ of varying ratchet period are selected, all with the same blaze angle of 26.7° yielding a fixed aspect ratio (period: height) of 2:1. These optical gratings are reproduced using the UV resin PUA and UV imprinting (Obducat NIL) with 30 seconds exposure. Following creation of the new master stamp, a surplus of new

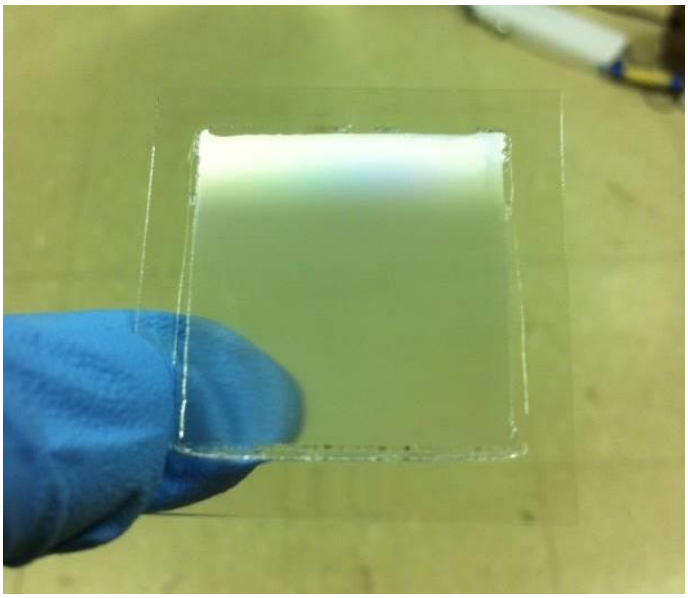

Figure 17. Optically transparent PUA master stamp of microscale ratchets.

PUA molds are made. The reason for the added process step is to preserve the integrity of the original optical gratings. In order to minimize surface adhesion forces between PUA stamp and the new PUA mold to be fabricated, an anti-sticking coating of (3-Aminopropyl)triethoxysilane (3-APTES) and poly(dimethylsiloxane) (PDMS) is applied (Lee, et al., 2006) (Lee & Kim, 2007). To apply this layer, first the samples are placed into reactive ion etching (RIE) to be subjected to O_2 plasma at 50 watts, 450mT, for 30 seconds, the samples are then soaked with 1wt% 3-APTES for 15 minutes and then rinsed with DI water, then a PDMS coating is applied and the samples are placed in an oven at 80℃ for 4 hours, finally the samples re cleaned by sonication in IPA for 5 minutes and washed with DI water.

3.2.2. Thermal Imprinting of PMMA

Following the production of PUA master stamps, PMMA sheets are cut down into approximately 2x2cm squares in preparation for thermal imprinting. Through trial and error, the side which the protective coating that was the most difficult to remove was removed first for all samples.

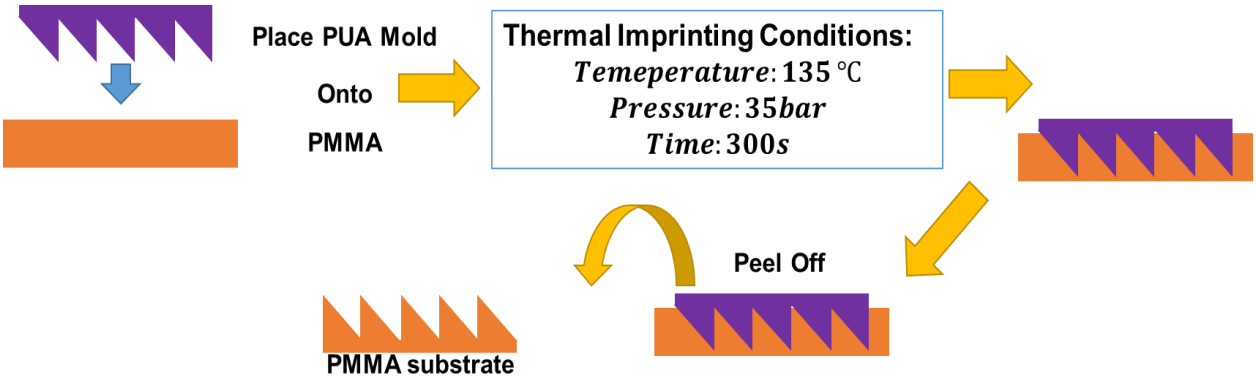

Figure 18. PMMA ratchet fabrication procedure using thermal imprinting.

The samples are placed onto the Obducat® NIL stage and the following conditions are set for thermal imprinting:135℃, 35bar, and 300 seconds. After imprinting the samples were removed from the NIL stage and blown clean with compressed air and set aside for subsequent superhydrophobic coating. The PUA stamps can be reused. Three groups of spatially periodic ratchets were manufactured, with periods of 1, 10, and 20μm all of which had the same aspect ratio 2: 1.

3.3. Polymer Superhydrophobic Surface

Thermally imprinted PMMA microscale ratchets are dip coated using a nanoparticle solution. A 1mg:100mL ethanol and hexamethyldisilazane (HMDS) coated SiO_2 (AEROSIL RX 50) mixture is sonicated for 1 minute or until the mixture is milky white in ambient conditions. Before dip coating the PMMA substrates, with and without ratchets are first blown clean using compressed air. To prevent substrate bending for the samples without ratchets through-out the dip coating process, the PMMA backing sheet is kept in place (resolved through trial and error). The

substrates with ratchets did not exhibit this bending behavior, possibly due to residual surfaces stresses left by thermal imprinting. The substrates were dip coated and left in the solution for 1 minute to allow for the HMDS coated SiO_2 particles to attract to the surface, followed by removal at a rate of approximately 1mm/second. All substrates where left to dry at ambient conditions and then coated again to achieve the desired number of coatings. The overall process is illustrated in Figure 19.

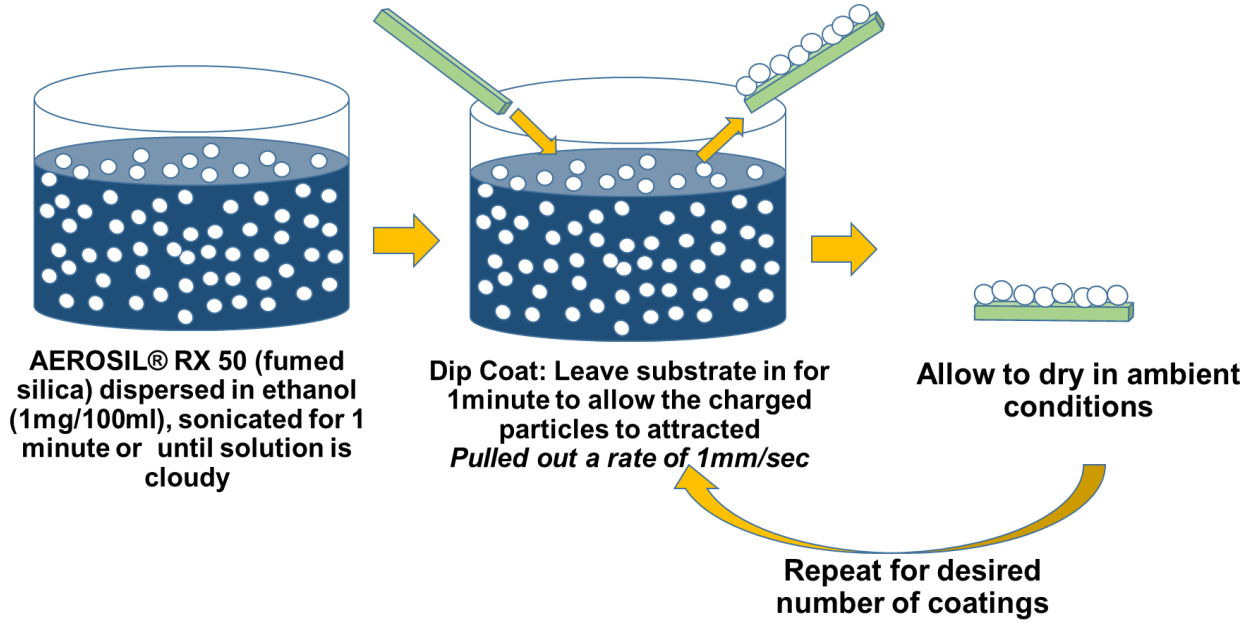

Figure 19. Illustration showing the procedure for dip coating PMMA substrates with HMDS coated SiO2.

3.4. Structural Analysis

Post fabrication, all sample groups are characterized using predominantly SEM images and quick validations of surface integrity are made using an optical light microscope. Further characterization following superhydrophobic coating is used in the form of contact angle measurements.

3.4.1. Scanning Electron Microscopy (SEM)

SEM images which capture images of sample surfaces using high energy electron beams, provide much higher resolutions compared to optical microscopy. A JEOL 6610LV SEM which is located in the Shared Instrument Facility at Louisiana State University is used for these measurements. Before any measurements can be done, a thin conductive layer of metal is coated (this layer makes imaging possible on a nonconductive polymer substrate), the coating Pt and is within the order of 10nm. The SEM settings are as follows; only secondary electrons are used and the set voltage is at 5kV, and the working distance is 10mm, with all other settings on automatic. Various magnification ranges are used to capture high resolution images. The samples which are used for surface characterization purposes are not reused in the superhydrophobic coating stage.

3.4.2. Contact Angle Measurements

Both static and dynamic contact angle test were conducted on all substrates with 3 samples per group. A VCA Optima (AST Products, Inc.) is used to conduct the static contact angle measurements; whereas a simple custom apparatus (Figure 20) is used for the sliding angle measurement. The custom sliding angle apparatus was fabricated by a former colleague (Brumfield, 2014) and is composed of a sample stage where droplets are dispersed via a syringe pump at a set droplet volume of 10μL and a leveled and mounted protractor used to determine the sliding angle to the nearest tenth of a degree. The sliding angle in the ratchet direction, the opposing ratchet direction and the perpendicular direction or measured. In both setups, 3 readings are taken per sample so that a sample average as well as standard deviation can be

extracted.

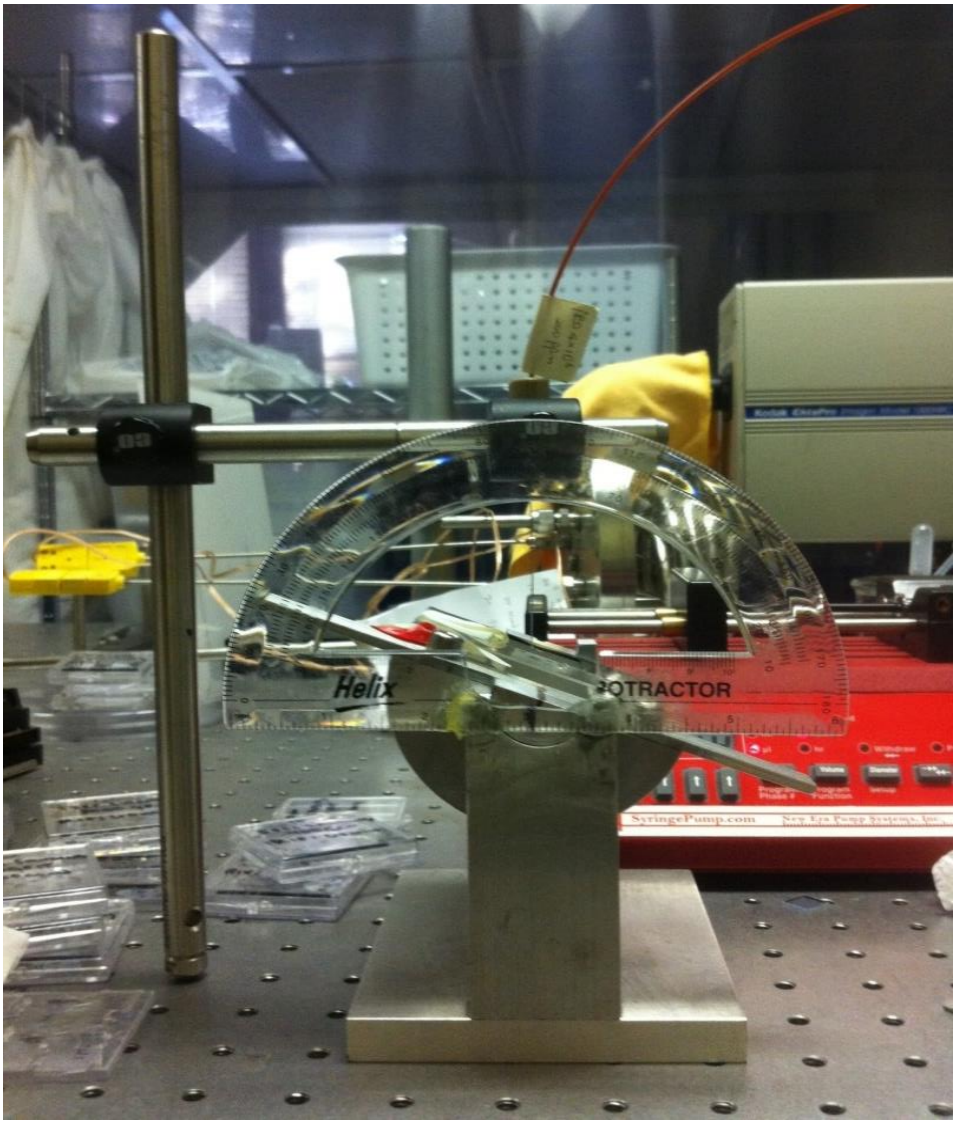

Figure 20. Custom made sliding angle apparatus.

3.5. Optical Light Microscopy of Condensation

To observe droplet behavior directly on the condensing surfaces, an experimental setup shown in Figure 21 is devised and consist of a visual light microscope equipped with a Lumenera © Infinity 1 CCD camera and the stage fashioned with an isothermal brass cooling block connected to a cooling system is used. The temperature control of the brass block is set to 2℃ and is

allowed a one hour stabilization period with the surrounding environment at ambient conditions (71°F , 35%RH) before a substrate is placed upon it. Videos in one minute intervals are taken of each test group, with and without surface coatings as well as with and without ratchets. Frames of interest are extracted from the videos in order to study average droplet size, area coverage, and coalescence behavior.

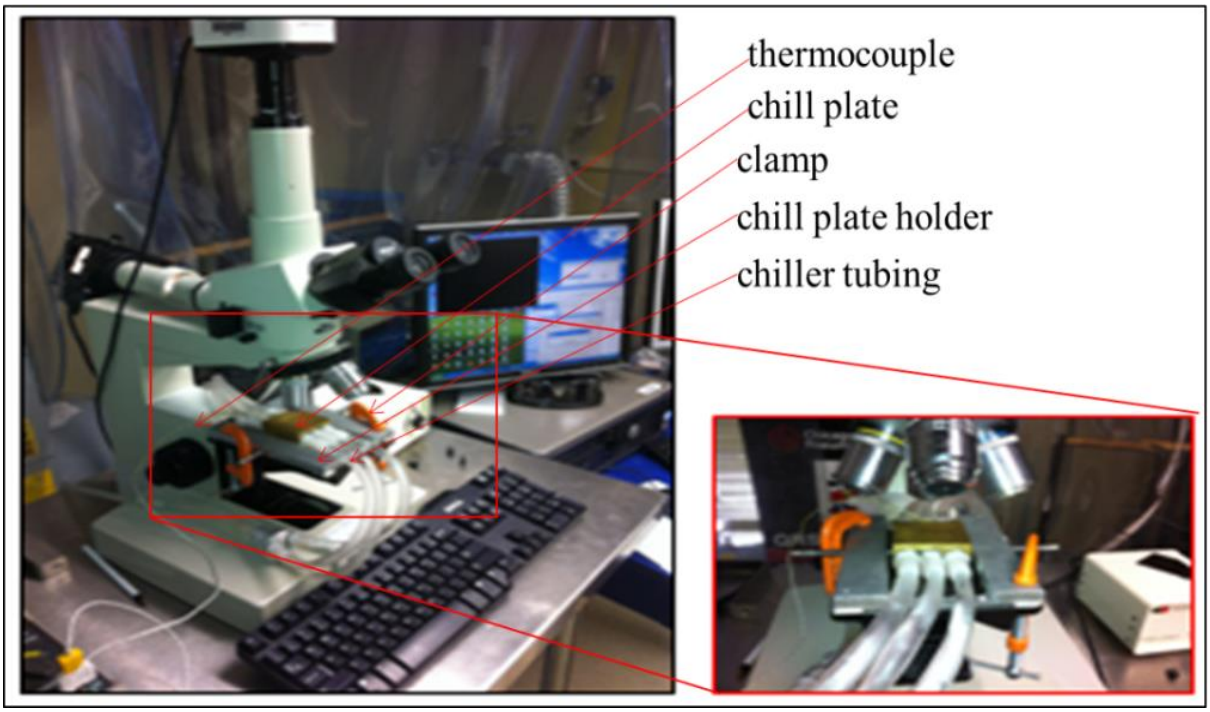

Figure 21. Experimental setup for direction observation of condensation (Brumfield, 2014)**.**

3.5.1. Image Processing

3.5.1.1. Average Droplet Size and Area coverage

The final frames of the videos are used to assess average droplet size as well as average droplet area coverage by image analysis via ImageJ. The images are extracted and saved as jpeg files then opened using paint.net software. An image layer is created over the original image in which droplets are outlined and filled using the paint function. This process is time consuming; however, far more accurate than simply using the threshold variation in ImageJ. The

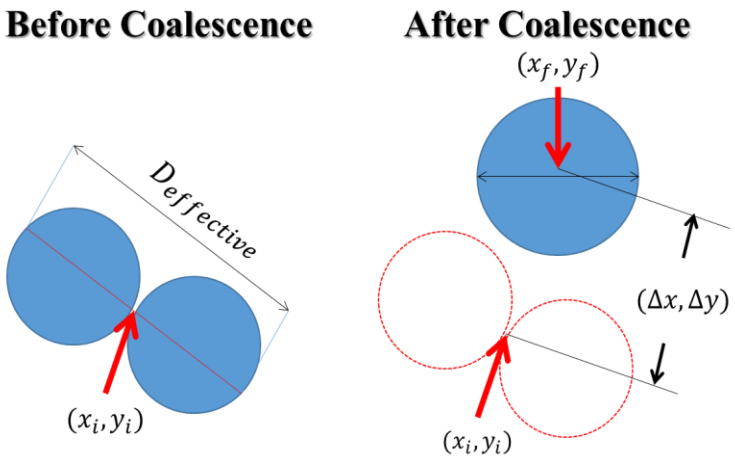

Figure 22. Measuring displacement of coalesced droplets.

thresholding is still adjusted in ImageJ to convert the image to an 8-bit black and white image. The Analyze Particle command is used to quantify area and area coverage. The reason for this time consuming process is due to the presence of ratchets. Without creating an image mask in paint.net program, the adjusted image (post-thresholding) leaves vertical lines which outline the ratchet peaks. The initial remedy of Fourier transforms and then inverse Fourier transforms to remove the periodic features, removed a majority of these vertical surface features but not enough to adequately count droplets.

3.5.1.2. Coalescence events

Also, extracted from the videos are the counts of coalescence induced ejection events that occur. Finally, coalescence events from the first ten seconds are counted and droplet configuration as well as coalescence displacement are recorded. For coalescence displacement, all events within the first 10 seconds are noted and then droplet sizes are measured. Just before the coalescence event an effective diameter of the two droplets, i.e. the combined diameter along with any gap distance between the two droplets, is identified to locate the effective center (pixel location). This center location is used as the point of origin. Post coalescence, the new droplet that has

formed as a result of the merged droplets is measured for its area and then its center location. The vector difference between the point of origin and the displacement point determines the displacement vectors in x and y components. The y displacement corresponds to either the ratchet direction of the opposite whereas x is the vertical component. Figure 22 demonstrates how these values are denoted. These values are measured manually using the commercially available MB Ruler 5.3. In order to further investigate any potential changes to surface wetting behavior, a video is recorded of a superhydrophobic substrate subjected to the aforementioned conditions over the period of one hour.

3.6. Conclusions

Both UV and thermal imprinting techniques were used to fabricate cm scale substrates consisting of micro ratchets with various periods of 1, 10, and 20μm. These ratchets were dip coated with HMDS coated SiO_2 nanoparticles to create a superhydrophobic surface. Surfaces were inspected before and after coating using SEM and visual light microscope. The characterization methods post coating involve observation using a CCD microscope camera to quantify droplet area and coalescence behaviors.

Chapter 4. Surface Characterization

4.1. Introduction

Samples are observed in after ratchet fabrication to determine if ratchet integrity is retained and how the period affects the sharpness of the peaks, after dip coating with HMDS coated SiO_2 to discern whether coating thickness obscures the ratchets, and following condensation experiments to see if there is any variation in the coating. The wetting behaviors are quantified after coating and after all condensation experiments to determine if there is coating degradation.

4.2. Structural Analysis

Following thermal imprinting, samples are observed using SEM (Figure 23). Before observation

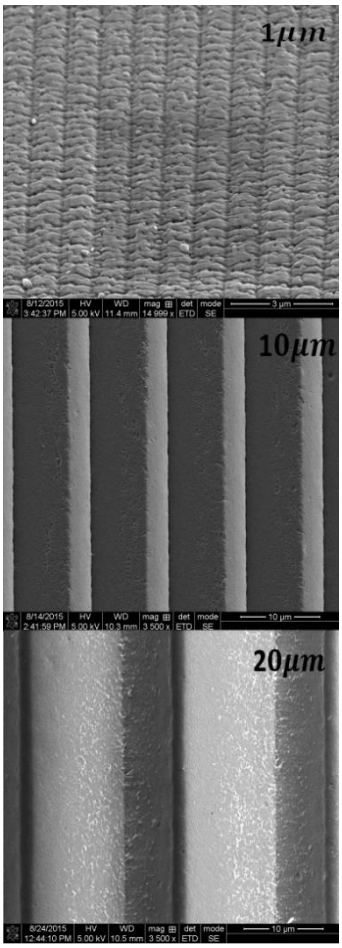

Figure 23. SEM images of ratchet produced via thermal imprinting.

a thin layer of Pt, less than 10nm is deposited on the PMMA substrates, this layer is quite visible on the 1um period ratchets. The 10 and 20 um periods should higher ratchet integrity, specifically a more homogenous surface compared to that of the 1um period which did not display nearly as sharp peaks.

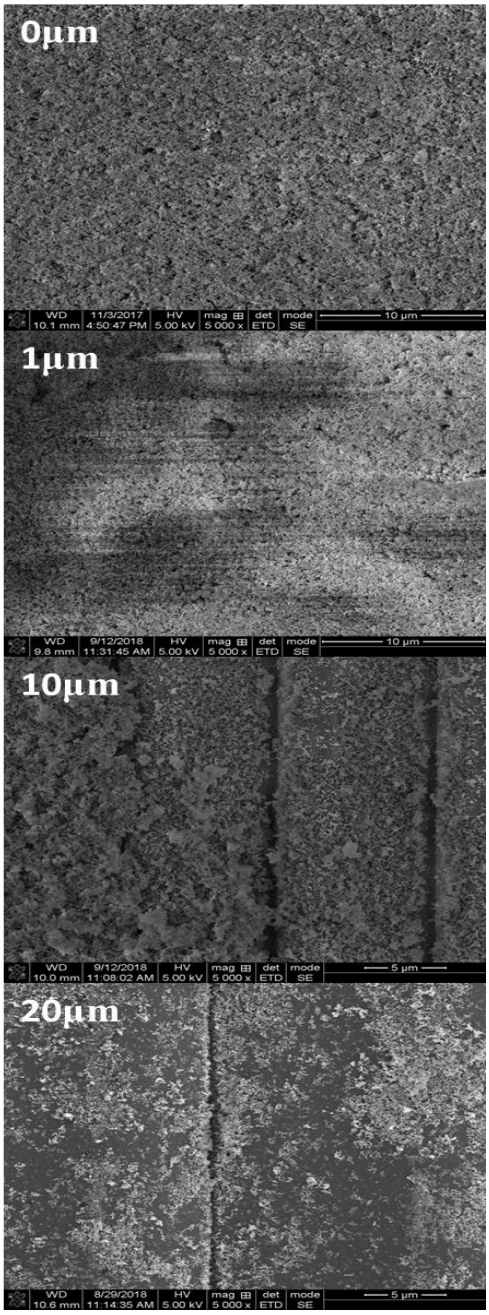

Figure 24. SEM images of HMDS coated SiO_2 nanoparticles dip coated onto PMMA substrates. For 0um, the number of coatings is 4 whereas the ratchets each of 6 coats.

These substrates are easily reproduced using successive thermal imprinting from a PUA mold. Following the fabrication of PMMA substrates, a superhydrophobic coating of HDMS coated SiO_2 nanoparticles is applied and the surfaces are observed near the center of each substrate and are shown in Figure 24. It is difficult to directly measure the coating thickness but one can see that it thick enough to render this sample of the 1µm period ratchets unusable for condensation experiments. The 10µm period structures show that the coating can be inhomogeneous due to large agglomerates that may form on the surface as seen on the left side of the image. The 20µm period shows that the surface coating is not quite as thick in this area. To classify whether this coating method is useful for the larger sized ratchet periods, wetting behavior is observed in the proceeding section.

4.3. Wetting Behavior

4.3.1. Influence of the Number of Coatings

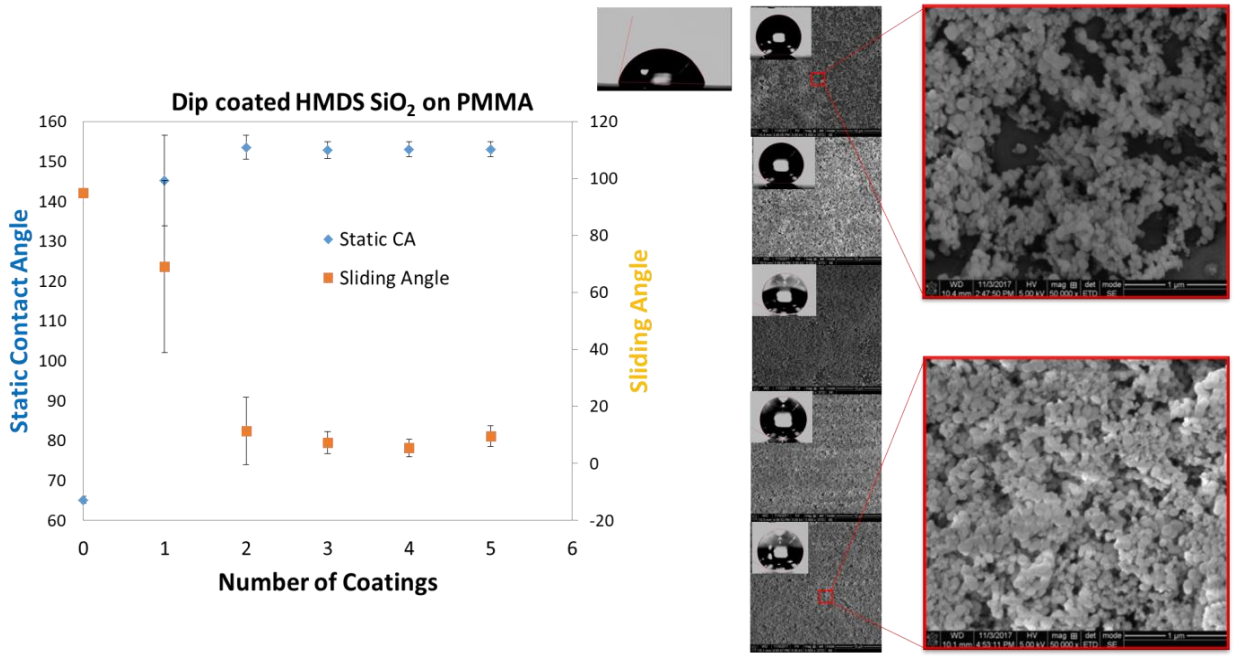

Figure 25. Wettability and coating measurement and observation using contact angle analysis and SEM.

Conduction of contact angle analysis after successive coating revealed the strong dependence on

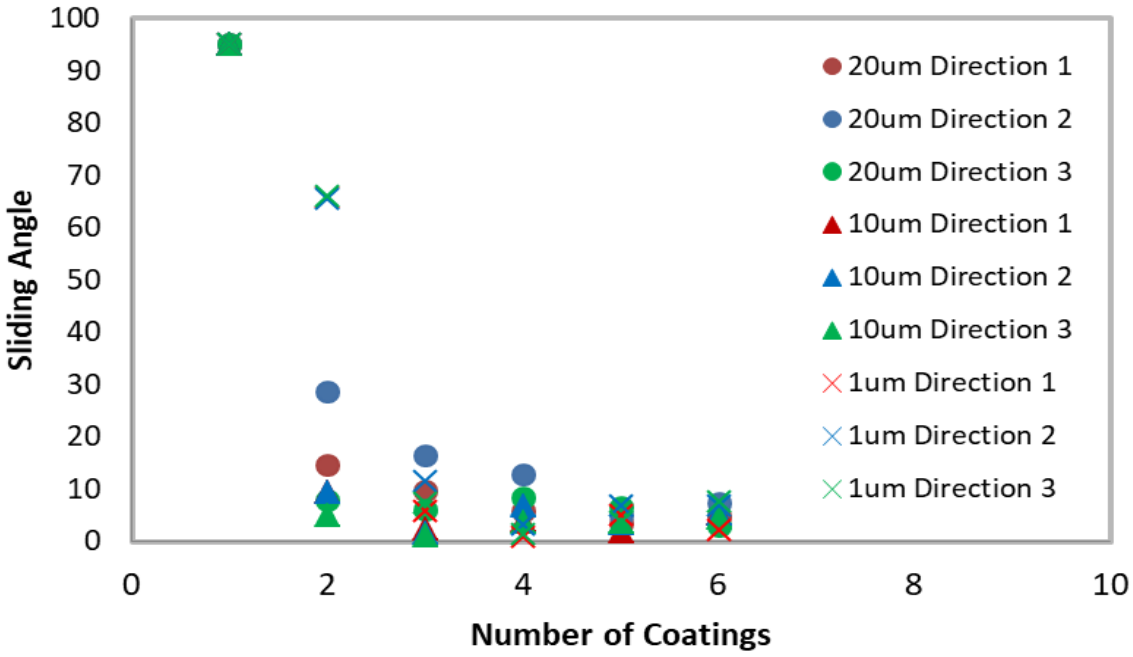

Figure 26. Coating analysis for optimal sliding angle at various ratchet periods.

the number of coatings. For a unpatterened PMMA substrates (those without ratchets), an increase in the number of coatings from 0 to 2 there is a significant increase in static contact angle (about 137% increase) after which, a plateau is reached and further coating does not produce any change in contact angle; however, a minima for sliding angle is not reached until about 4 coatings. One can see the structural variation between a single coating and 6 coatings, as the number of coatings increases the packing of the coating increase as well, as expected.

4.3.2. Preferred Sliding Direction

For PMMA ratchets, only sliding angle is measured considering the primary means of transport depends on the droplet mobility. Since the ratchets has essentially three directional variations due to the asymmetry of the surface, the sliding angle is measured in each direction to determine which provides the minimum resistance to droplet motion; this in turn will determine the most

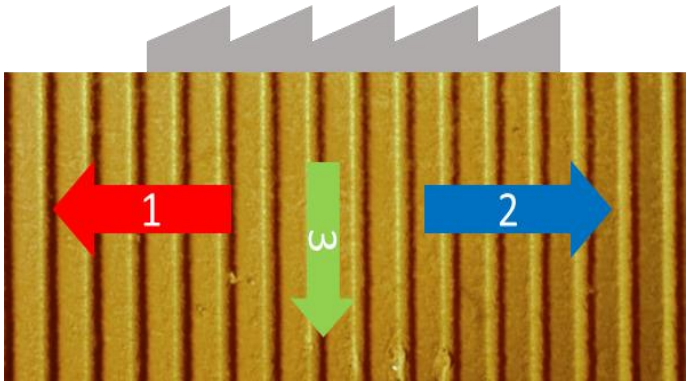

Figure 27. Illustration of the various sliding directions on a substrate with ratchets.

favorable direction of transports. Just as with, substrates without ratchets, first the optimal coating number needs to be determined. One can see a similar trend for the ratchets as was present in the unpatterened PMMA, however, it takes a larger number of coatings to achieve a

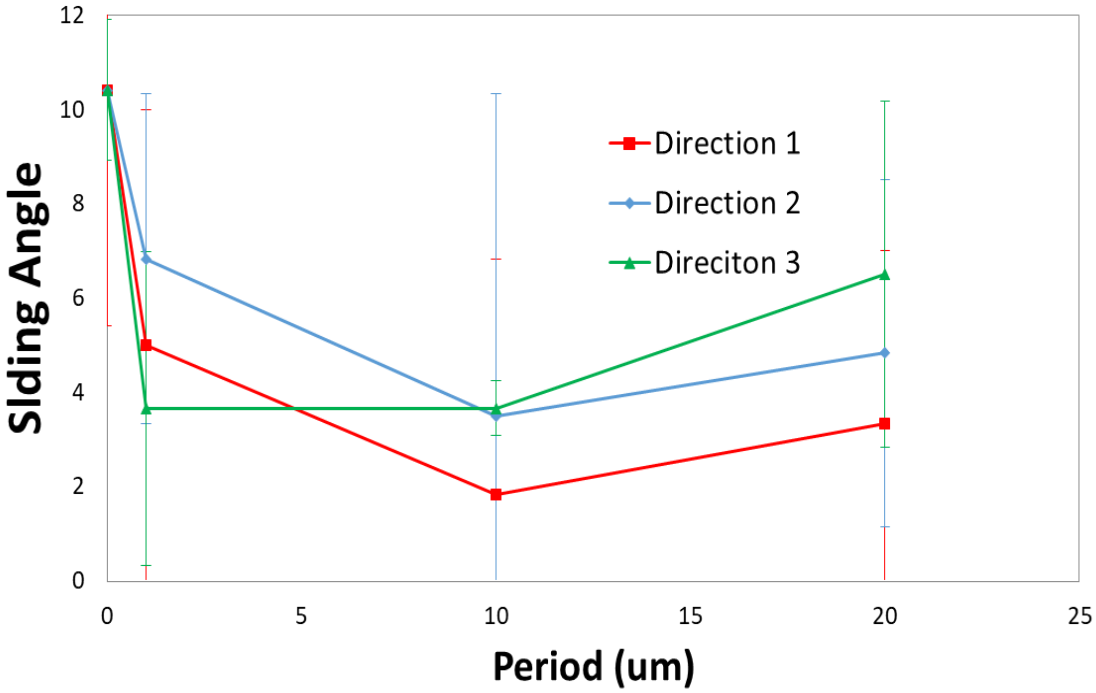

Figure 28. Sliding angle variation dependent on ratchet period.

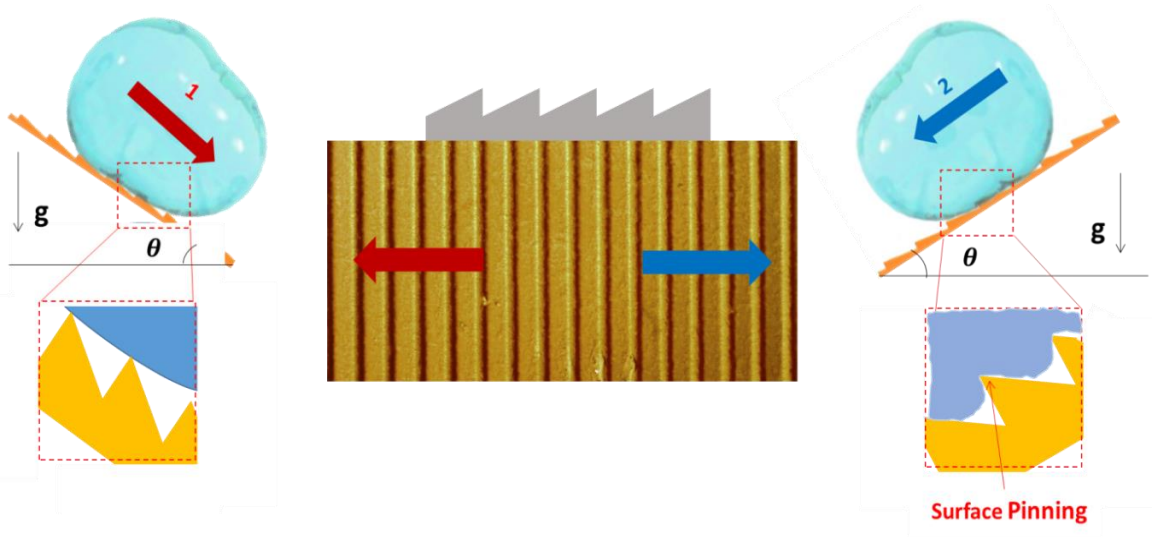

Figure 29. Illustration demonstrating variation in sliding direction on a ratchet surface.

favorable sliding angle condition. Considering there is not a large degree of variation between the 5th and 6th coating and that the 6th coating displays values that are slightly closer together in terms of sliding direction, this coating number is chosen.

These variations are further investigated as a function of ratchet period. As expected, the substrates patterned with ratchets out-perform the blank substrates and show a preferred sliding direction. All ratchets periods, with the exception of 1um, show a preferred direction in the 1 direction, in good agreement with literature. A minima for sliding angle ($2° \pm 0.5°$) occurred for 10um period. The behavior of the 1um ratchet period diverges from the behavior of the larger periods due to the ratchet size being an order of magnitude lower than the droplet size as well as the mean particle size of the coating being larger than the ratchet period which is evident in Figure 24.

The results produced by the sliding angle test are in good agreement with literature (Chamakos, Karapetsas, & Papathanasiou, 2016), (Ok, May 2011), (Sheng & Jihua, 2011), (Linke, et al., 2006). Figure 29 shows an illustration of the mechanisms associated with the sliding in the

ratchet direction as well as in the opposite direction. There is an added barrier associated with the sliding direction 2 which is pinning to the ratchet peaks; this adds a resistance to the mobility.

4.3.3. Effect of time on coating

The coating stability is test over a period of 4 months, showing that the static contact angle

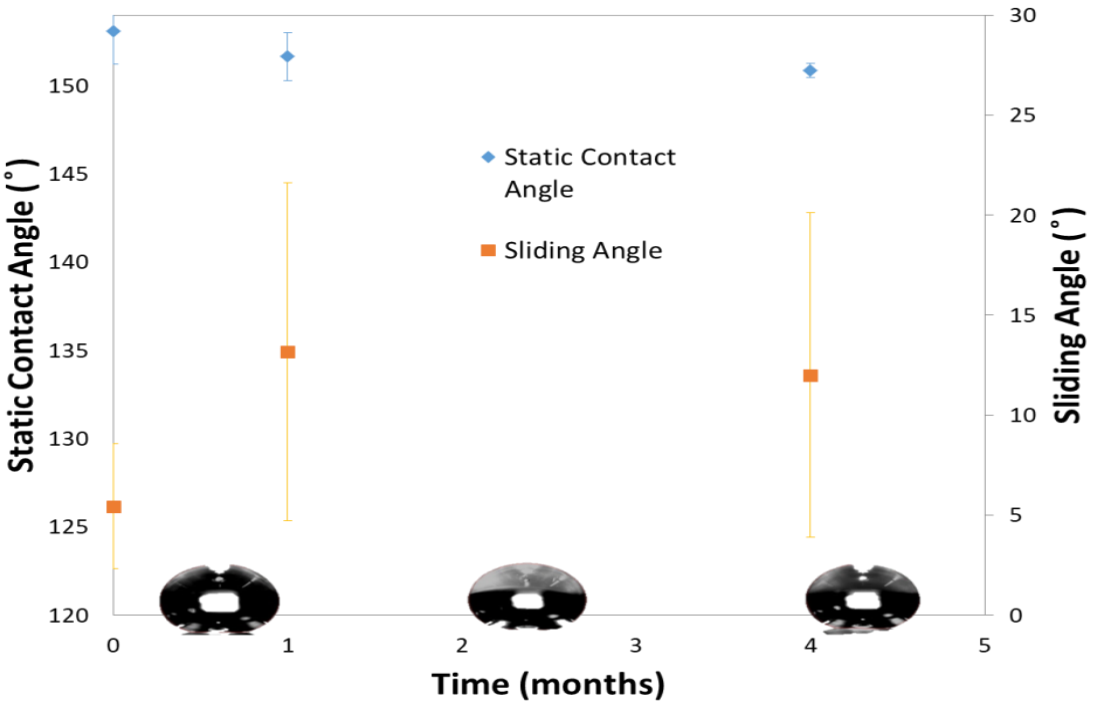

Figure 30. Stability analysis of dip coated substrates over a period of 4 months.

remains relatively the same where there is a slight increase in the sliding angle. The largest variation occurs from the initial coating to 1 month. It should be noted that this stability analysis is performed before condensation experiments.

4.4. Conclusion

Contact angle analysis revealed that the optimal coating number for unpatterened PMMA substrates is around 4 which is slightly different compared to the required coating number for substrates with ratchets, this is due to the larger surface area. Low sliding angles qualify the

surfaces to be superhydrophobic. For ratchets, the sliding direction agrees with literature in that the ratchet direction provides the least amount of resistance for droplet motion. In conducting a stability analysis, it is found that the surface does appear to degrade slightly over time before even being subjected to any condensation; therefor it is beneficial to use the surfaces for experimental purposes within the first month of dip coating.

Chapter 5. Optical Microscopy of Condensation

5.1. Effect of coating and ratchet period on droplet density

The average droplet area is dramatically dependent on the presence of coating. Without coating blank substrates yielded droplet areas nearly doubled that of the coated samples; 1 and 10um period ratchets had the same behavior. The most dramatic increase occurred for the 20um periods ratchets this appears to be due to the mode of droplet growth on the uncoated substrates.

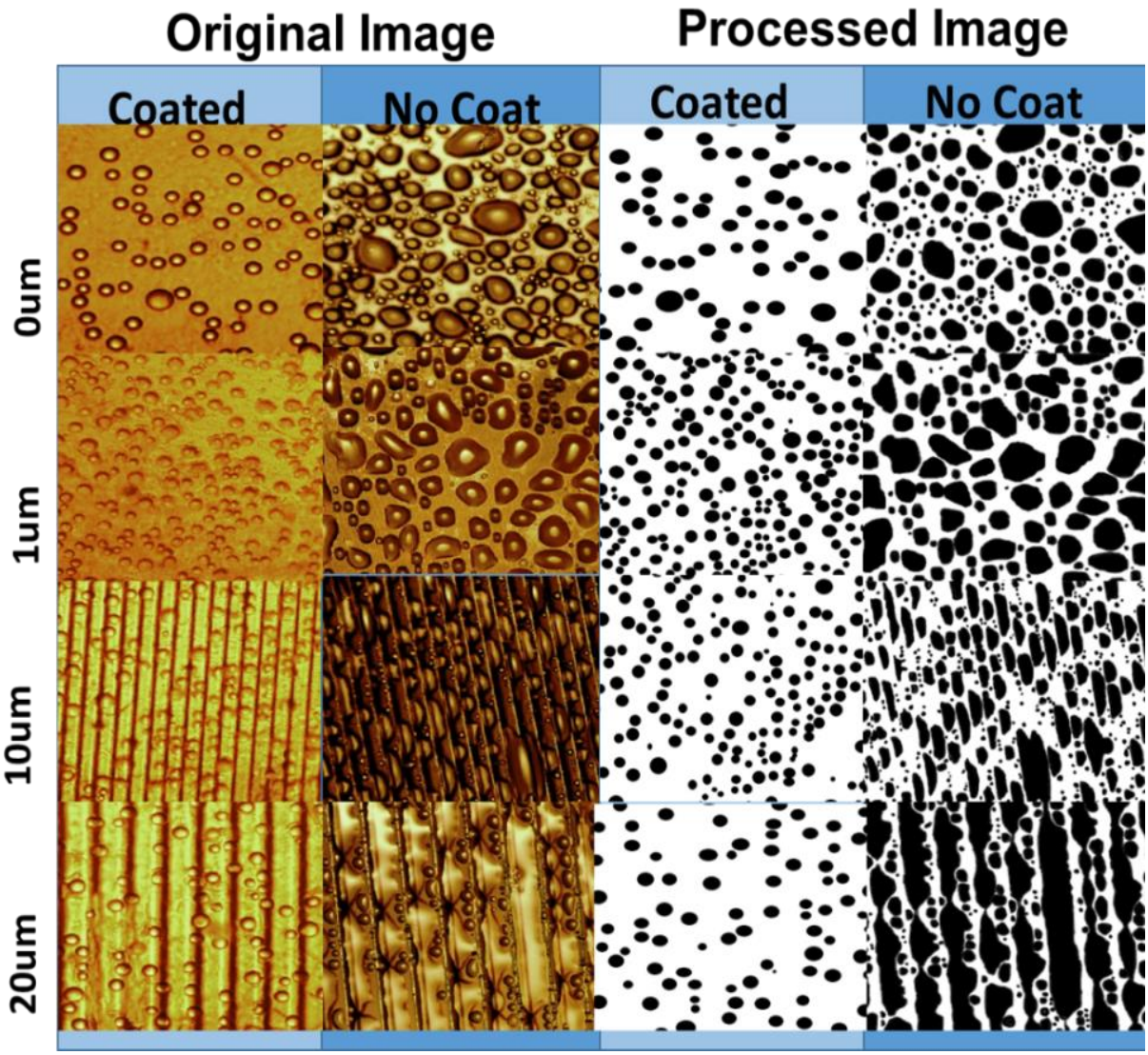

Figure 31. Visual light microscope images from pre and post processing.

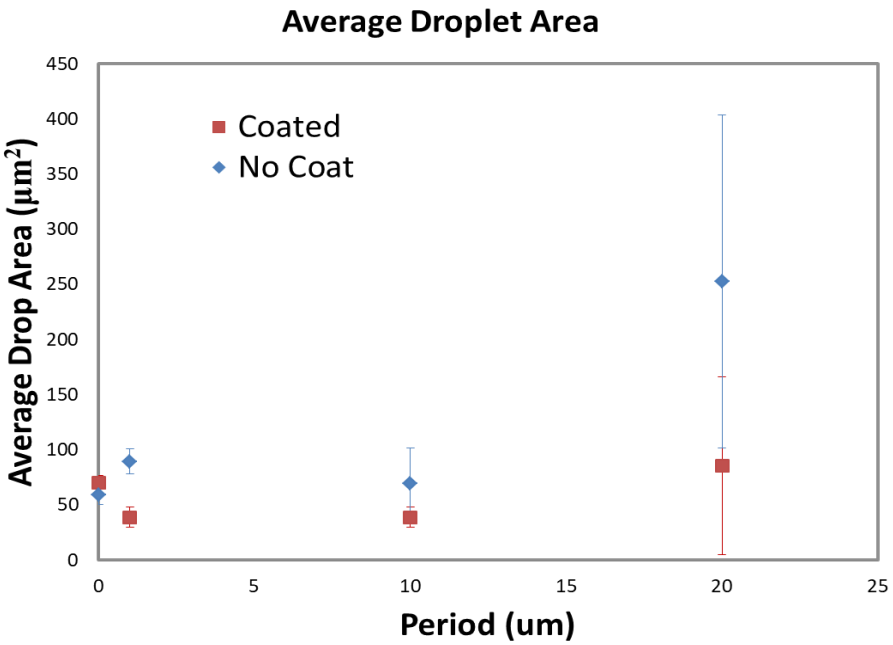

Figure 32. Average droplet area with and without HMDS coated SiO2 particle coating as a function of ratchet period.

The droplets grew within the ratchet valleys, forming an elongated shape and easily merging with other droplets eventually leading to nearly fully wetted ratchet valleys. In smaller ratchet periods, the droplets grow predominately in ratchet valleys rather than at the ratchet peaks due to the fact that there are a larger number of potential nucleation sites in non-peak areas and the droplets that do nucleate at ratchets peaks are swept downward into the valleys. One can observe in Figure 32 he larger the period, the larger the average droplet area ; however, for 1um droplets very quickly grow to sizes much larger than the ratchet period and can easily wet the surface yielding areas only slightly less than that of a blank untreated substrate. Although there was a clear trend in the average droplet area, there appears to be no such trend for % area coverage (shown in Figure 33) for the uncoated substrates. The addition of HMDS SiO_2 coating reduces

the average droplet area, most dramatically for the 20μm period. Even though there is a decrease

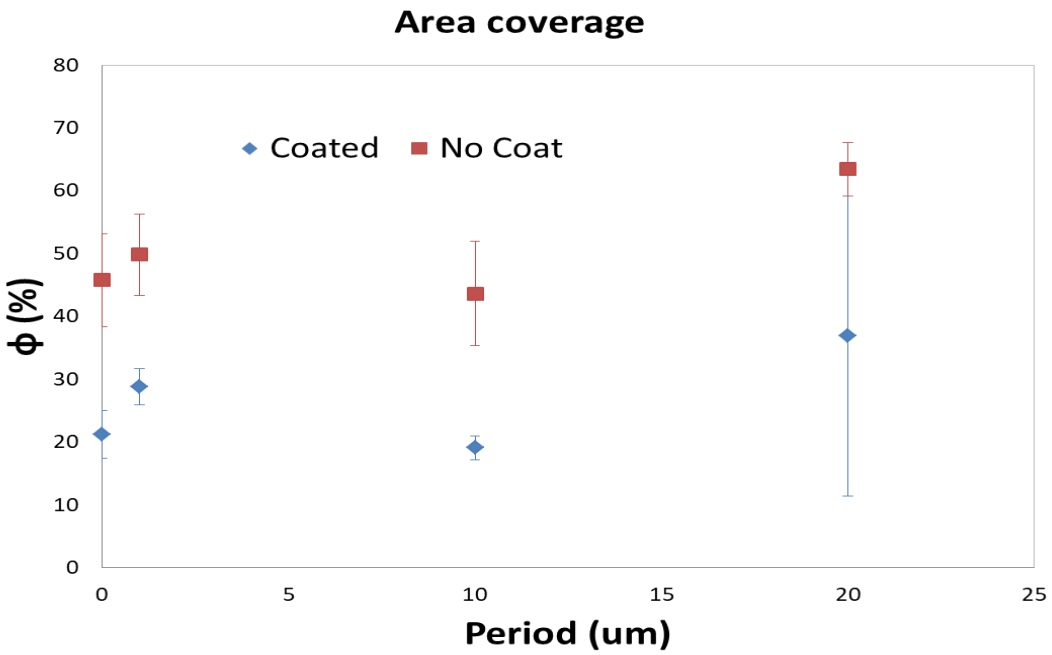

Figure 33. The area coverage of substrates with and without coating as a function of ratchet period.

in the average area from a blank substrate to a substrate with ratchets, there is little to no change when ratchet size increases. The area coverage shows a slightly parabolic behavior with minimum area coverage at 10μm period.

5.2. Coalescence events

5.2.1. Ejection Events

Spontaneous droplet removal shows a favored droplet diameter which remains relatively constant (approximately 10μm) regardless of ratchet period (shown in Figure 34). This value is consistent with literature, which found critical diameters of departure to be around 10μm (or in the same order of magnitude). What is interesting is the period influence on the number of ejection events. The average number of events doubles from 10μm to 20μm. This could be due

to ratchet actively playing a role in the coalescent event. For the 10μm period, the critical drop diameter is equal to the period leaving little to no room for the surface asymmetry to influence the motion; however, for the 20μm period there are more potential configurations for the onset of ejection events.

Figure 35 shows that before and after ejection events. The nucleation locations are statistically random; however it upon investigation of ejection events, several coalescence configurations are

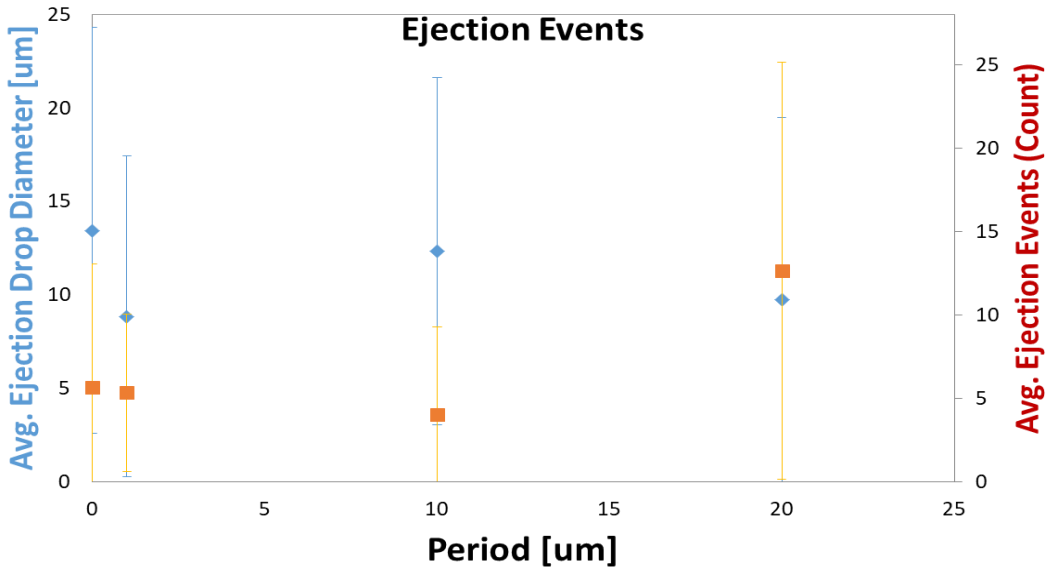

Figure 34. Average droplet diameters that coalesce then eject and average number of ejection events as a function of ratchet period.

observed. To investigate this further the configurations for 10 and 20 um periods are compared to discern if there is a preferred configuration that may have induced the variations in the count of ejection events shown in Figure 34.

The schematic in Figure 36 shows the potential configurations for coalescence induced ejection.

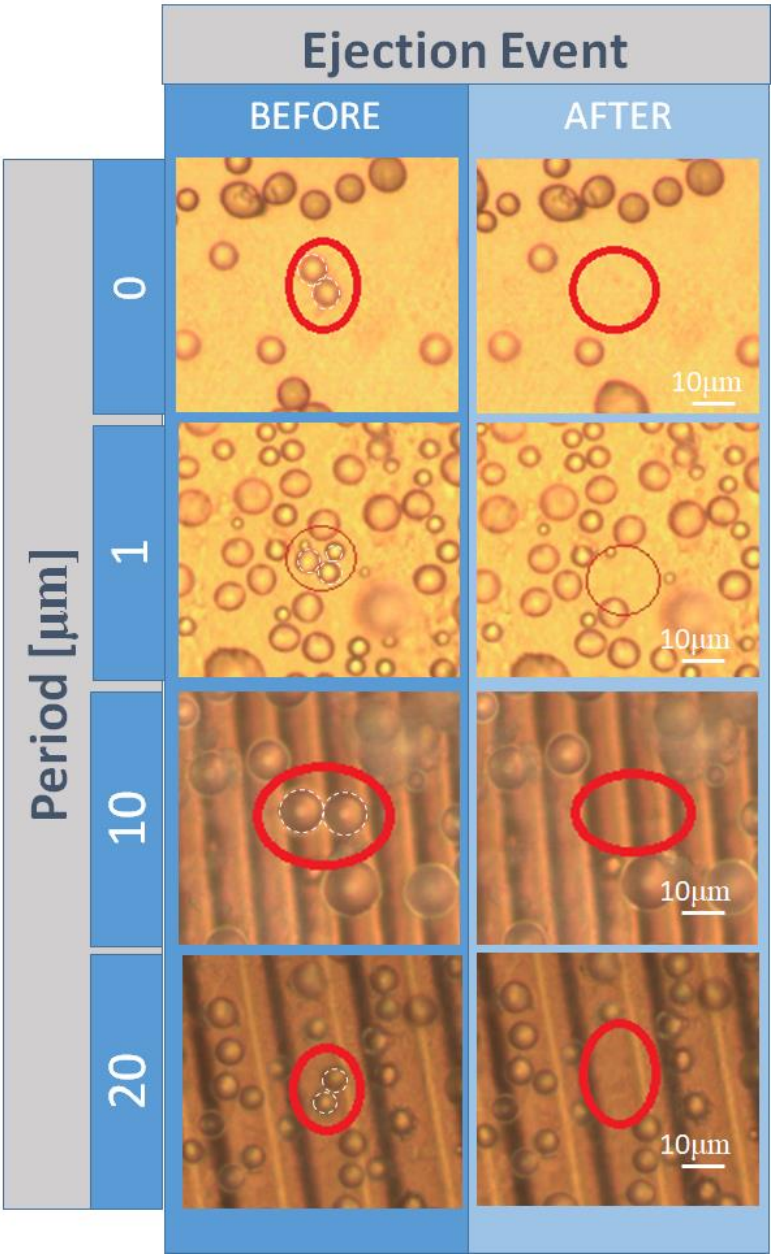

Figure 35. Before and after ejection events for substrates with coating.

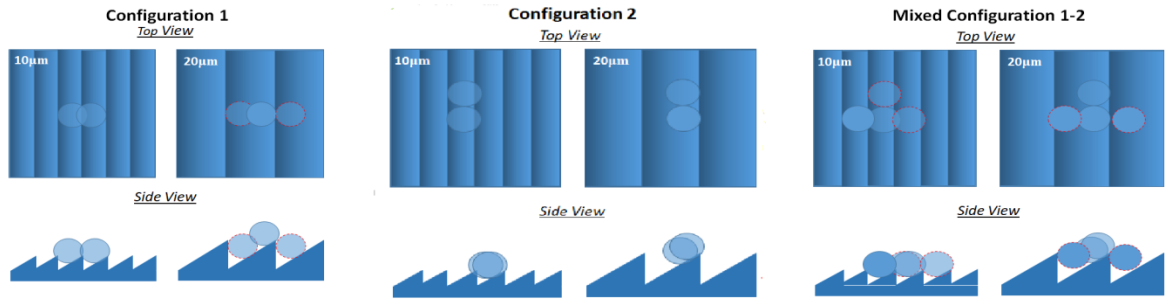

Figure 36. Potential configuration for ejection events for 10 and 20um period ratchets.

The angle of the droplets relative to one another can vary slightly from what is represented. Essentially there are two separate configuration types, those aligned horizontally (in reference to the schematic) and those aligned vertically. In the case of configuration 1, notice that for 20um period there are two droplets outlined in red. These events in configuration 1 occurred with only two droplets, only one droplet outlined in red only with the one not outlined in red was present for each event in this configuration. These events can also occur in mixed configurations, 3 droplets or more are `characteristic to these types of configurations. After counting the number of events in a specific configurations, it becomes evident that 20um period ratchets dominate. At an average droplet diameter of 10um, 20um period out-performed the 10um period ratchets in

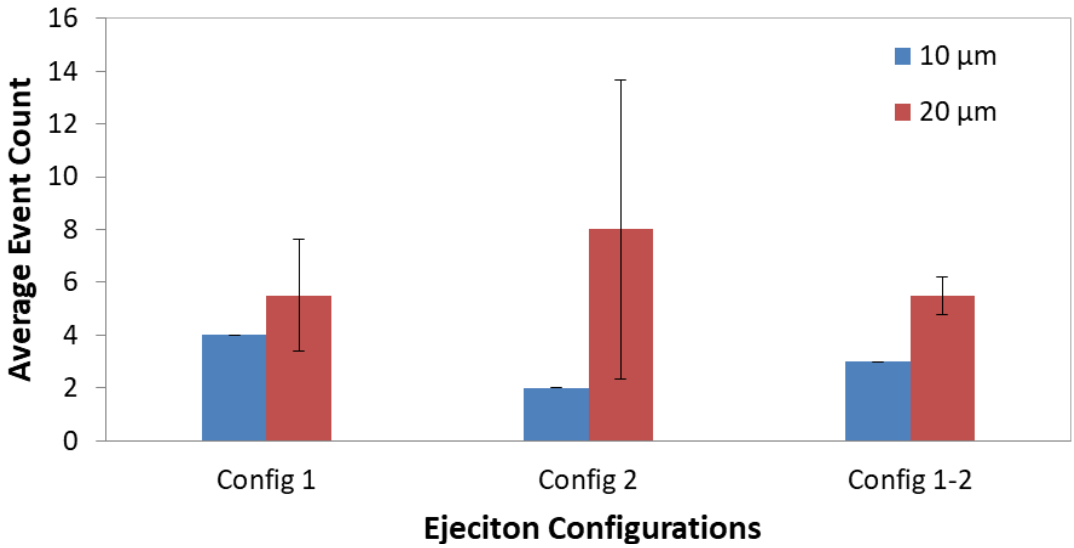

Figure 37. Average event count for various ejection configurations of 10 and 20um periods.

all configuration types. The zero standard deviation present for 10um period is due to the face that there was only one sample for which coalescence induced ejection occurred.

5 2.2. Coalescence Displacement

To further investigate the effects of ratchet period on droplet interaction, specifically during coalescence, behaviors within the first and last 5 seconds of the direct observation videos are analyzed. Droplet sizes before coalescence are measured along with an effective center, which is determined by an effective radius that encases both droplets. The center location of the new droplet formed post-coalescence is measured and subtracted from the effective center pre-coalescence and a displacement vector is established. There appears to be a trend of increasing

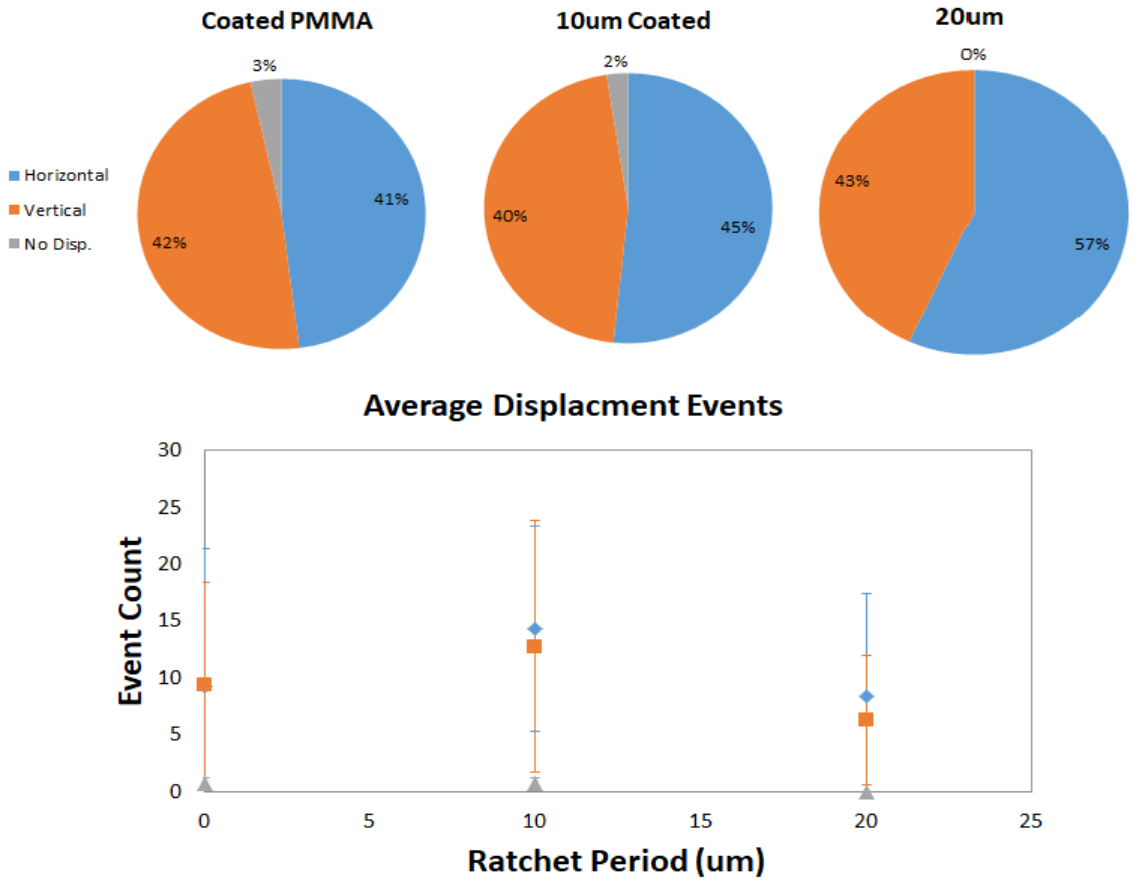

Figure 38. a) Maximum average displacement per event. b) average displacement event count as a function of ratchet period.

displacement in the horizontal direction, either in the ratchet direction or in the opposite. The larger the period, the greater the larger the displacement vector in the horizontal direction, this is in agreement with the previous results which showed that the larger periods have more configurations for coalescence events on a single ratchet simply due to a larger surface area. Further quantification of the events shows that the average displacement has a maximum at the 10um period ratchets.

5.3. Conclusion

SiO_2 nanoparticles reduced the % area coverage and overall average droplet size on substrates. Coalescence induced ejection events were observed for coated substrates, in which the droplet ejection diameter remained constant at about 10um. Ratchet period played a role in the number of ejection events for the one minute test intervals, the larger the period the greater the number of ejection events. The larger number of coalescence configurations for the 20um period (due to larger surface area), allowed for a greater probability of ejection. Further investigation into on the influence of ratchets on coalescence behavior showed a small percentage increase in the horizontal coalescence events (either along ratchets or opposite ratchets) compared to vertical or no displacement events.

Chapter 6. Design and Fabrication of Liquid Crystal Thermography

6.1. Introduction

Following the fabrication and characterization of ratchets, the heat transfer behavior is systematically investigated. An experimental setup from literature provides a base model for the experimental setup within this study.

6.2. Design

A custom condensation chamber nearly mimicking that of Bansal et al (Bansal, Khandekar, & Muralidhar, 2009) is fabricated. The image depicts the experimental setup next to a schematic to show the internal layout. The general design concept consists of an enclosed environment with a metal base in which heat flux is controlled, an internal water/fluid reservoir, a sample stage, and a top cooling plate. The top cooling plate consists of an observation glass and a transparent polymer flange that is also a cooling channel. The variations between the fabricated chamber and Bansal et all chamber, is the lack of a cooling channel on the top flange and here, temperature of the bottom brass flange is controlled instead of directly controlling the heat flux.

6.3. Fabrication

The completed design is shown in Figure 41. The system is built using bulk parts which are cut using custom designs. A $\frac{1}{2}$" brass plate (McMaster-Carr) is cut into a 4x4" block and a ¼ " circular ring is drilled with an inner diameter of 2 ¾ " and an outer diameter of 3", this will fit the O-ring and the polycarbonate tube that serves as chamber housing. Near the corners, the ¼"-20 for 18-8 stainless steel bolts (McMaster-Carr) holes. On the back side of the brass flange, a 3/8" recession with a 2 1/8" diameter is made to accommodate a steel disc 100W ring heater . The polycarbonate tubing that houses the working fluid is 3" in OD and 2 3/4 "ID. The top flange is also polycarbonate, the bulk material is of ½"thickness and is cut into the same 4x4"

size as the bottom brass flange with the same bolt hole array as well as the circular recess for the O-ring and the PC tubing. The center of the PC flange contains a circular through-hole for a sight glass and a slight recession to place the sample in and affix with PC retainer. The AutoCAD drawing can be found in Appendix A. Additionally two through holes are made through the top of the chamber, in the PC flange and the other is through the side of the PC tubing. The first through hole is to place instrument probes, specifically thermal couples and the second is for the air valve to pump the chamber to a desired pressure. The air valve is affixed with a through the wall fixture then connected to bleed valve, a T-joint which connects to a

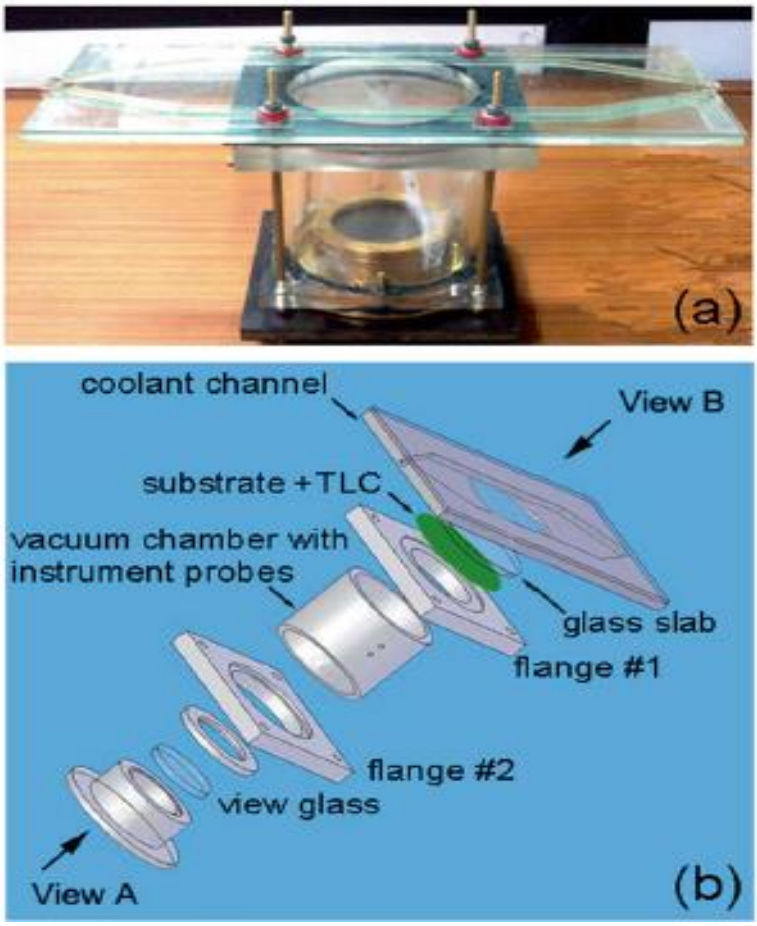

Figure 39. Experimental setup of Bansal et. all a) overall layout b) illustration depicted the exploded view of the chamber (Bansal, Khandekar, & Muralidhar, 2009).

vacuum pressure gauge, and then another valve which opens and closes the line to the pump. Due to certain circumstances, the power supply for the disc heater could no longer be used; therefor the brass flange is heated using a hotplate (Fischer Scientific). An hour stabilization period is allowed from when the hot plate is turned on to the initial temperature setting (2.2 on the hot plate dial and vapor temperature≈ 30℃). Stabilization periods between temperature intervals are approximately an hour as well and relative humidity remains at approximately 100%.

6.4. Calibration

A calibration setup is devised based on setups in literature. An outline of the setup is shown in Figure 42. The setup is comprised of a hot plate, isothermal brass block, cover plate with optical

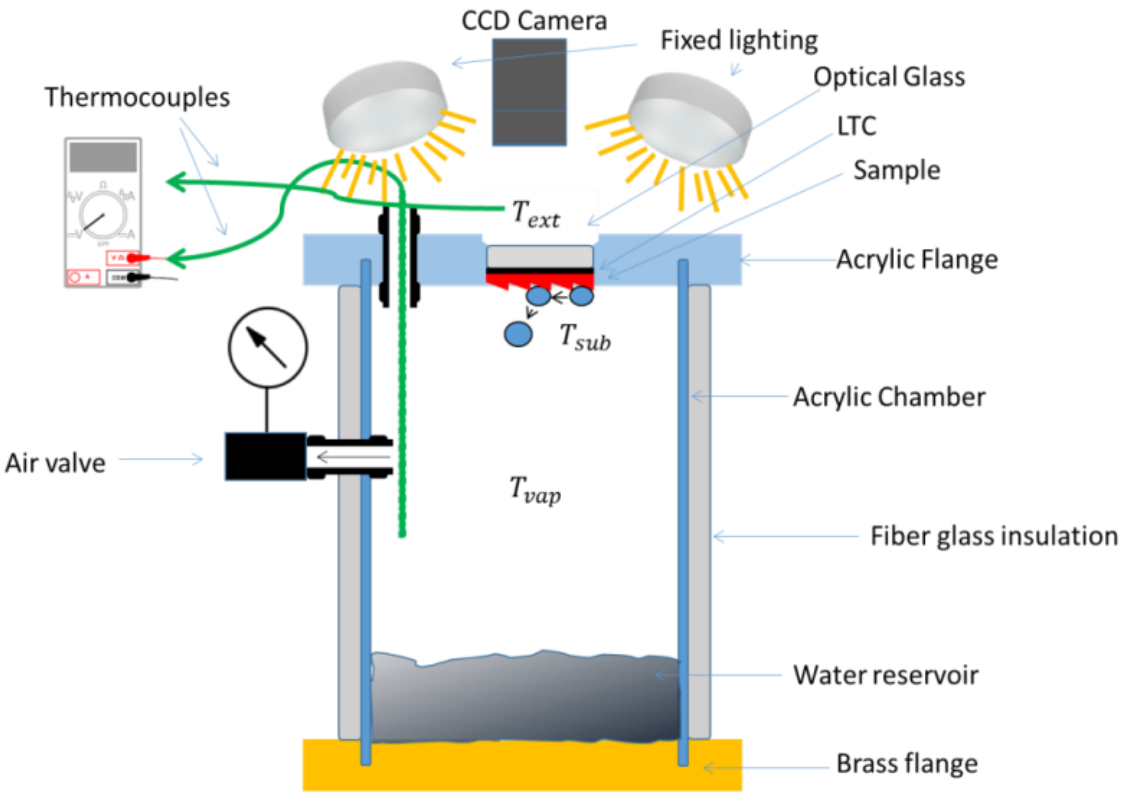

Figure 40. An illustration of the custom condensation chamber layout.

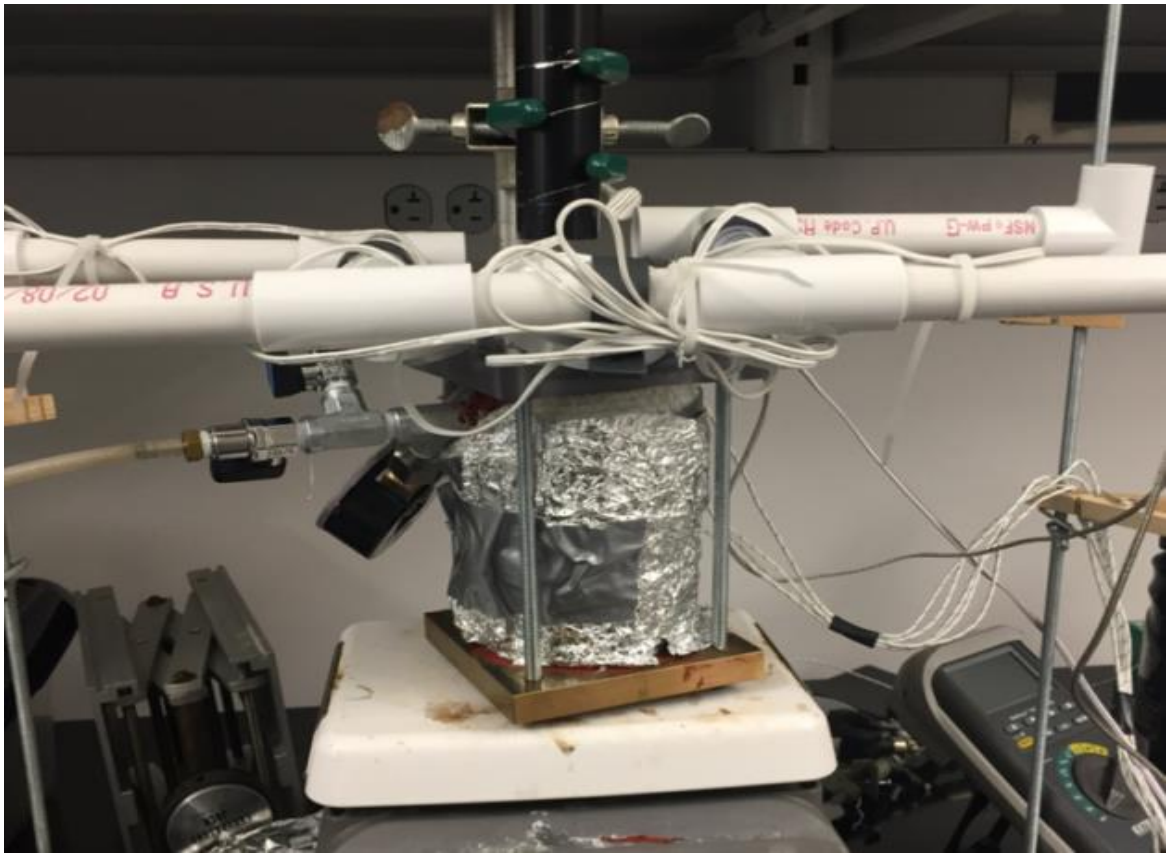

Figure 41. Custom designed condensation chamber.

glass, lighting system set at a constant angle, and a CCD camera connected to a computer.

6.5. Conclusions

Type K thermal couples (OMEGA ® Engineering) are used to determine the temperature for the internal and external environment with the exception of the liquid thermal crystal sheet (Edmund Optics with an activation range of 40-45℃) temperature. The variations between the fabricated chamber and Bansal et al. chamber in Figure 39, is the lack of a cooling channel on the top flange and here, temperature of the bottom brass flange is controlled instead of directly controlling the heat flux shown in Figure 41. A calibrated liquid thermal crystal sheet is adhered to the back side of the sample and is then placed in the chamber as shown in Figure 40. The desired temperature range is reached by turning on the hot plate and allowing an hour

stabilization period to be reached for equilibrium conditions. The vapor temperature is monitored and is and the external temperature as well as a liquid thermal crystal images is captured for each temperature interval. The image is then analyzed using a hue temperature conversion established during the calibration period.

The quantities which are measured and those that are calculated are clearly shown in Figure 49 the constants which pertain to material properties are shown in black, those that are measured or

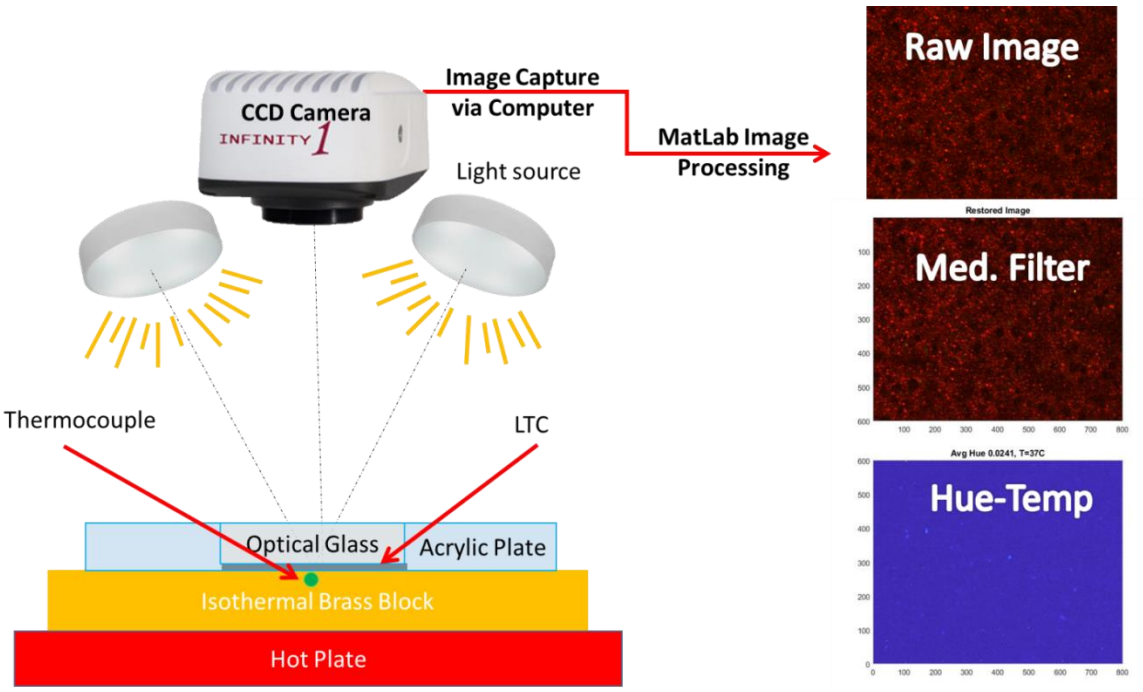

Figure 42. Calibration setup for the conversion of hue to temperature for LTC.

shown in green, and the values which are unknown but can be solved for are in red.

An isothermal brass block is used as a backing substrate for the LTC during calibration to eliminate any unnecessary temperature variation. The lighting and viewing angle are kept at a constant angle throughout the entire duration of the experiment, a simplified illustration of which is shown in Figure 42. Time for temperature stabilization is allowed and an image at each changing mV (read on an EXTECH multi-meter) is taken. The voltage is then converted to

temperature, through a separate calibration method. The images taken by a CCD microscope camera (Lumenera © Infinity 1) are first corrected to get rid of background noise (spitting into separate RGB channels and applying a median filter to each then remerging the image for a corrected one) The corrected mean values of red, green, and blue intensities are exported into a matrix. The image is then converted to a HSI/HSV image where the hue is then extracted. Using these values, a calibration curve is devised. This information provides a direct conversion from a color space to temperature.

Chapter 7. Condensation Heat Transfer Measurements: Liquid Crystal Thermography

7.1. Calibration

A careful calibration procedure is established through precedents in literature (Abdullah, Talib,

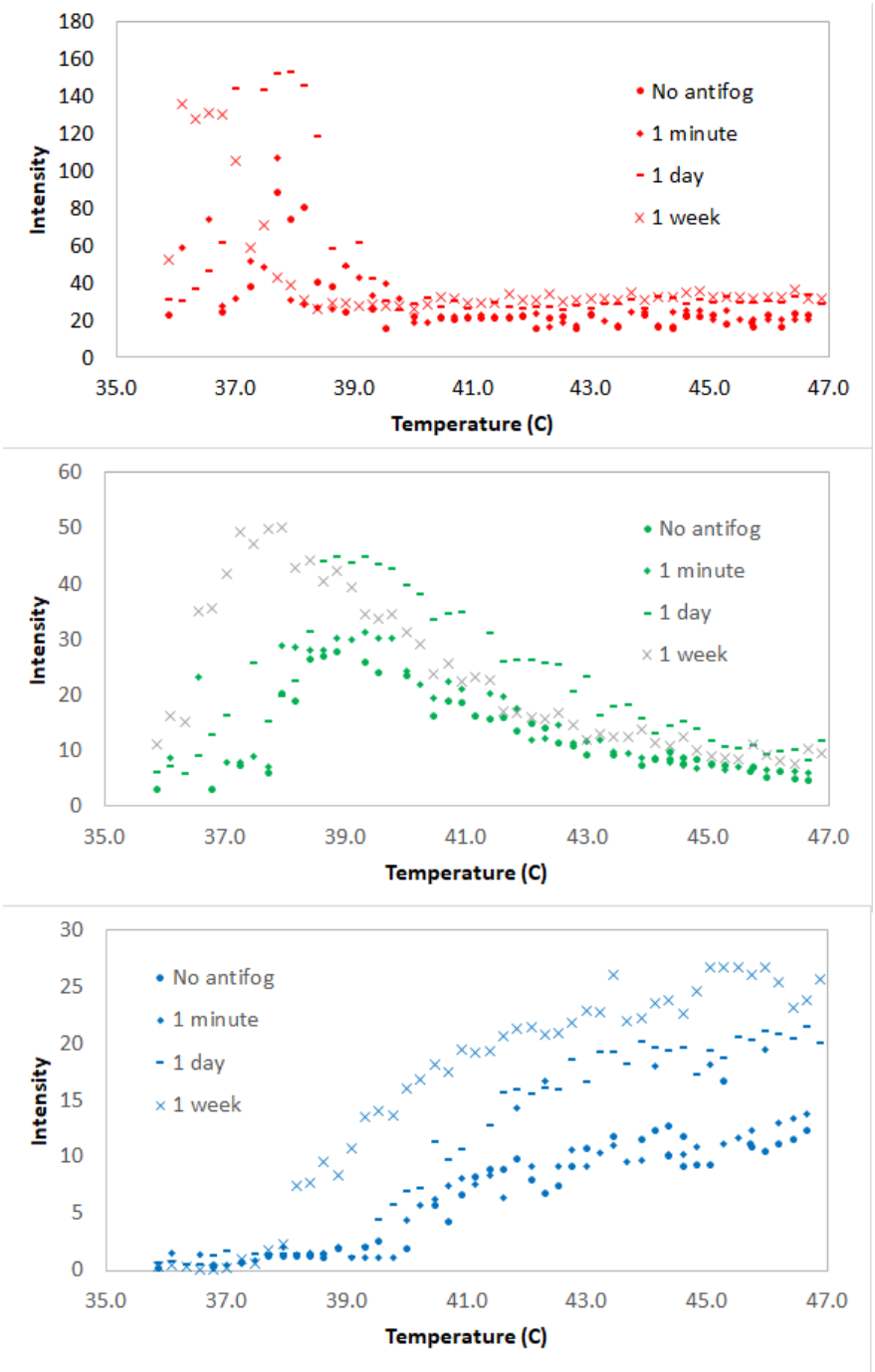

Figure 43. Shifts in red, green, and blue intensities after using anti-fog coating.

Jaafar, & Salleh, 2010) (Anderson & Baughn, 2005) (Baughn, Anderson, Mayhew, & Wolf, 1999) (Hay & Hollingsworth, 1998), cautiously keeping lighting intensity and angle constant. First, temperature is changed in small increments and images are captured at each change to determine the relationship between hue and temperature. Upon initial experiment, the space between the viewport and the LTC sheet became obstructed by unwanted condensates. Implementation of Rain-X™ Anti-Fog decreased their presence; further investigation showed that the coating changed the intensity of the colors over time as show in Figure 43. To avoid this change in intensity, the old coating is removed with ethanol and a new coat of anti-fog coating is applied upon each change of sample. Upon conversion of Hue to temperature, the calibration curve is devised. It is clear for the activation range begins at around 36 ℃ and ends at about

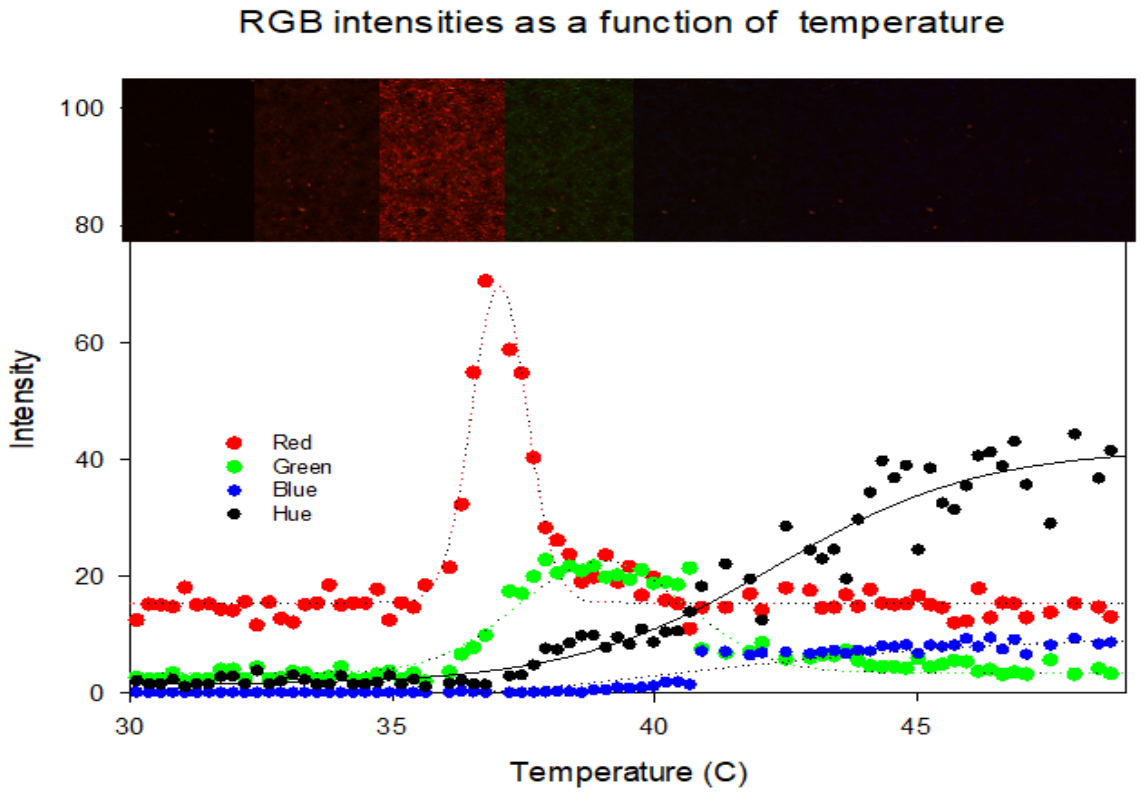

Figure 44. Calibration curve for LTC.

46℃, which is a wider band than anticipated (activation range is from 40℃ − 45 ℃) however different ions between temperature ranges can still be made due to the unique hue values for each temperature interval captured at a tenth of degree due to the usage of a linear mV conversions established using a digital multi-meter. A dominant red intensity remains after the red activation zone, a new lighting (with different color temperature) may help improve the prominence of each RGB intensity; regardless, there is still a discernable hue variation which fits a 5^{th} order polynomial as anticipated by Hay and Hollingsworth.

7.2. Substrate Temperature Distribution

Due to the results shown in the direct observation section (5.2.1. Ejection Events in Figure 34),

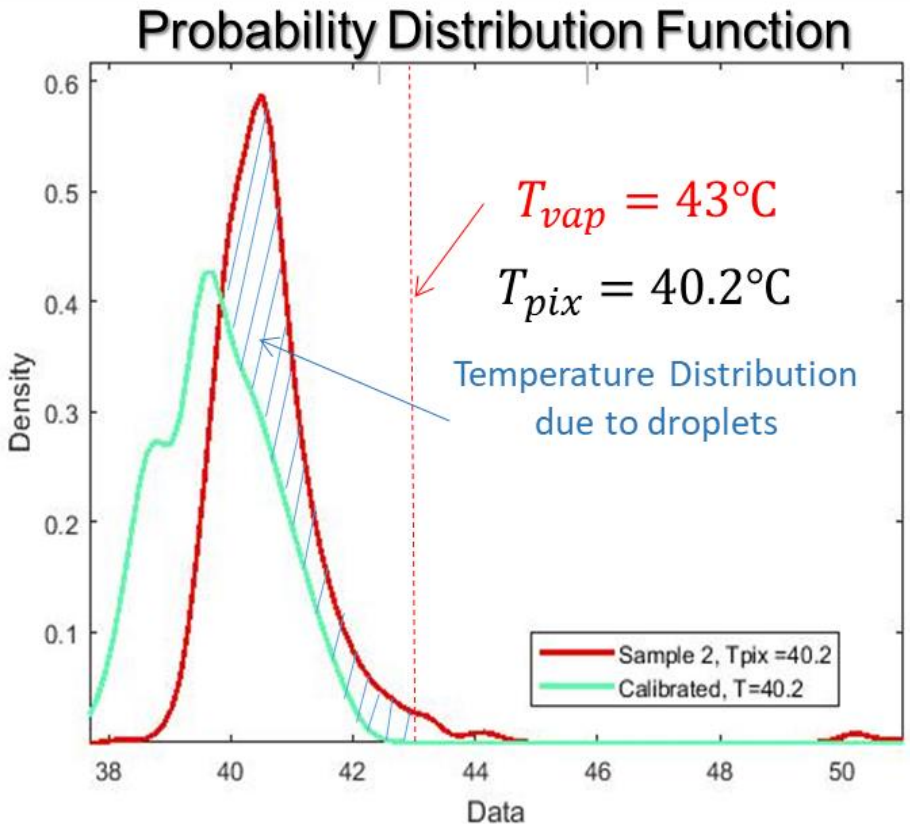

Figure 45. Substrate temperature compared to calibrated temperature distribution.

specifically that the 10um period ratchet produced the second smallest average droplet area with

the 1um period achieving the smallest however these ratchets were obstructed as shown in Figure 24, only 10um period PMMA ratchets and unpatterened PMMA substrates are investigated in the quantification of temperature distribution as well as the quantification of heat transfer. To quantify the substrate temperature, the hue to temperature calibration curve established in Figure

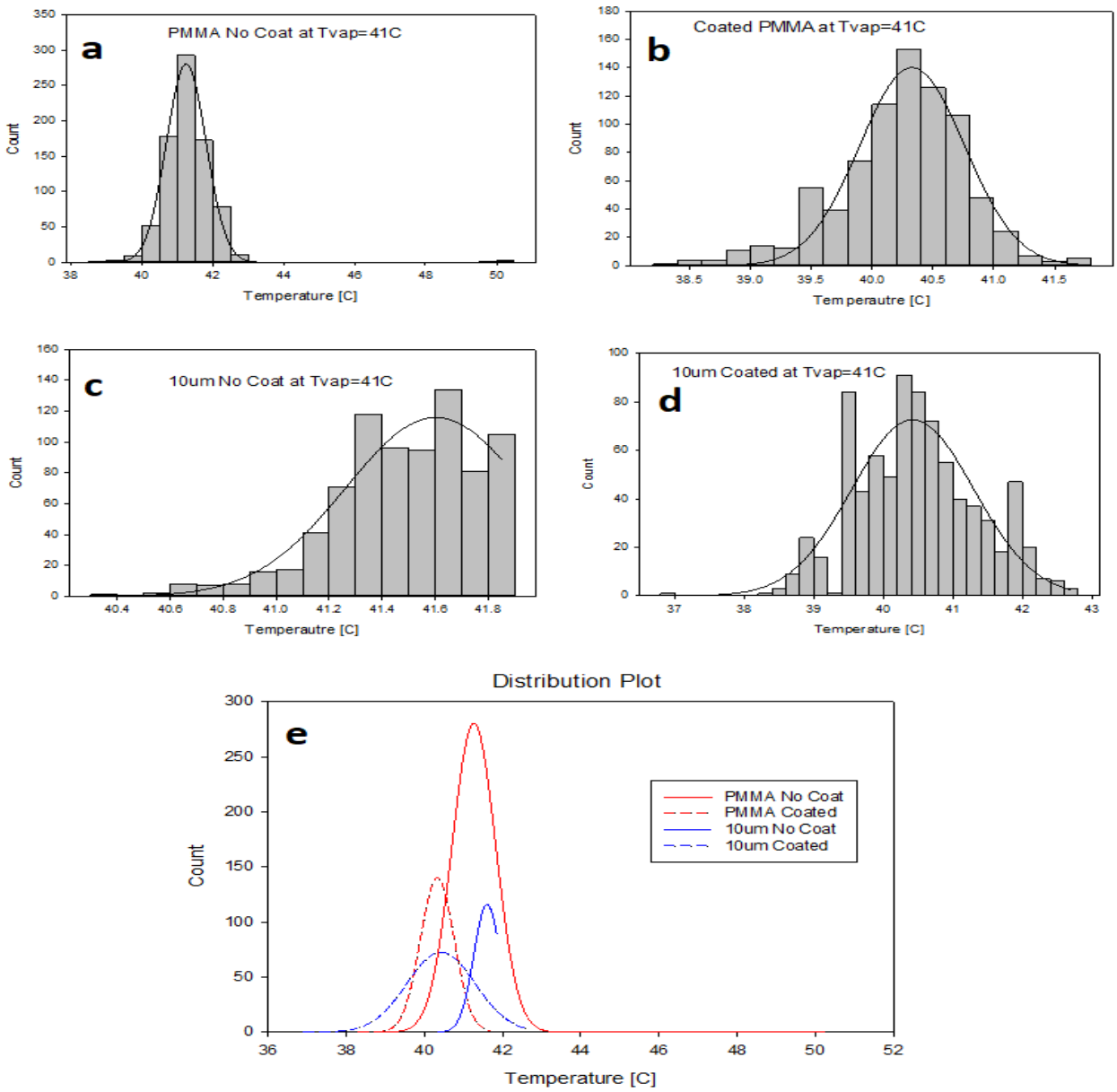

Figure 46. Normal distribution fits of substrate temperature at 41C vapor temperature. (a-d) shows individual distribution fits. e) all normal distrubtion fits.

44 is used. The distribution curves established during calibration where used as standards of comparison to determine the difference in substrate temperature due to the presence of droplets. All measured images show a density/count higher than the calibration curve with non-parametric fits. For example, in Figure 45, the red curve has greater amplitude than the calibrated curve of only using only the LTC sheet. This is potentially due to the larger number of inactive sites due to the surface as parities of the coating, i.e. some of the regions are in the active range where others are not. Slight shifts and multiple peaks show indications of varied distributions potentially indicating the presence of droplets. However, no individual droplets were identified in the form of stark hue difference on surface plots such as in Figure 47, only boundaries between LTC agglomerate.

Increasing the temperature difference between the heat transferring surfaces and the vapor may allow for more salient features such as droplet boundaries to be identified. The amplitude variation among the various substrates can be due to the nonhomogeneous nature of the surface. Considering the largest amplitude is exhibited in the uncoated PMMA sample, a flat substrate, adding a layer makes the substrate more thermal resistive as expected shown in Figure 46. Adding a superhydrophobic coating also increases the physical texture of the substrate, increasing the local temperature gradient, evident in Figure 46 in the variation between inset *a* and *b*. This can attributed to the lower density count, while some of the LTC are displaying a hue consistent with the temperature range, some of the LTCs may still show an inactive range (displaying a black color). Adding texture such as surface roughness or ratchet features, can increases temperature gradient even slightly. Another potential cause is the wetting behavior exhibited on the substrates.

7.2.1. Mid-plane temperature

To match the temperature distribution to the image, a mid-plane temperature is mapped for samples at which the vapor temperature is at 41 ℃, well into the activation range. Two further planes are extracted to better quantify the distribution behavior and these maps are shown in Figure 47. The inset *c*, shows the distribtuion of each plane. In this example, the distribution is

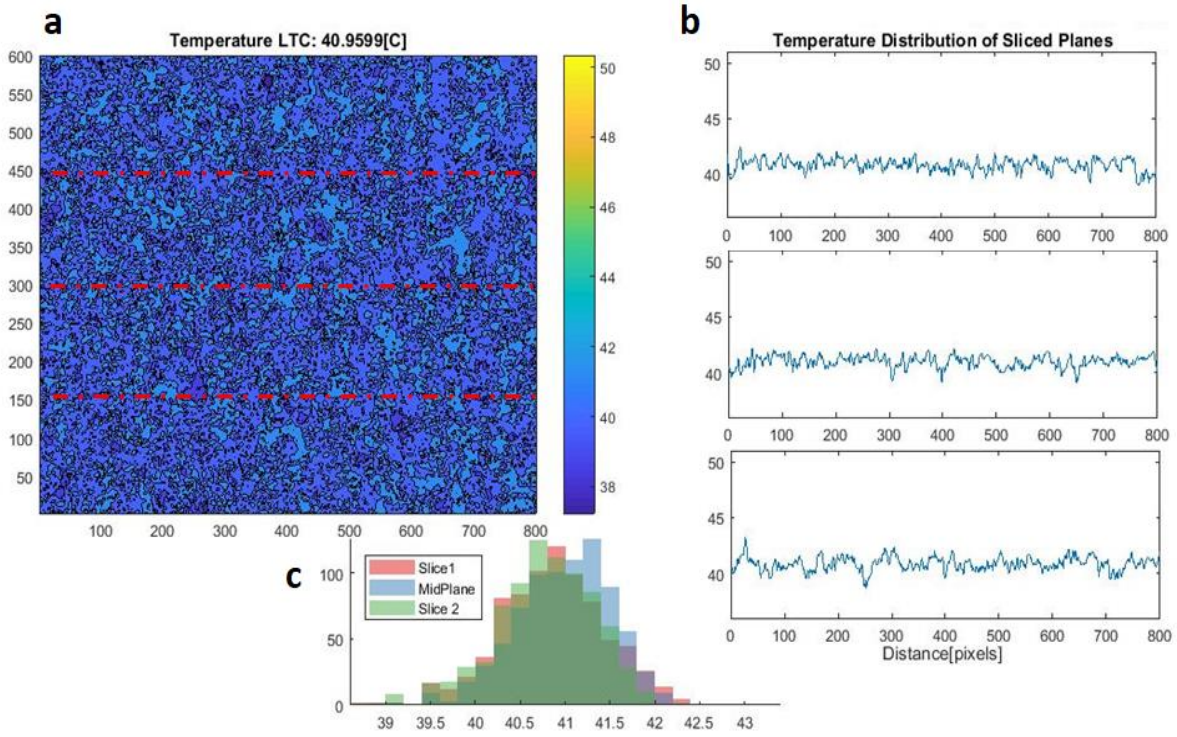

Figure 47. a) surface contour plot displaying temperature of an uncoated PMMA substrate b) temperature distribution of the red sections on a. c) temperature distribution of the sections of interest.

normal and fairly consistent amongst each plane. Very clear peaks can be identified for blank unpatterend PMMA and 10um coated. The other two samples show a relatively sporadic display of temperature variation throughout the mid-plane. The uncoated 10um period ratchets showed a baseline temperature of approximately 41.8℃, with temperature variations dropping to 40.2℃. The coated PMMA sample shows similar behavior. These two samples display a relatively small temperature variation whereas the unpatterened uncoated PMMA and the 10um coated show a

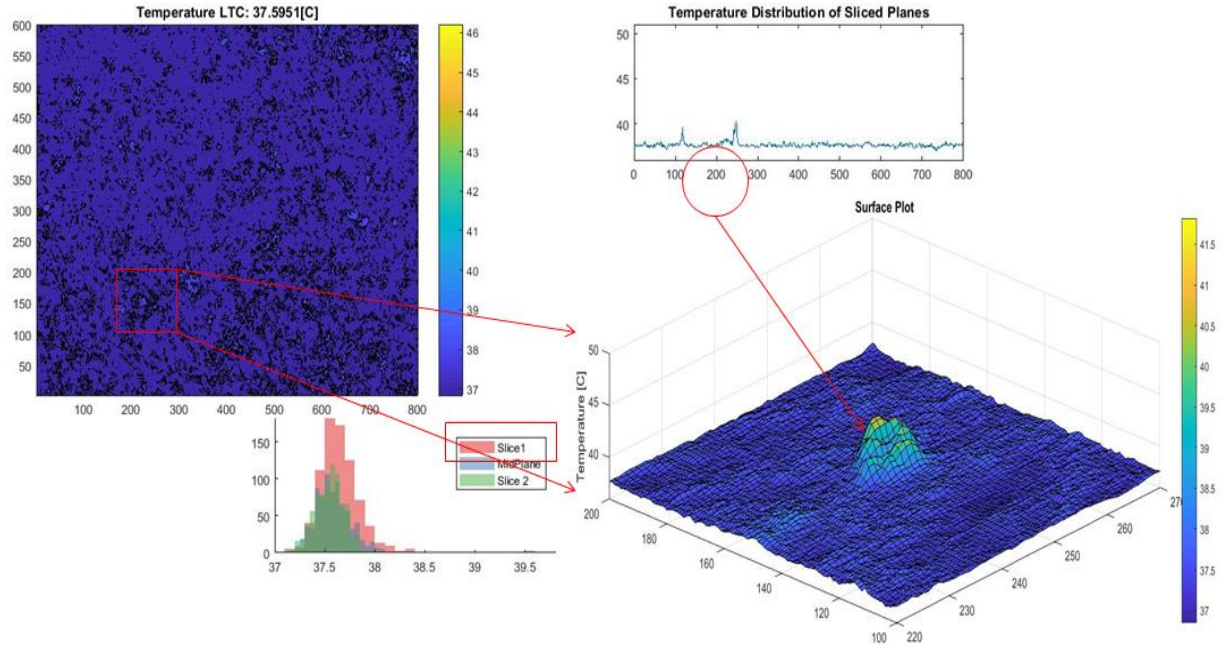

Figure 48. Example of a rapid change in temperature contour on a substrate.

variation of approximately 10℃. It is difficult to assess whether or not these vast differences are due to the presence of droplets. An example of a surface asperity is shown in Figure 48 **Error! Reference source not found.**. One can see that the maximum temperature difference between the peak and the surrounding area is approximately 3℃. Overall, the error for the sample groups are as follows, the largest for uncoated PMMA ±1.9℃, 10um coated ± 0.6℃, uncoated 10um ±0.5 ℃, and finally coated PMMA with ±0.4℃.

7.3. Heat Transfer

Measured quantities, constants, and unknown values, are shown in green, black, and red text respectively in Figure 49.

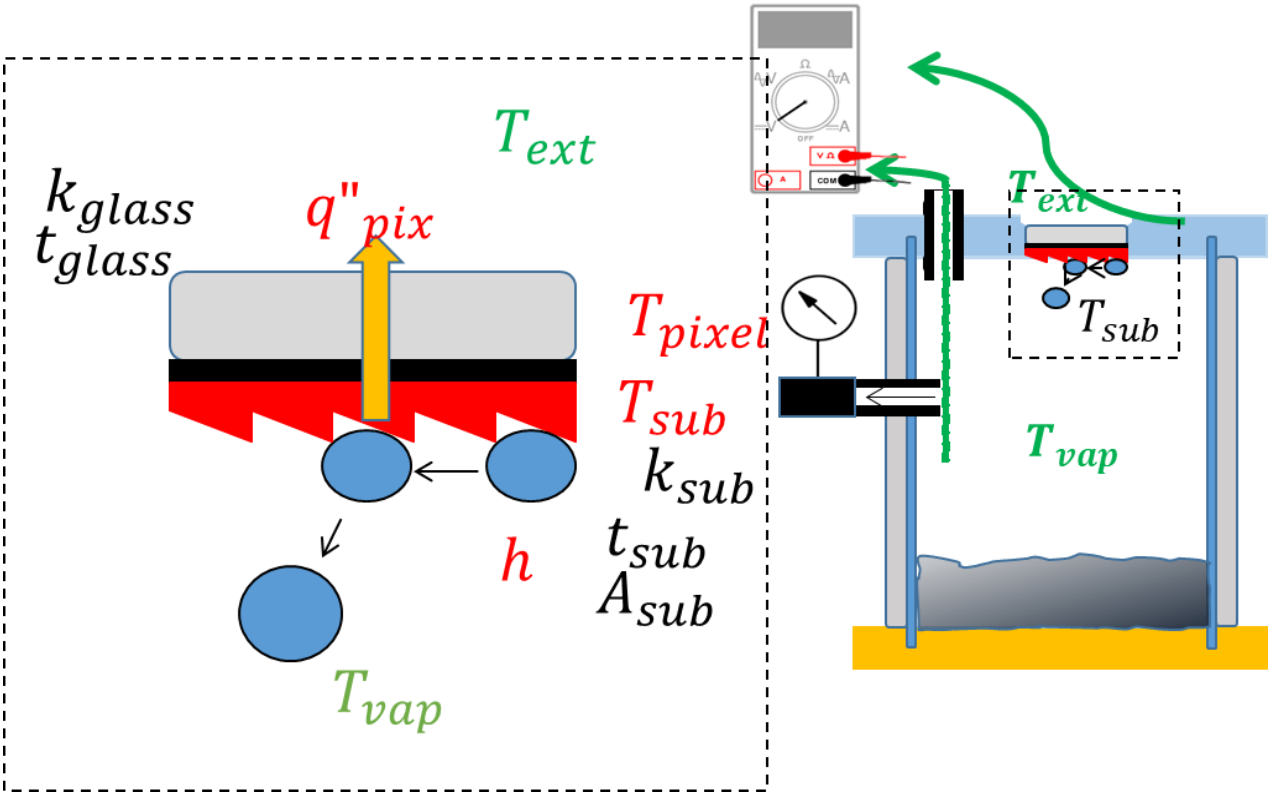

Figure 49. Schematic showing the measured and calculated values for heat transfer through a substrate in condensation.

To quantify heat transfer, a one dimensional approach is used throughout the entire system, where the instantaneous local heat flux through a single pixel area of the substrate is:

(7.2)

$$q"_{pix} = \frac{\dot{Q}_{pixel}}{A_{Pixel}} = k_{glass}\frac{T_{pix} - T_{ext}}{t_{glass}}$$

Where $\dot{Q}_{pixel}$ and A_{Pixel} are defined as the pixel heat transfer rate and the area of single pixel. The equivalent relationship which is issued includes the observation glass properties k_{glass} and

t_{glass} which are the thermal conductivity and the thickness of the glass. The temperatures denoted are of measured external temperature T_{ext} juxtapose the outside environment of the glass and unknown quantity of T_{pix}, which can be found by converting the hue to temperature for an individual pixel based on the calibration curve in Figure 44.

To find the heat transfer coefficient the following equation can be used

(7.2)

$$h = \frac{\dot{Q}_{Total}}{A_{sub}(T_{vap} - T_{sub})}$$

Such that $\dot{Q}_{Total}$=$q"_{pix} * A_{sub}$, where A_{sub} is the substrate area and T_{vap} is the vapor temperature that is measured by a K-type thermocouple and T_{sub} is equal to the averaged pixel temperature throughout the entire substrate area and can be found using:

(7.3)

$$T_{sub} = T_{vap} - \frac{q"_{pix}(t_{sub})}{k_{sub}}$$

The prominent factors extracted from the direct observation of average droplet area and % area coverage foreshadowed the results of the heat transfer coefficient, specifically referring to Figure 33 and Figure 32 shows that 10um substrates show similar area coverage and average droplet size compared to that of unpatterened PMMA. At lower vapor temperatures uncoated PMMA achieves the highest HTC followed by uncoated 10um ratchets, Coated PMMA, and finally 10um coated ratchets. The largest standard deviation is present in the blank PMMA substrates. A potential cause is due to the FWC wetting behavior, larger since droplet sizes can vary dramatically in this mode depending how rapidly droplet sweeping occurs subsequently affecting

the thermal resistance and thus the heat transfer coefficient. Several papers provide potential explanations for the heat transfer coefficient behavior. (Hwang, et al., 2016) saw a similar trend when comparing hydrophobic and superhydrophobic surfaces, such that the heat transfer coefficient for hydrophobic was unexpectedly higher than that of superhydrophobic surfaces. When this research group observed the condensation behavior under ESEM, there were sticky

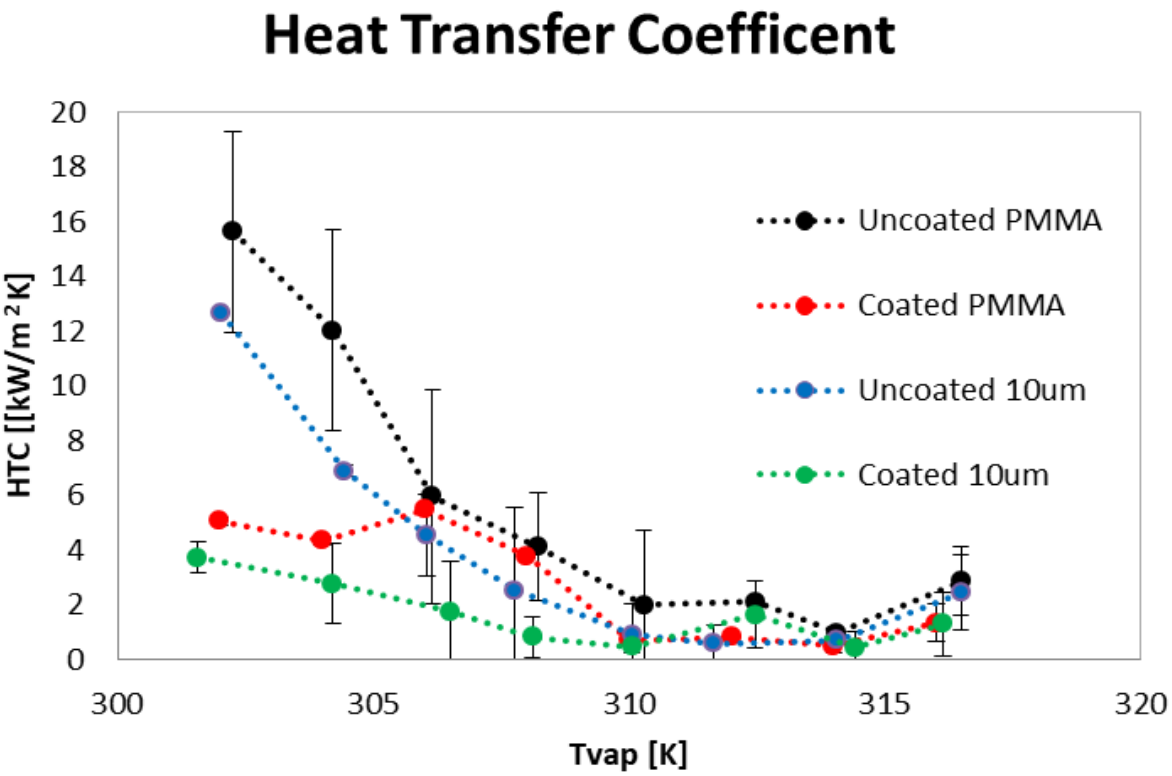

Figure 50. Heat transfer coefficients determined using LTC.

nucleation sites on the SHS as well as relatively large departing droplets due to these adhesion forces which reduced the HTC. The heat flux values were within a few hundred kilowatts per square meter. Another paper (Chen, et al., 2007) compared the heat transfer coefficient for superhydrophobic two-tier, to both hydrophobic and hydrophilic smooth surfaces with the explanation of condensation flooding due to pinning induced by transition into potential Wenzel wetting state. (Miljkovic N. , et al., 2013) show the distinct variations between filmwise,

dropwise, flooded surface, and jumping behavior. The HTC performance is as follows: jumping, dropwise, flooded, and finally filmwise at a chamber pressure of 2700Pa. There appears to be no significant vapor pressure dependence (range of 2-3.5 kPa) on the steady state performance. Another reference (Enright, Miljkovic, Al-Obeidi, Thompson, & Wang, 2012) avoided the flooding phenomena by retaining low subcooling temperatures <0.8K

7.3.1. Heat transfer in a single droplet

Although, the direct and indirect experiments are conducted in different conditions, it is reasonable to devise a relationship between droplet density and heat transfer to understand the effectiveness of the surface coating in heat transfer. The current results appear conflicting due to the direct observations showing effective droplet removal in response to superhydrophobic surface treatment. The droplet density is a pivotal factor in how efficiently a surface can transfer heat. Including droplet area and droplet area coverage as a factor in the heat transfer coefficient, the uncoated substrates still out-perform the coated substrates with the 10um ratchets achieving the

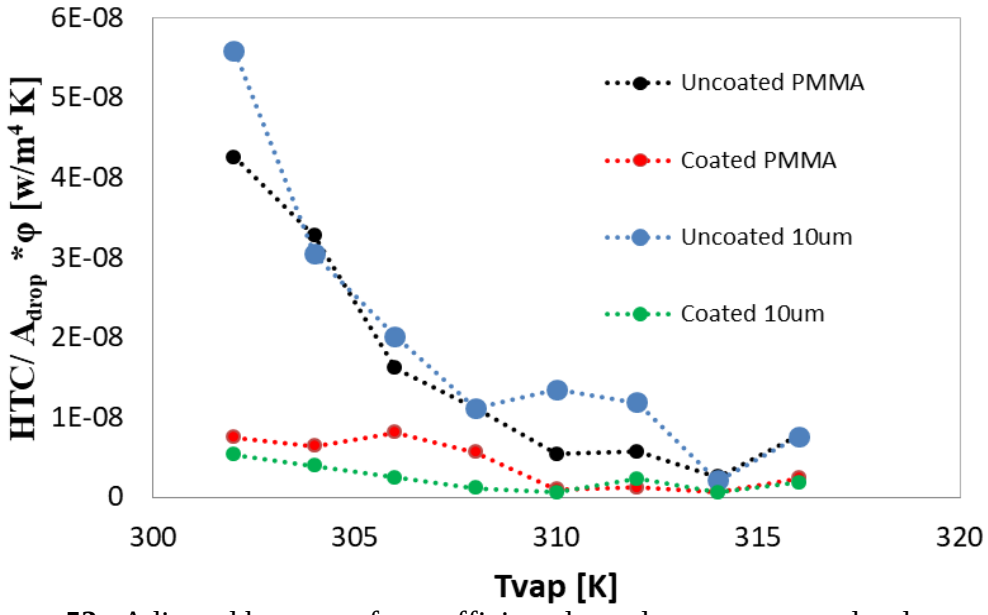

Figure 53. Adjusted heat transfer coefficient dependent on average droplet area and area coverage.

highest performance.

7.4. Superhydrophobic Coating Integrity Post-Experimentation

7.4.1. Wetting Behavior

To understand whether the conditions of the experiments have degraded the surface integrity, wetting behavior following all experiments is observed. Only the dynamic contact angle which

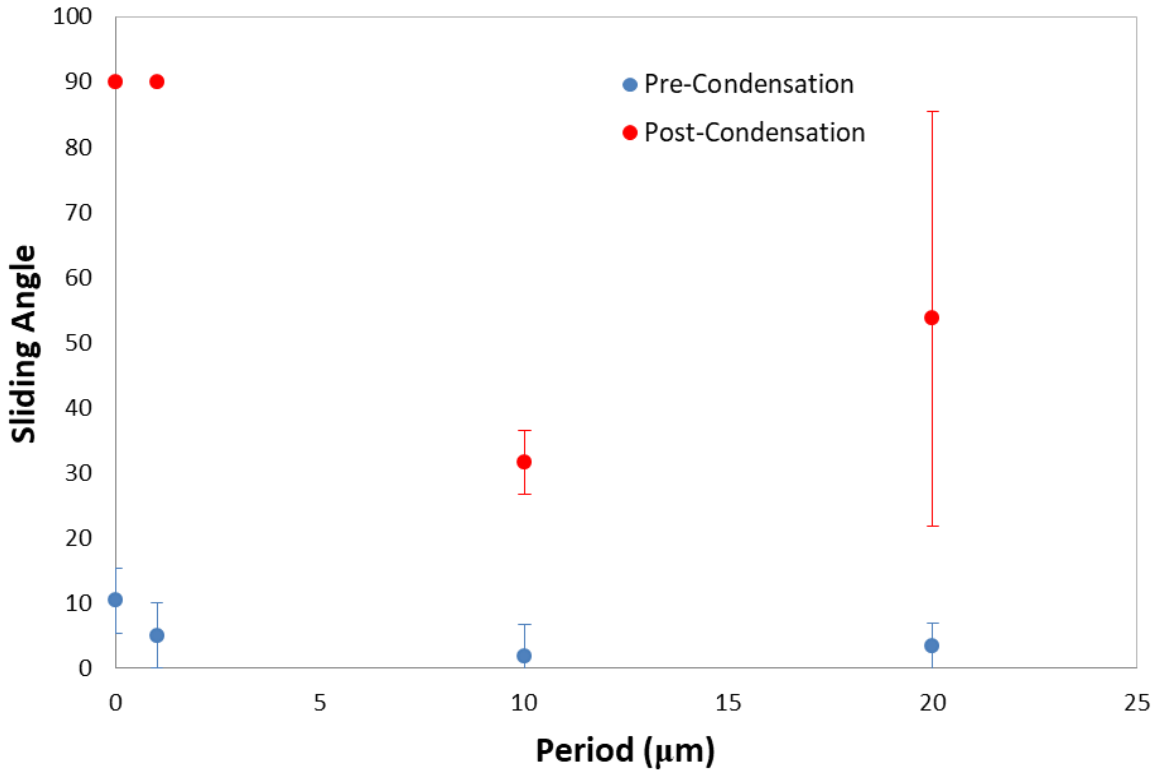

Figure 54. Sliding angle measured before and after all condensation experiments.

directly shows the mobility of the droplet on the surface is measured. From the results one can clearly see that the sliding angle of the droplets on the surfaces change dramatically. There is still a similar trend maintained to that of the pre-condensation phase, with 10µm period producing the lowest sliding angle. Through these results it becomes evident that the surface morphology has changed in some way, to further investigate, SEM images before and after condensation necessary.

7.4.2. SEM Observation

SEM images before and after all condensation experiments were taken, Figure 55 shows that there is some degradation of the surface coating, specifically the thickness which is clearly

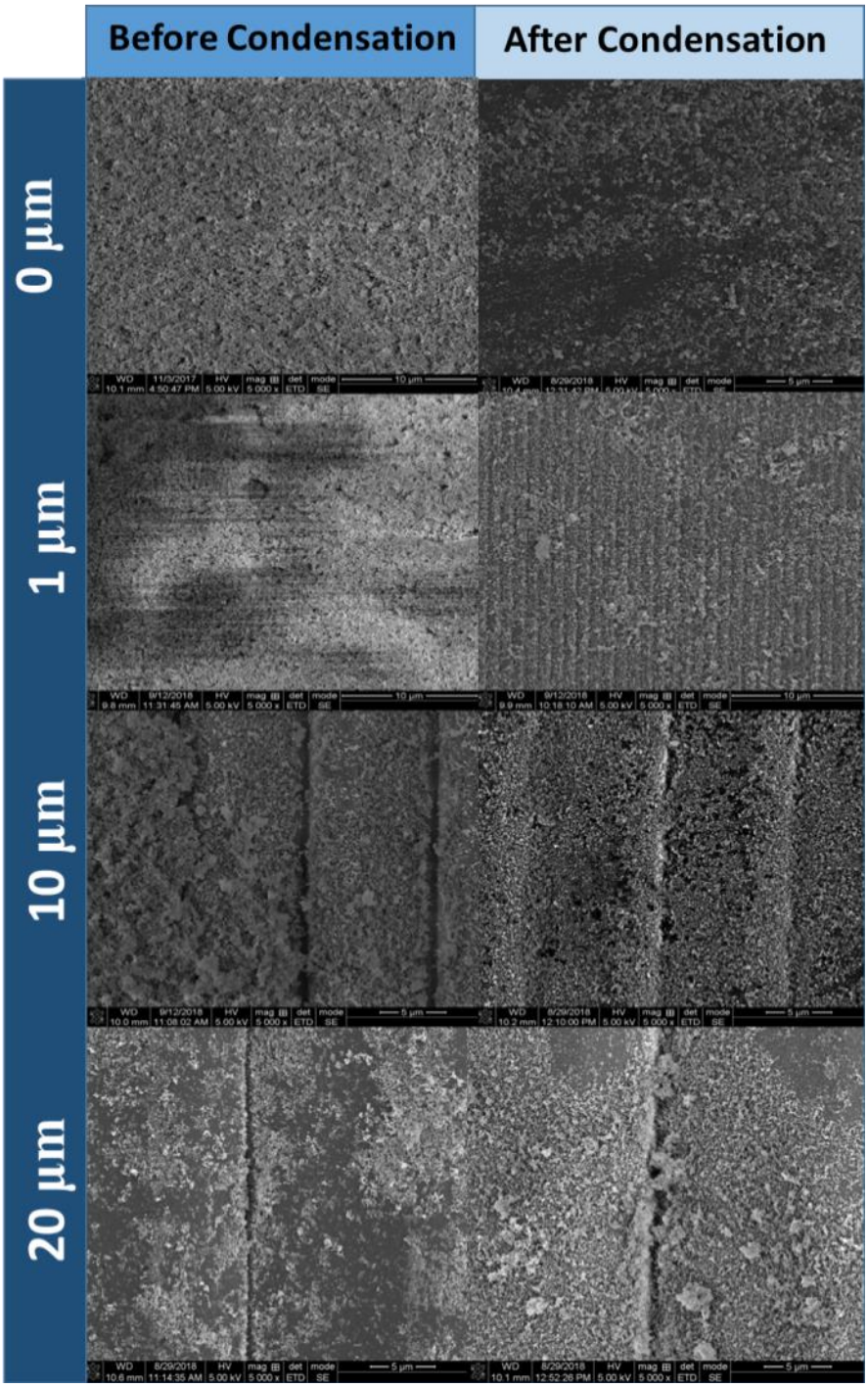

Figure 55. SEM observations before and after all condensation experiments.

evident in the 1μm period ratchets. The surface coating is thick enough to obstruct the ratchets before the experiments; however, following exposure to condensates, the surface has thinned enough to visualize the periodic surface features. For all other surfaces a similar behavior is observed with the exception of the 20μm period, in which the formation of agglomerates appears to be more prevalent. This could be attributed to the average droplet diameters measured during microscope condensation experiments are comparable to the period. Loose particles at the surface are easily swept by droplets and can form into agglomerates where ever the droplet last resided before drying the sample.

Chapter 8. Conclusion and Future Works

8.1. Conclusions

Asymmetric surfaces with ratchet periods of 1, 10, and 20um were successfully fabricated on PMMA substrates using a combination of UV and thermal imprinting. These asymmetric surfaces were able to be modified to have superhydrophobic properties using relatively stable and facile method of dip coating HMDS coated SiO_2 nanoparticles which reduced the % area coverage and overall average droplet size on substrates. Coalescence induced ejection events were observed for coated substrates, in which the droplet ejection diameter remained constant at about 10um. Ratchet period played a role in the number of ejection events for the one minute test intervals, the larger the period the greater the number of ejection events. Various coalescence configurations for ejection events where observed upon further observation, the 20um period outperformed the 10um period in each of these configuration. This is potentially due to larger surface area which allowed for a greater probability of ejection. Further investigation into on the influence of ratchets on coalescence behavior showed a small percentage increase in the horizontal coalescence events (either along ratchets or opposite ratchets) compared to vertical and no displacement events.

In the second experimental setup, liquid crystal thermography, different environmental conditions are utilized compared to that of the condensation observed under the visual light microscope. LTC particles sizes are approximately 5um which is comparable to the ratchet period; therefor, no prominent discernable asymmetric surface temperature effects could be observed. There are no visible individual droplet boundaries either due the droplet being the same order of magnitude as the liquid crystals or the condensing vapor temperature does not induce a large enough temperature difference to that of the cooler substrate. Measuring heat

transfer coefficient as a function of vapor temperature revealed that the ratchets unexpected reduced the HTC value compared to an unpatterened PMMA substrate. The presence of a coating further deterred the efficiency. Some potential causes for this unexpected behavior could be the following: the substrates do not have long term stability in maintaining superhydrophobic wetting behavior and switch from Cassie-Baxter state to Wenzel state. The potential presence of NCGs could render the performance of DWC unfavorable compared to FWC. FWC is expected and observed on the uncoated substrates in direct observation. After an hour (similar time from to the indirect observations) time lapse video was taken of 10um period coated sample, it appears that the wetting behavior maintains its integrity but again the direct observation experiment using the visual light microscope (cooling block set to 2℃, and environment is at ambient conditions: 20℃ with RH at 36%) is a different condition than the condensation chamber using liquid crystal thermography (30-45℃ vapor temperature range with 100%RH). After analyzing wetting behavior post condensation experiments, one can see that the wetting behavior degrades potentially due to the surface coating thinning as observed in SEM images.

8.2. Future Work

Preliminary investigations have been made on improving the wetting behavior without adding a coating that can introduce an unwanted thermal resistance, the most promising of which is nanosphere lithography using a self-assembly monolayer of polystyrene (PS) nanospheres. These nanospheres act as a mask to create tiny bumps very clearly seen in Figure 56 on the surface of interest using a reactive ion etching process. The difficulty lies in achieving a large

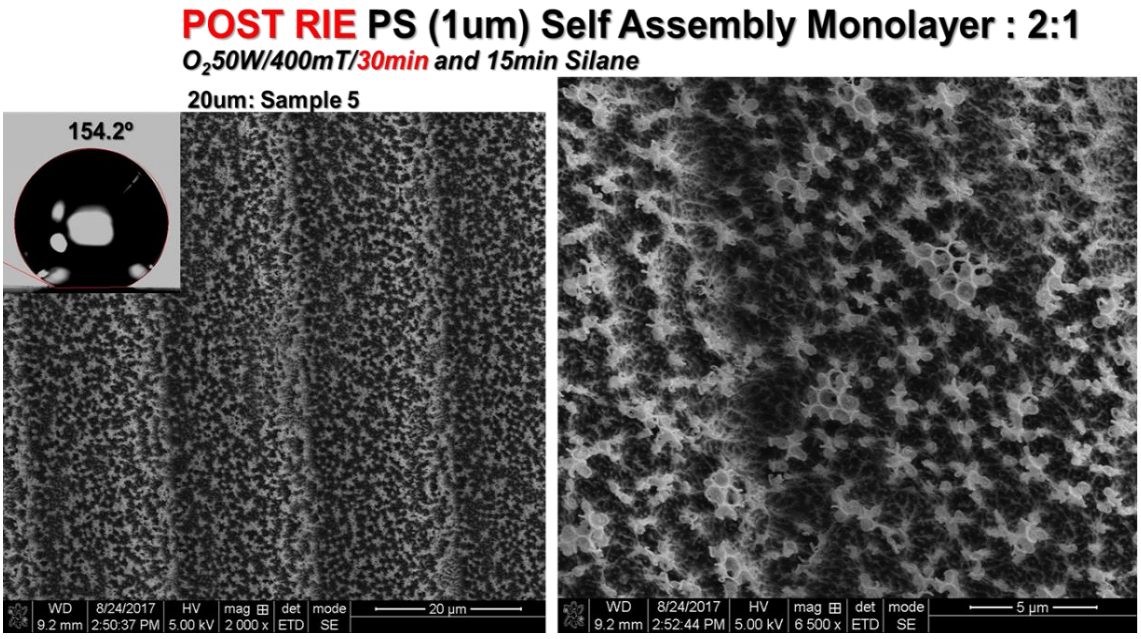

Figure 56. SEM images of nanosphere lithography using PS nanospheres.

homogenous area. Changing the dispersion solution systematically may allow for a better surface coating.

Another future improvement includes a modified condensation chamber in which vapor flow can be controlled to avoid surface flooding. In order to do this a separate chamber housing the fluid as well as a drainage system to reintroduce the same fluid can be fabricated with a flow control valve. All of which can be achieved using the basic design of Figure 57. However the most beneficial way to conduct a combination experiments, specifically direct observation of droplets

and indirect observation of the temperature profile on the backside of the substrate though liquid crystal thermography, is to have cameras on both sides of the apparatus. The presence of a cooling fluid channel on the backside may hinder this .A cooling channel needs to be designed in such a way that it does not obstruct the liquid thermal crystal and it does not introduce any obstruction to the data due to the flow field of the coolant.

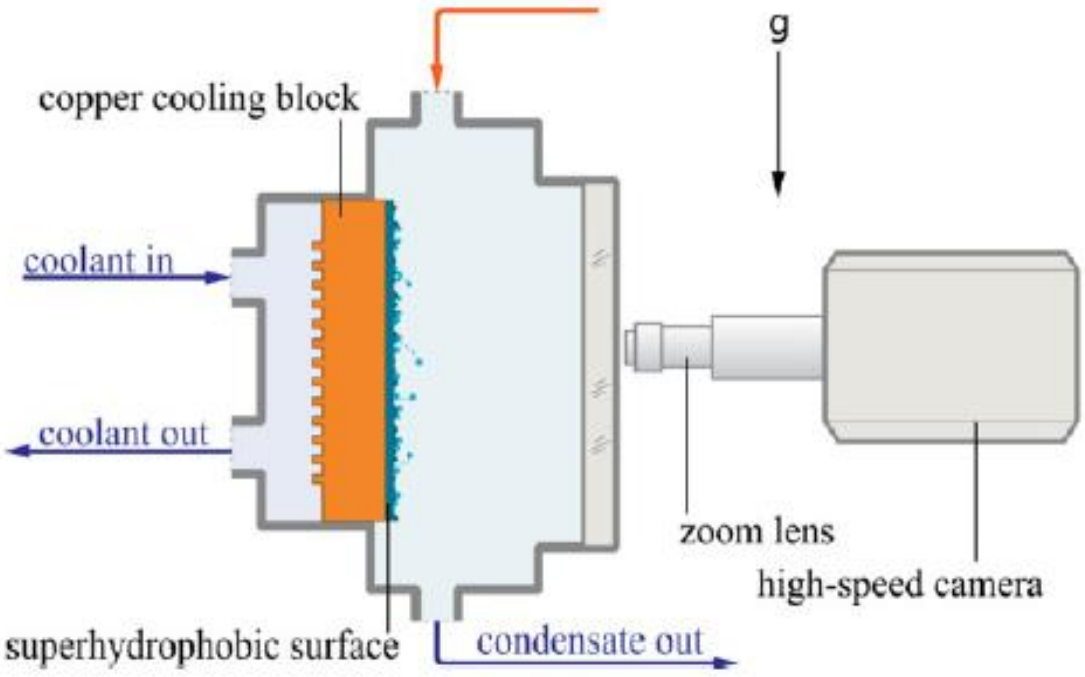

Figure 57. Condensation chamber fabricated by (Rykaczewski, et al., 2013).

Bibliography

(n.d.). Retrieved from Hiveminer: https://hiveminer.com/Tags/africa%2Ctenebrionidae

Abdullah, N., Talib, A. R., Jaafar, A. A., & Salleh, M. M. (2010). The basics and issues of Thermochromic Liquid Crystal Calibrations. *Experimental Thermal and Fluid Science*, 1089-1121.

Anderson, M. R., & Baughn, J. W. (2005). Liquid-Crystal Thermography: Illumination Spectral Effects. Part1-Experiments. *Journal of Heat Transfer*, 581-587.

Bansal, G. D., Khandekar, S., & Muralidhar, K. (2009). Measurement of Heat Transfer During Dropwise Condensation of Water on Polyethylene. *Nanoscale and Microscale Thermophysical Engineering*(13), 184–201.

Baughn, J. W., Anderson, M. R., Mayhew, J. E., & Wolf, J. D. (1999). Hysteresis of Thermochromic Liquid Crystal Temperature Measurement Based on Hue. *Journal of Heat Transfer*, 1067-1072.

Bergaman, T. L., Lavine, A. S., Incropera, F. P., & Dewitt, D. P. (2011). *Introdution to Heat Transfer*. Hoboken: John Wiley & Sons, Inc.

Boreyko, J. B., & Chen, C. H. (2013). Vapor Chambers with Jumping-Drop Liquid Return from Superhydrophobic Condensers. *Int. J. Heat Mass Transfer*, 409-418.

Boreyko, J. B., Zhao, Y., & Chen, C. H. (2011). Planar Jumping-Drop Thermal Diodes. *Applied Physics Letters*, 23105.

Boreyko, J., & Chen, C.-H. (2009). Self-Propelled Dropwise Condensate on Superhydrophobic Surfaces. *PRL 103*, 184501.

Brumfield, L. (2014). Experimental and Numerical Study of the Effects of Asymmetric Micro Ratchets on Pool Boiling. *Diss. Louisiana U, Baton Rouge*.

Celia, E., Darmanin, T., Givenchy, E. T., Amigoni, S., & Guittard, F. (2013). Recent advances in designing superhydrophobic surfaces. *Journal of Colloid and Interface Science*, 1-18.

Chamakos, N. T., Karapetsas, G., & Papathanasiou, A. G. (2016). How asymmetric surfaces induce directional droplet motion. *Colloids and Surfaces A: Physicochemical and Engineering Aspects*, 180-189.

Chang, K. C., Chuang, T. L., Ji, W. F., Chang, C. H., Peng, Y. Y., Shih, H., . . . Su, Y. C. (2015). UV-curable nanocasting technique to prepare bioinspired superhydrophobic organic-inorganic composite anticorrosion coatings. *Express Polymer Letters*, 143-153.

Chen, C.-H., Cai, Q., Tsai, C., Chen, C.-L., Xiong, G., Yu, Y., & Ren, Z. (2007). Dropwise condesnation on supherhydrophobic surfaces with two-tier roughness. *Applied Physics Letters*, 1-4.

Cheng, J., Vandadi, A., & Chen, C.-L. (2012). Condensation heat transfer on two-tier superhydrophobic surfaces. *Appl. Phys Lett. 101*, 131909.

Cho, R. (2011, March 7). *The Fog Collectors: Harvesting Water From Thin Air*. Retrieved January 11, 2017, from State of the Planet: http://blogs.ei.columbia.edu/2011/03/07/the-fog-collectors-harvesting-water-from-thin-air/

Chow, D. (2013, April 30). *Cicada Grooming Habits: Insects Use 'Jumping' Water Droplets To Self-Clean*. Retrieved September 17, 2017, from HuffPost: http://www.huffingtonpost.com/2013/04/30/cicada-grooming-habits-invasion-2013_n_3187175.html

Comanns, P., Buchberger, G., Buchsbaum, A., Baumgartner, R., Kogler, A., Bauer, S., & Baumgartner, W. (2015). Direction, passive liquid transport: the Texas horned lizard as a model for a biomimetic 'liquid diode'. *Journal of the Royal Society* .

Comanns, P., Buchberger, G., Buchsbaum, A., Baumgartner, R., Kogler, A., Bauer, S., & Baumgartner, W. (2015). Directional, passive liquid transport: the Texas horned lizard as a model for a biomimetic 'liquid diode'. *Royal Society* .

Daniel, S., & Chaudhury, M. K. (2002). Rectified Motion of Liquid Drops on Gradient Surfaces Induced by Vibration. *Langmuir*, 3404-3407.

Enright, R., Miljkovic, N., Al-Obeidi, A., Thompson, C. V., & Wang, E. N. (2012). Condensation on Superhydrophobic Surfaces: The Role of Local Engery Barriers and Struture Length Sclae. *Langmuir*, 1-9.

Gao, S., Liao, Q., Liu, W., & Liu, Z. (2018). Coalescence-Induced Jumping of Nanodroplets on Textured Surfaces. *The Journal of Physical Chemistry Letters*, 13-18.

Glicksman, L. R., & Hunt, A. W. (1972). Numerical Simulation of Dropwise Condensation. *Int. J. Heat Mass Transfer*, 2251-2269.

Graham, C., & Griffith, P. (1973). Drop Size Distributions and Heat Transfer in Dropwise Condensation. *Int. J. Heat Mass Transfer* , 337-346.

Guo, P., Zheng, Y., Liu, C., Ju, J., & Jiang, L. (2012). Directional shedding-off of water on natural/bio-mimetic taper-ratchet array surfaces. *Soft Matter*, 1770-1775.

Hay, J., & Hollingsworth, D. K. (1998). Calibration of micro-encapsultated liquid crystals using hue angleand a dimensionless temperture. *Experimental Thermal and Fluid Science*, 251-257.

Hou, Y., Yu, M., Chen, X., Wang, Z., & Yao, S. (2015). Recurrent Filmwise and Dropwise Condensation on a Beetle Mimetic Surfaces. *ACS Nano*, 71-81.

Hu, H. W., & Tang, G. H. (2014). Theoretical investigation of stable dropwise condensation heat transfer on a horizontal tube. *Applied Thermal Engineering*, 671-679.

Huang, X., Yuan, Y., Shaozhe, L., Wang, W., & Hong, R. (2017). One-step sol-gel preparation of hydrophobic antireflective SiO2 coating on poly(methyl methacrylate) substrate. *Elsevier: Materials Letters*, 62-64.

Huang, Z., Hwang, Y., & Radermacher, R. (2017). Review of nature-inspired heat exchanger technology. *International Journal of Refrigeration 78* , 1-17.

Hurst, S. M., Farshchian, B., Choi, J., Kim, J., & Park, S. (2012). A universally applicable method for fabricating superhydrophobic polymer surfaces. *Elsevier*, 85-90.

Hwang, H. S., Shim, J. K., & Park, I. (n.d.). Superhydrophobic Surfaces from a Spray Coating Process. *18TH INTERNATIONAL CONFERENCE ON COMPOSITE MATERIALS*.

Hwang, K. W., Kim, D., Jo, H., Park, H. S., Moriyama, K., & Kim, M. H. (2016). Effects of heat flux on dropwise condensation on a superhydrophobic surface. *Jounal of Mechanical Science and Technology 30*, 2141-2149.

Ireland, P. T., Neely, A. J., Gillespie, D. H., & Robertson, A. J. (1999). Turbulent heat transfer measurements using liquid crystals. *International Journal of Heat and Fluid Flow vol. 20*, 355-367.

Kabeel, A. E., Hamed, A. M., & El-Agouz, S. A. (2010). Cost analysis of different solar still configurations. *Elsevie: Energy, 35*, 2901-2908.

Kakade, V. U., Lock, G. D., Wilson, M., Owen, J. M., & Mayhew, J. E. (2009). Accurate heat transfer measurements using thermochromic liquid crystal. Part 1: Calibration and characteristics of crystals. *International Journal of Heat and Fluid Flow*, 939-949.

Kakade, V. U., Lock, G. D., Wilson, M., Owen, J. M., & Mayhew, J. E. (2009). Accurate heat transfer measurements using thermochromic liquid crystal. Part 2: Application to a rotating disc. *International Journal of Heat and Fluid Flow 30*, 950-959.

Keyanfar, K., & Becker, D. (2012, April 16). Simple Fabrication of a Superhydrophobic Surface.

Kim, S., & Kim, K. (2011). Dropwise Condensation Modeling Suitable for Supherhydrophobic Surfaces. *Heat Transfer*, 133.

Lagubeau, G., Le Merre, M., Clanet, C., & Quere, D. (2011). Leidenfrost on ratchet. *Nature Physics Letters*, 395-398.

Lee, M. J., Lee, N. Y., Lim, J. R., Kim, J. B., Kim, M., Baik, H. K., & Kim, Y. S. (2006). Antiadhesion Surface Treatments of Molds for High-Reolution Unconventional Lithography. *Advanced Materials*, 3115-3119.

Lee, N. Y., & Kim, Y. S. (2007). A poly(dimethylsiloxane)-coated flexible mold for nanoimprint lithography. *Nanotechnology 18*, 415303.

Lee, S., Cheng, K., Palmre, V., Bhuiya, M. H., & Kim, K. J. (2013). Heat transfer measurement during dropwise condensation using micro/nano-scale porous surface. *International Journal of Heat and Mass Transfer 65*, 619-626.

Lin, Y.-T., & Chou, J.-H. (2015). A facile low-temperautre and low-cost process for fabricating super-hydrophobic surface on acrylic. *Journal of Material Science*, 6624-6630.

Linke, H., Aleman, B. J., Melling, L. D., Taormina, M. J., Francis, M. J., Hygelund, C. C., . . . Stout, A. (2006). Self-Propelled Leidenfrost Droplets. *Physical Review Letters 96*, 154502.

Liu, C. C., Ju, J., Zheng, Y., & Jiang, L. (2014). Asymmetric Ratchet Effect for Directional Transport of Fog Drops on Static and Dynamic Butterfly Wings. *ACS Nano*, 1321-1329.

Luo, Y., Li, J., Zhu, J., Zhao, Y., & Gao, X. (2015). Fabrication of Condensate Microdrop Self-Propelling Porous Films of Cerium Oxide Nanoparticles on Copper Surfaces. *Angew. Chem. Int. Ed.54*, 4876-4879.

Manzoor , H. (2013, November 6). *Lotus effect - superhydrophobic surfaces*. Retrieved May 24, 2016, from YouTube: https://www.youtube.com/watch?v=bFiOkxoXLic

Mendoza, H., Beaini, S., & Carey, V. P. (2014). An Exploration of Transport Within Microdroplet and Nanodroplet Clusters During Dropwise Condensation of Water on Nanostructured Surfaces. *Journal of Heat Transfer, 136*, 1-9.

Miljkovic, N., Enright, R., & Wang, E. (2012). Effect of Droplet Morphology on Growth Dynamics and Heat Transfer during Condensation on Superhydrophobic Nanostructured Surfaces. *ACS Nano, 6*, 1776-1785.

Miljkovic, N., Enright, R., Nam, Y., Lopez, K., Dou, N., Sack, J., & Wang, E. N. (2013). Jumping-Droplet-Enhanced Condensation on Scalable Superhydrophobic Nanostructured Surfaces. *Nano Letters*, 179-187.

Moitsheki, R. J. (2011). Steady one-dimensional heat flow in a longitudinal triangular and parabolic fin. *Commun Nonlinear Sci Numerical Simulat*, 3971-3980.

Nilsson, M. A., Daniello, R. J., & Rothstein, J. P. (2010). A novel and inexpensive technique for creating superhydrophobic surfaces using Teflon and sandpaper. *Journal of Physics D: Applied Physics*.

Ok, J. T. (May 2011). Droplet Motion on Minituraized Ratchets. Baton Rouge: Louisiana State University.

Olceroglu, E., Hsieh, C.-Y., rahman, M., Lau, K. K., & McCarthy, M. (2014). Full-Field Dynamic Characterization of Superhydrophobic Condensation on Biotemplated Nanostructured Surfaces. *Langmuir, 30*, 7556-7566.

Paxson, A. T., Yague, J. L., Gleason, K. K., & Varanasi, K. K. (2014). Stable Dropwise Condensation for Enchancing Heat Transfer via the Initiated Chemical Vapor Deposition (iCVD) of Grafted Polymer Films. *Advanced Materials*, 418-423.

Philipavicius, J., Kazadojev, I., Beganskiene, A., Melninkaitis, A., Sirutkaitis, V., & Kareiva, A. (2008). Hydrophobic Antireflective Silica Coatings via Sol-gel Process. *Materials Science*, 283-287.

Rabinovich, S. (2011). A Simple Theory of Condensation. *Journal of Experimental and Theoretical Physics*, 637-641.

Rao, Y., & Xu, Y. (2012). Liquid Crystal Thermography Measurement Uncertainty Analysis and Its Application to Turbulent Heat Transfer Measurements. *Advances in Condensed Matter Physics*.

Rao, Y., & Xu, Y. (2012). Liquid Crystal Thermograpy Measurement Uncertainty Analysis and Its Application to Turbulent Heat Transfer Measurements. *Advances in Condensed Matter Physics*, 1-8.

Rose, J. W. (1967). On the Mechanism of Dropwise Condensation. *Int. J. Heat Mass Transfer*, 755-762.

Rose, J. W. (2002). Dropwise condensation theory and experiment: a review. *Journal of Power and Energy*, 115-126.

Rykaczewski, K. (2012). Microdroplet Growth Mechanism during Water Condensation on Supherhydrophobic Surfaces. *Langmuir*, 1-10.

Rykaczewski, K., Paxson, A. T., Anand, S., Chen, X., Wang, Z., & Varanasi, K. K. (2013). Multimode Multidrop Serial Coalescence Effects during Condensation on Hierarchial Superhydrophobic Surfaces. *Langmuir*, 1-11.

Schmidt, E., Schurig, W., & Sellschopp, W. (1930). Versuche uber die Kondensation von Wasserdampf in Film- und Tropfenform. *Technische Mechanik und Thermodynamik*, 53-63.

Sheng, X., & Jihua, Z. (2011). Directional motion of water drop on ratchet-like superhydrophobic surfaces. *Elsevier: Applied Surface Science*, 6811-6816.

Tanner, D. W., Pope, D., Potter, C. J., & West, D. (1965). Heat transfer in dropwise condensation - Part II surface chemistry. *Int. J. Heat Mass Transfer*, 427-436.

Tanner, D. W., Potter, C. J., Pope, D., & West, D. (1965). Heat transfer in dropwise condensation - Part 1 The effects of heat flux, steam velocity and non-condesable gas concentration. *Int. J. Heat Mass Transfer*, 419-426.

Vemuri, S., & Kim, K. J. (2006). An experimental and theoretical study on the concept of dropwise condensaiton. *Int. J. Heat Mass Transfer*, 649-657.

Vemuri, S., Kim, K. J., Wood, B. D., Govindaraju, S., & Bell, T. W. (2006). Long term testing for dropwise condensation using self-assembly monolayer coatings of n-octadecyl mercaptan. *Appl. Therm. Eng.*, 421-429.

Vorobyev, A. Y., & Guo, C. (2015). Multifunctional surfaces produced by femtosecond laser pulses. *Journal of Applied Physics*, 117.

Wang, D., Zhao, A., Li, L., He, Q., Guo, H., Sun, H., & Gao, Q. (2015). Bioinspired ribbed hair arrays with robust superhydrophobicity fabricated by micro/nanosphere lithography and plasma etching. *Royal Society of Chemistry*, 96404-96411.

Wang, Q., Yang, X., & Yang, Z. (2014). Study on Micro and Nano Structure and Superhydrophobicity for Several Typical Planing Animals Legs. *Applied Mechanics and Materials*, 551-554.

Wen, R., Xu, S., Zhao, D., Lee, Y.-C., Ma, X., & Yang, R. (2017). Hierchial Superhydrophobic Surfaces with Micropatterened Nanowire Arrays for High-Efficiency Jumping Droplet Condensaiton. *ACS Appl. Mater. Interfaces*, 44911-44921.

Why is a Lotus Rock pan so easy to clean? . (2014, April 14). Retrieved May 24, 2016, from Lotus Rock: http://lotusrock.com/why-is-a-lotus-rock-pan-so-easy-to-clean/

Wong, T.-S., Kang, S. H., Tang, S. K., Smythe, E. J., Hatton, B. D., Grinthal, A., & Aizenberg, J. (2011). Bioinspired self-repairing slippery surfaces with pressure-stable omniphobicity. *nature*, 443-447.

Wu, Y., Zhang, C., Yuan, Y., Wang, Z., Shao, W., Wang, H., & Xu, X. (2013). Fabrication of Wafer-Size Monolayer Close-Packed Colloidal Crystals via Slope Self-Assembly and Thermal Treatment. *Langmuir*, 14017-14023.

Xiao , R., Milijkovic, N., Enright, R., & Wang, E. N. (2013). Immersion Condensation on Oil-Infused Heterogeneous Surface for Enhanced Heat Transfer. *Scientrific Reports*, 1-6.

Yu, J. (2014). Fluid racheting by oscillating channel walls with sawteeth. *J. Fluid Mech.*, 305-328.

Zhang, P., & Lv, F. Y. (2015). A reveiw of the recent advances in superhydrophobic surfaces and the emerging energy-related applications. *Energy 82*, 1068-1087.

Zhu, J., Luo, Y., Tian, J., Li, J., & Gao, X. (2015). Clustered Ribbed-Nanoneedle Structured Copper Surfaces with High-Efficency Dropwise Condensation Heat Transfer Performance. *ACS: Applied Materials & Interfaces*, 10660-10665.

Appendix A

Chamber Schematics

Polycarbonate Flange

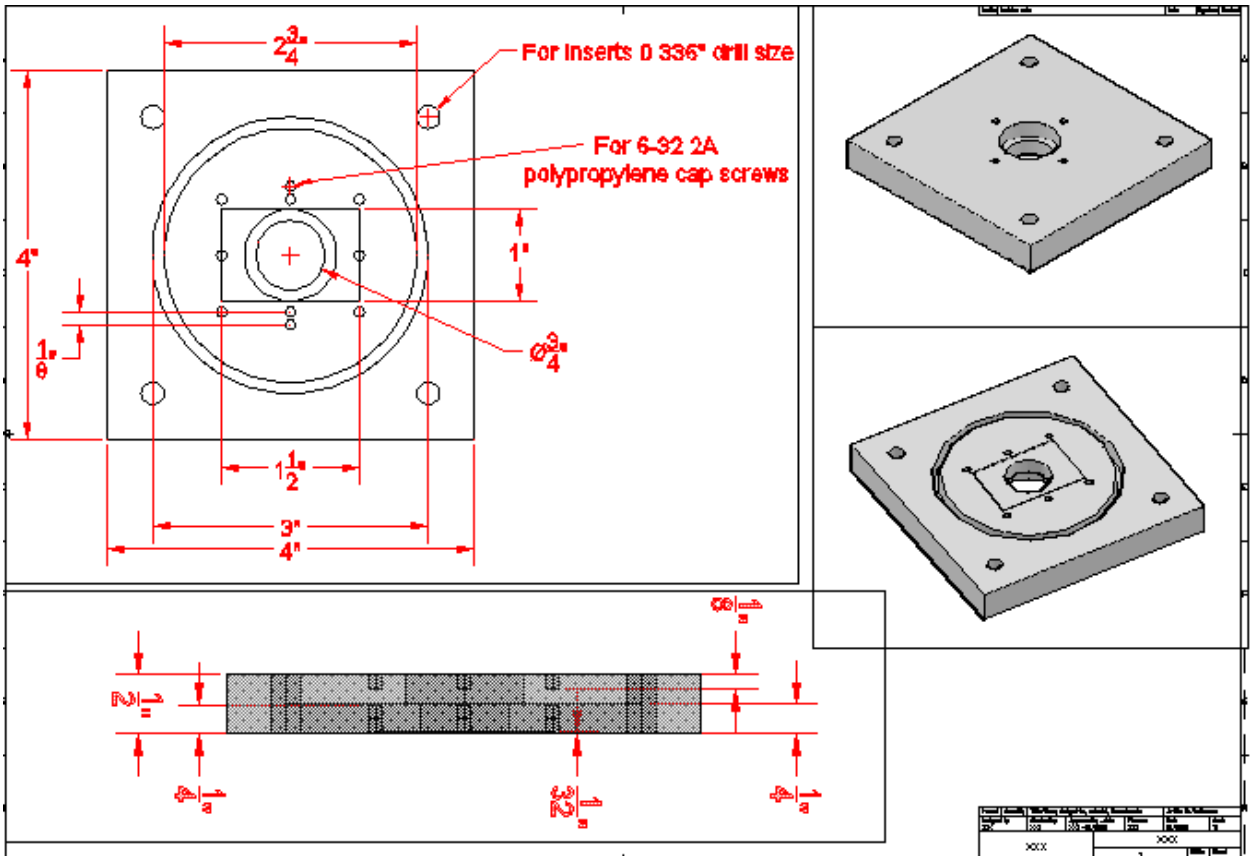

Brass Flange

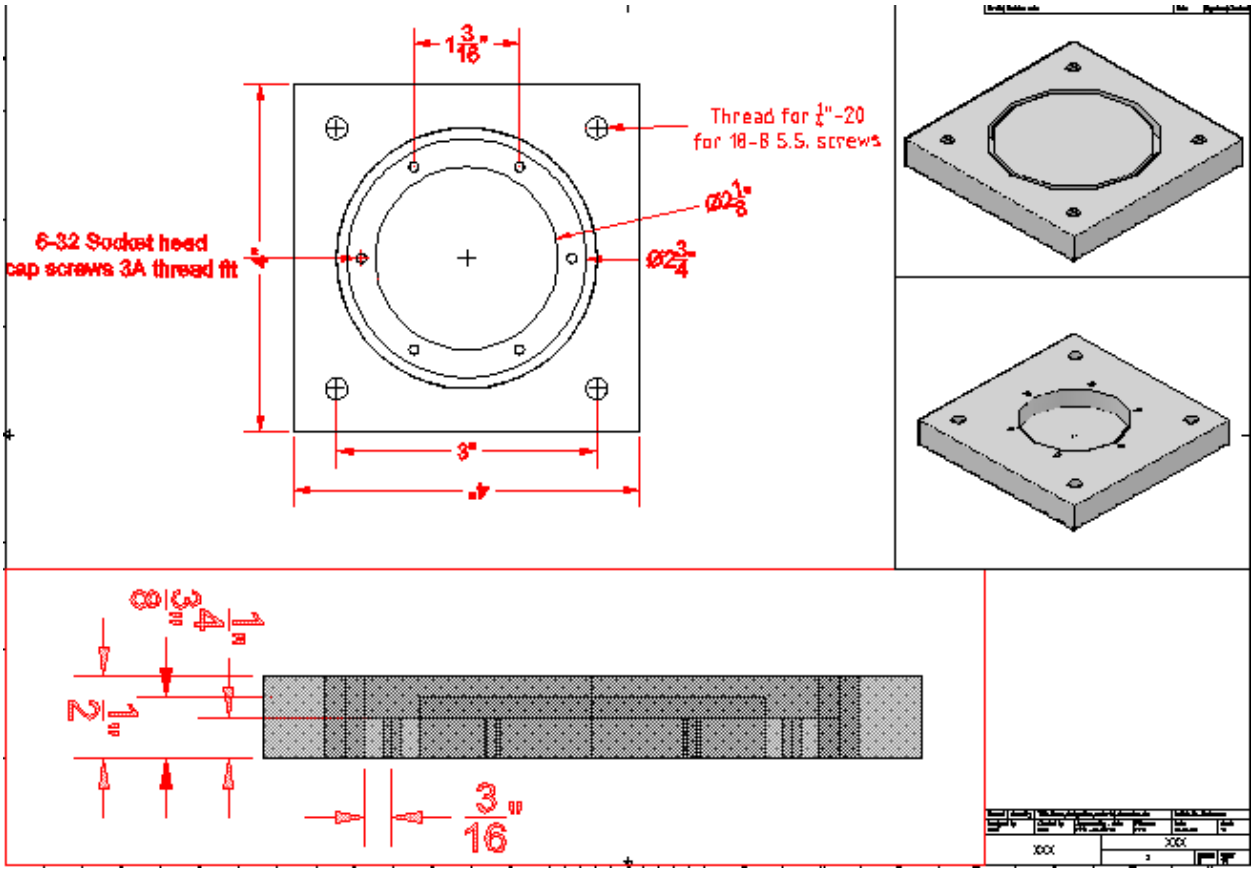

Heater Cap

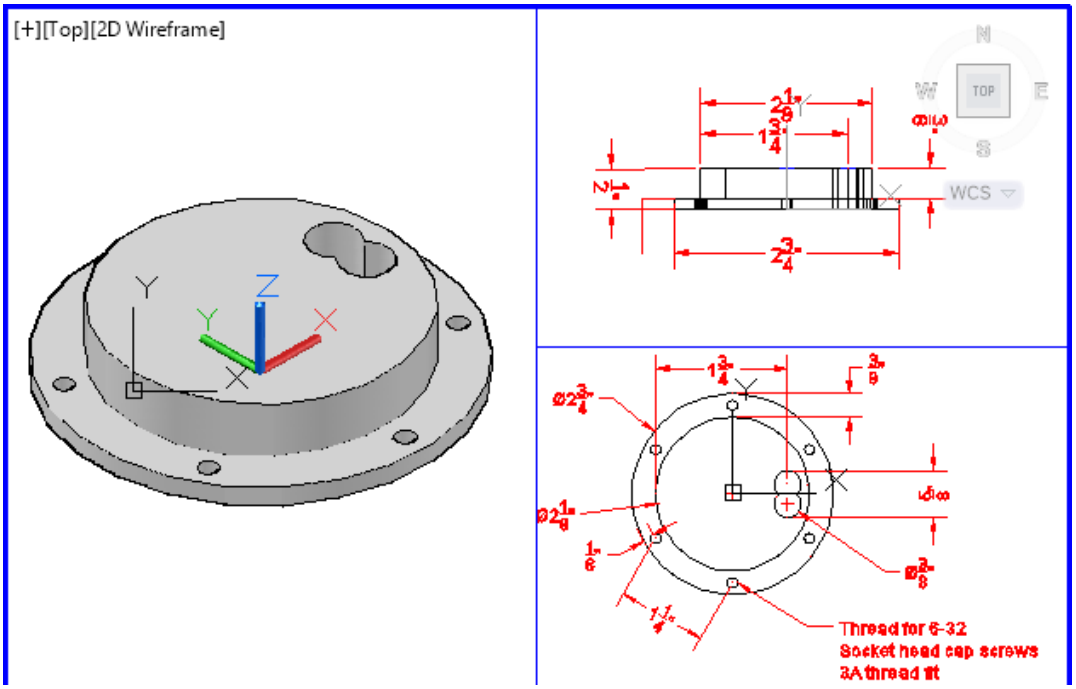

Appendix B

MatLAB codes

Image Post-processing Code: changing hue to temperature

```
clc;    % Clear command window.
clear;  % Delete all variables.
close all;  % Close all figure windows except those created by imtool.
imtool close all;   % Close all figure windows created by imtool.
workspace;  % Make sure the workspace panel is showing.
fontSize = 15;

n=65; %number of photos to be analyzed
summ=zeros(n,6); %Output matrix of averaged HSV and RGB values


for j1=1:n
j2=num2str(j1);
j3=strcat(j2,'.jpg');
rgbImage = imread(j3);

% Get the dimensions of the image.  numberOfColorBands should be = 3.
[rows columns numberOfColorBands] = size(rgbImage);

redChannel = rgbImage(:, :, 1);
greenChannel = rgbImage(:, :, 2);
blueChannel = rgbImage(:, :, 3);
% Display the individual red, green, and blue color channels.

% Generate a noisy image.  This has salt and pepper noise independently on
% each color channel so the noise may be colored.
noisyRGB = imnoise(rgbImage,'salt & pepper', 0.05);

% Extract the individual red, green, and blue color channels.
redChannel = noisyRGB(:, :, 1);
greenChannel = noisyRGB(:, :, 2);
blueChannel = noisyRGB(:, :, 3);

% Median Filter the channels:
redMF = medfilt2(redChannel, [3 3]); %output suppressed
greenMF = medfilt2(greenChannel, [3 3]); %output suppressed
blueMF = medfilt2(blueChannel, [3 3]); %output suppressed

% Find the noise in the red.
noiseImage = (redChannel == 0 | redChannel == 255);
% Get rid of the noise in the red by replacing with median.
noiseFreeRed = redChannel;
```

```
noiseFreeRed(noiseImage) = redMF(noiseImage);
meanGrayLevelRED = mean2(noiseFreeRed)

% Find the noise in the green.
noiseImage = (greenChannel == 0 | greenChannel == 255);
% Get rid of the noise in the green by replacing with median.
noiseFreeGreen = greenChannel;
noiseFreeGreen(noiseImage) = greenMF(noiseImage);
meanGrayLevelGREEN = mean2(noiseFreeGreen)


% Find the noise in the blue.
noiseImage = (blueChannel == 0 | blueChannel == 255);
% Get rid of the noise in the blue by replacing with median.
noiseFreeBlue = blueChannel;
noiseFreeBlue(noiseImage) = blueMF(noiseImage);
meanGrayLevelBLUE = mean2(noiseFreeBlue)

% Reconstruct the noise free RGB image
rgbFixed = cat(3, noiseFreeRed, noiseFreeGreen, noiseFreeBlue);


% Convert RGB fixed image to HSV
hsv = rgb2hsv(rgbFixed);

    % Extract Hue values
    h = hsv(:,:,1);

    % Extract Saturation values
    s = hsv(:,:,2);

    % Extract Brightness values
    v = hsv(:,:,3);

    % Find average of HSV values
    avgH = mean(h(:));
    avgS = mean(s(:));
    avgV = mean(v(:));

summ(j1,1:6)=[avgH,avgS,avgV,meanGrayLevelRED,meanGrayLevelGREEN,meanGrayLevel
BLUE];
end
```

Extraction of temperature contour plots and mid-plane temperature profile

The profiles represented herein were found via MatLab contour and surface plots using the Temperature matrix from the hue to temperature conversion formulas of CCD images. These images represent the near average of the data set. Each image is subdivided into contour plots, mid-plane temperature profiles and the overall temperature distribution compared to the calibrated distribution of only the LTC sheet respectively.

$$T_{vap} = 33℃$$

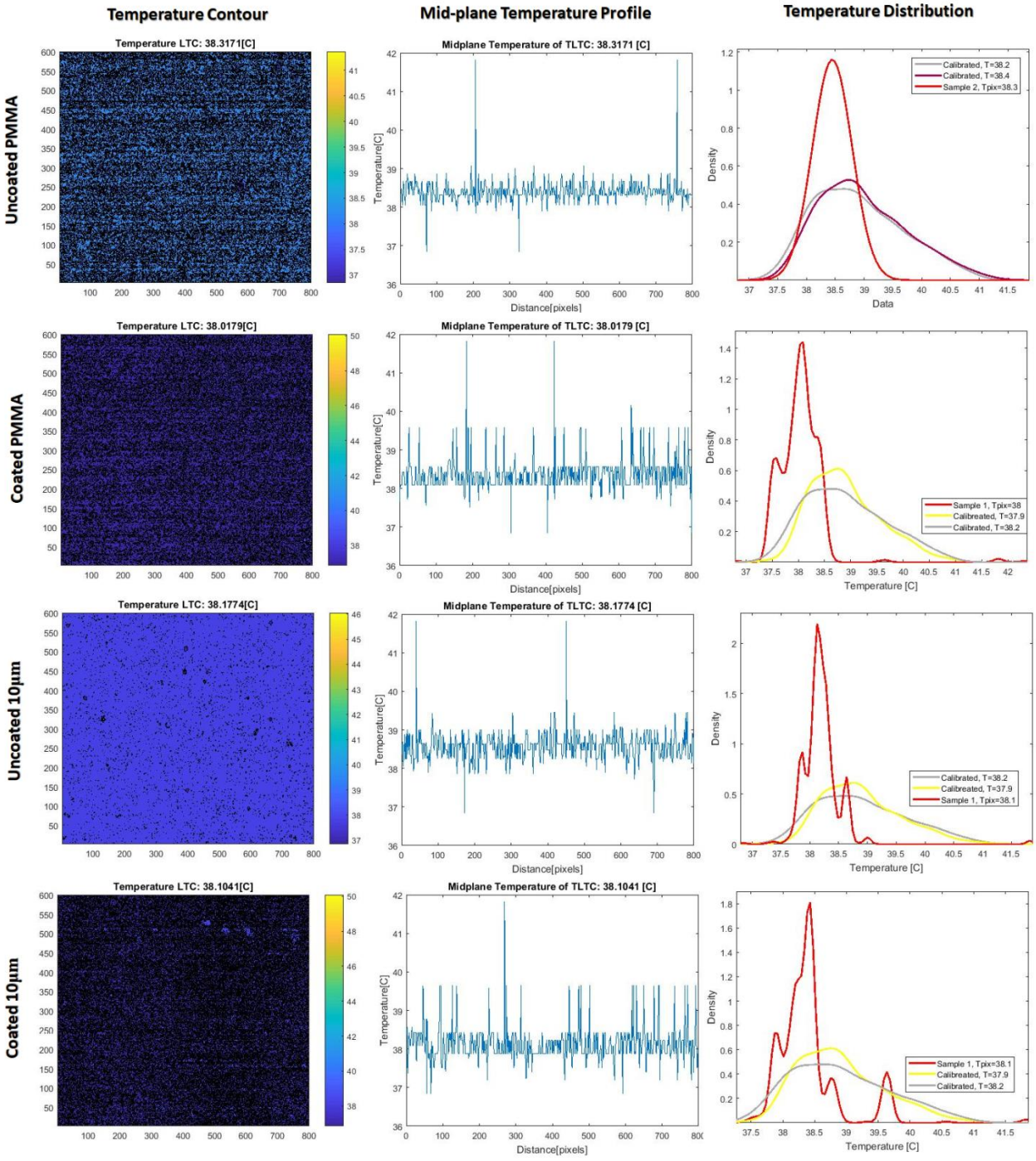
Temperature Contour
Mid-plane Temperature Profile
Temperature Distribution
Uncoated PMMA
Coated PMMA
Uncoated 10μm
Coated 10μm
Temperature LTC: 38.3171[C]
Midplane Temperature of TLTC: 38.3171 [C]
Calibrated, T=38.2
Calibrated, T=38.4
Sample 2, Tpix=38.3
Temperature LTC: 38.0179[C]
Midplane Temperature of TLTC: 38.0179 [C]
Sample 1, Tpix=38
Calibreated, T=37.9
Calibrated, T=38.2
Temperature LTC: 38.1774[C]
Midplane Temperature of TLTC: 38.1774 [C]
Calibrated, T=38.2
Calibreated, T=37.9
Sample 1, Tpix=38.1
Temperature LTC: 38.1041[C]
Midplane Temperature of TLTC: 38.1041 [C]
Sample 1, Tpix=38.1
Calibreated, T=37.9
Calibrated, T=38.2
Temperature[C]
Distance[pixels]
Density
Data
Temperature [C]

$$T_{vap} = 35℃$$

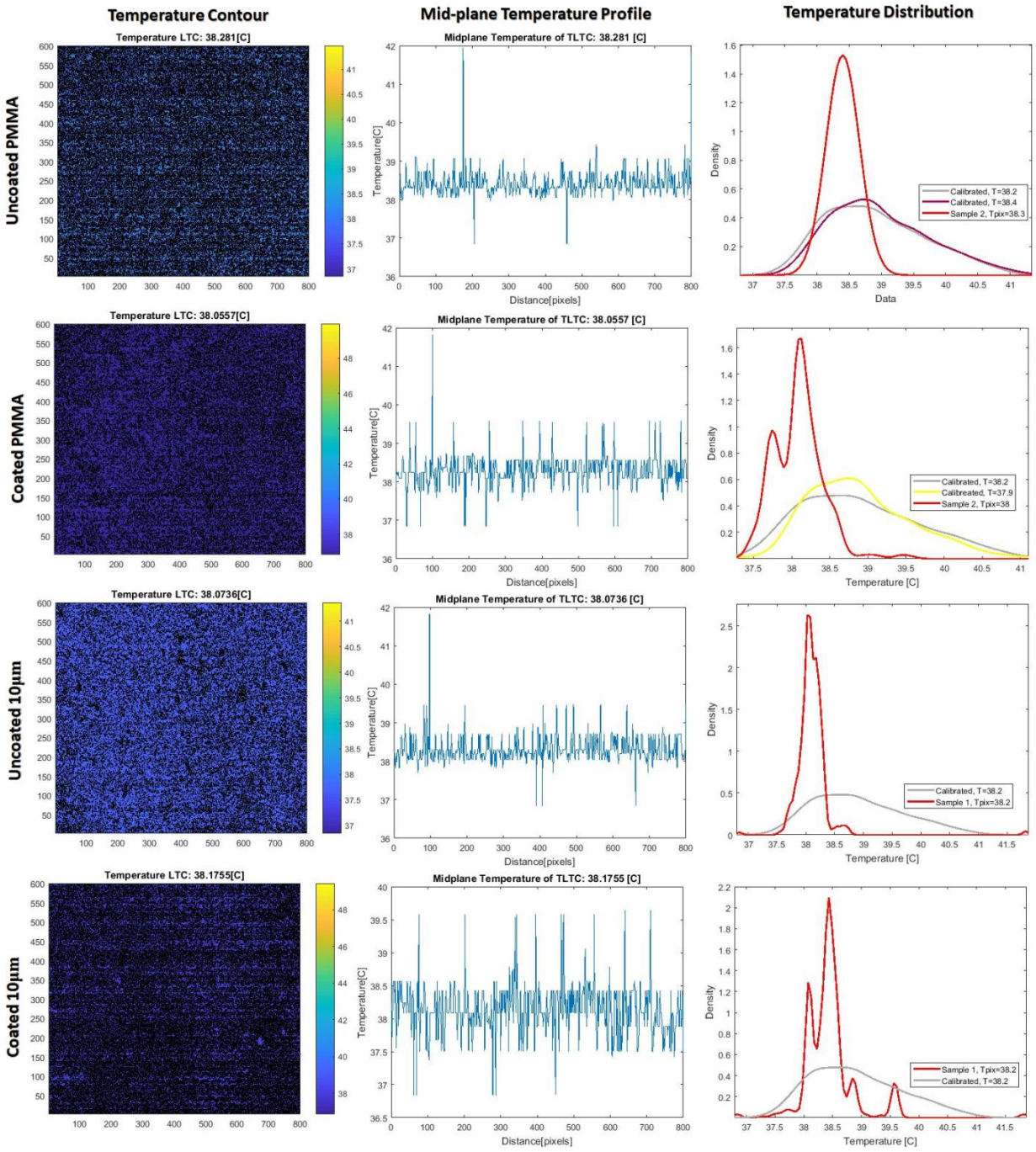
Temperature Contour
Mid-plane Temperature Profile
Temperature Distribution
Uncoated PMMA
Coated PMMA
Uncoated 10μm
Coated 10μm
Temperature LTC: 38.281[C]
Midplane Temperature of TLTC: 38.281 [C]
Temperature LTC: 38.0557[C]
Midplane Temperature of TLTC: 38.0557 [C]
Temperature LTC: 38.0736[C]
Midplane Temperature of TLTC: 38.0736 [C]
Temperature LTC: 38.1755[C]
Midplane Temperature of TLTC: 38.1755 [C]
Temperature[C]
Distance[pixels]
Density
Data
Temperature [C]
Calibrated, T=38.2
Calibrated, T=38.4
Sample 2, Tpix=38.3
Calibrated, T=38.2
Calibreated, T=37.9
Sample 2, Tpix=38
Calibrated, T=38.2
Sample 1, Tpix=38.2
Sample 1, Tpix=38.2
Calibrated, T=38.2

$$T_{vap} = 37℃$$

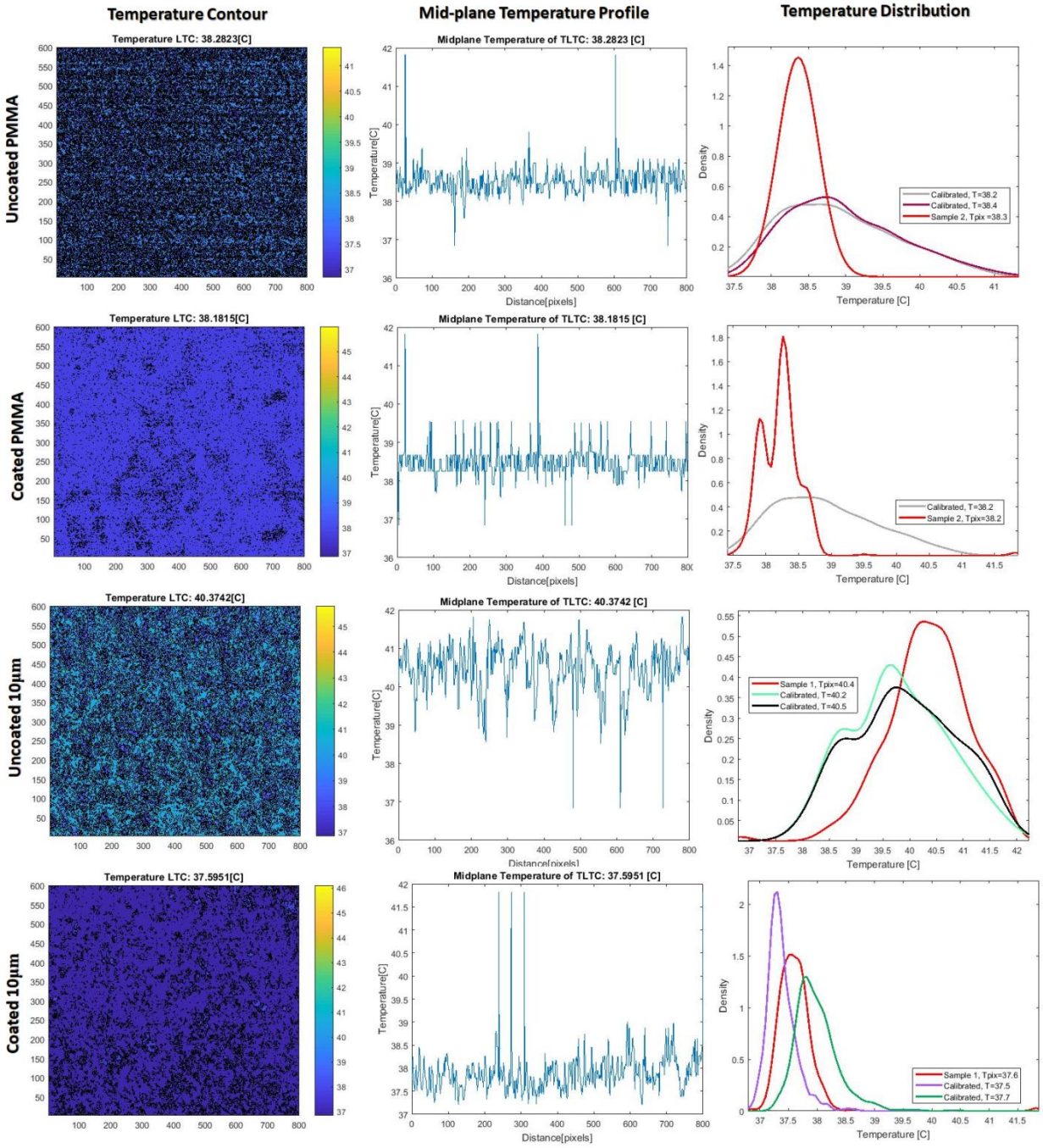
Temperature Contour
Mid-plane Temperature Profile
Temperature Distribution
Uncoated PMMA
Coated PMMA
Uncoated 10µm
Coated 10µm
Temperature LTC: 38.2823[C]
Midplane Temperature of TLTC: 38.2823 [C]
Calibrated, T=38.2
Calibrated, T=38.4
Sample 2, Tpix =38.3
Temperature LTC: 38.1815[C]
Midplane Temperature of TLTC: 38.1815 [C]
Calibrated, T=38.2
Sample 2, Tpix=38.2
Temperature LTC: 40.3742[C]
Midplane Temperature of TLTC: 40.3742 [C]
Sample 1, Tpix=40.4
Calibrated, T=40.2
Calibrated, T=40.5
Temperature LTC: 37.5951[C]
Midplane Temperature of TLTC: 37.5951 [C]
Sample 1, Tpix=37.6
Calibrated, T=37.5
Calibrated, T=37.7
Distance[pixels]
Temperature[C]
Density
Temperature [C]

$$T_{vap} = 39℃$$

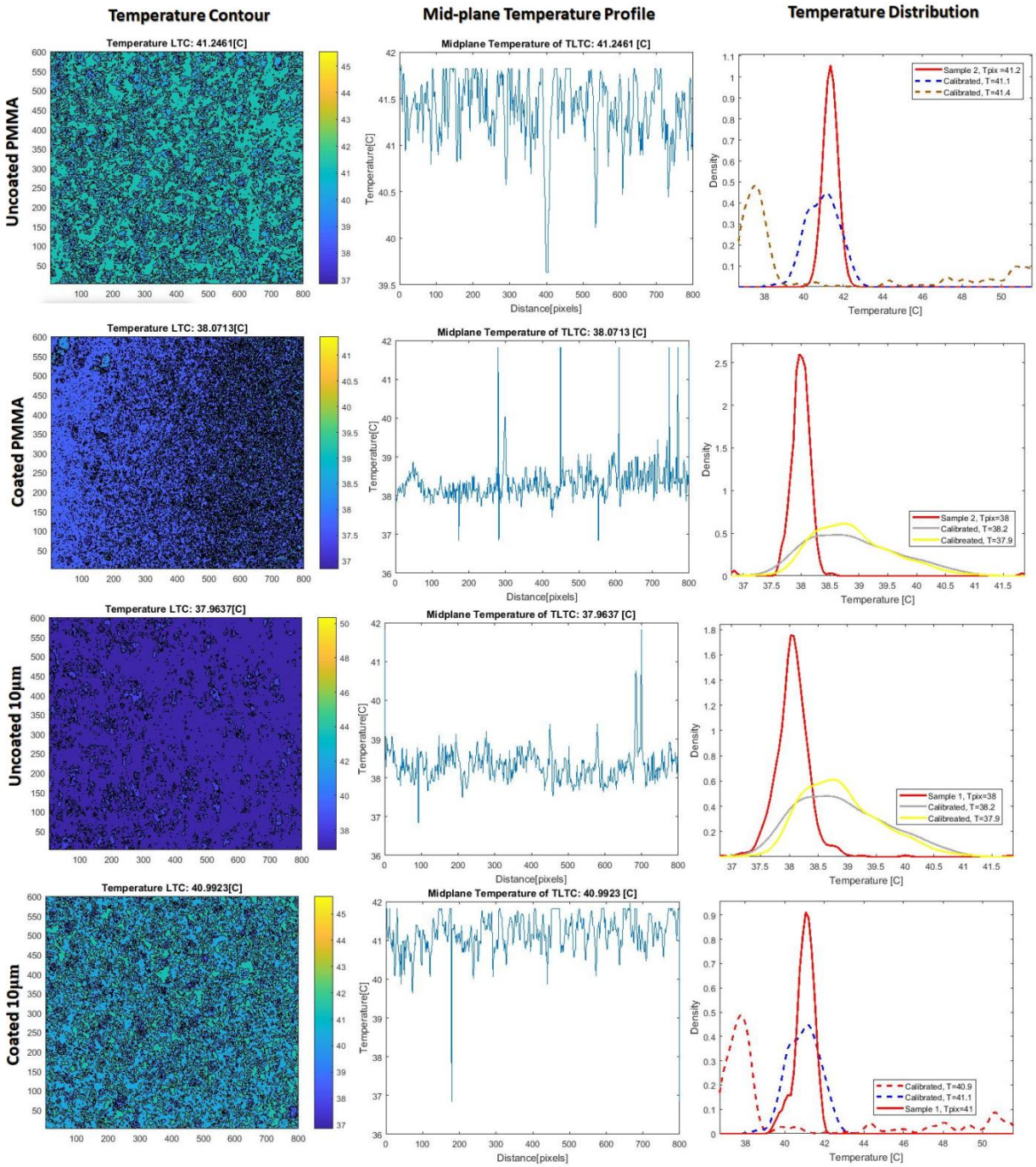
Temperature Contour
Mid-plane Temperature Profile
Temperature Distribution
Uncoated PMMA
Coated PMMA
Uncoated 10μm
Coated 10μm
Temperature LTC: 41.2461[C]
Midplane Temperature of TLTC: 41.2461 [C]
Sample 2, Tpix =41.2
Calibrated, T=41.1
Calibrated, T=41.4
Temperature LTC: 38.0713[C]
Midplane Temperature of TLTC: 38.0713 [C]
Sample 2, Tpix=38
Calibrated, T=38.2
Calibreated, T=37.9
Temperature LTC: 37.9637[C]
Midplane Temperature of TLTC: 37.9637 [C]
Sample 1, Tpix=38
Calibrated, T=38.2
Calibreated, T=37.9
Temperature LTC: 40.9923[C]
Midplane Temperature of TLTC: 40.9923 [C]
Calibrated, T=40.9
Calibrated, T=41.1
Sample 1, Tpix=41
Temperature[C]
Distance[pixels]
Density
Temperature [C]

$$T_{vap} = 41℃$$

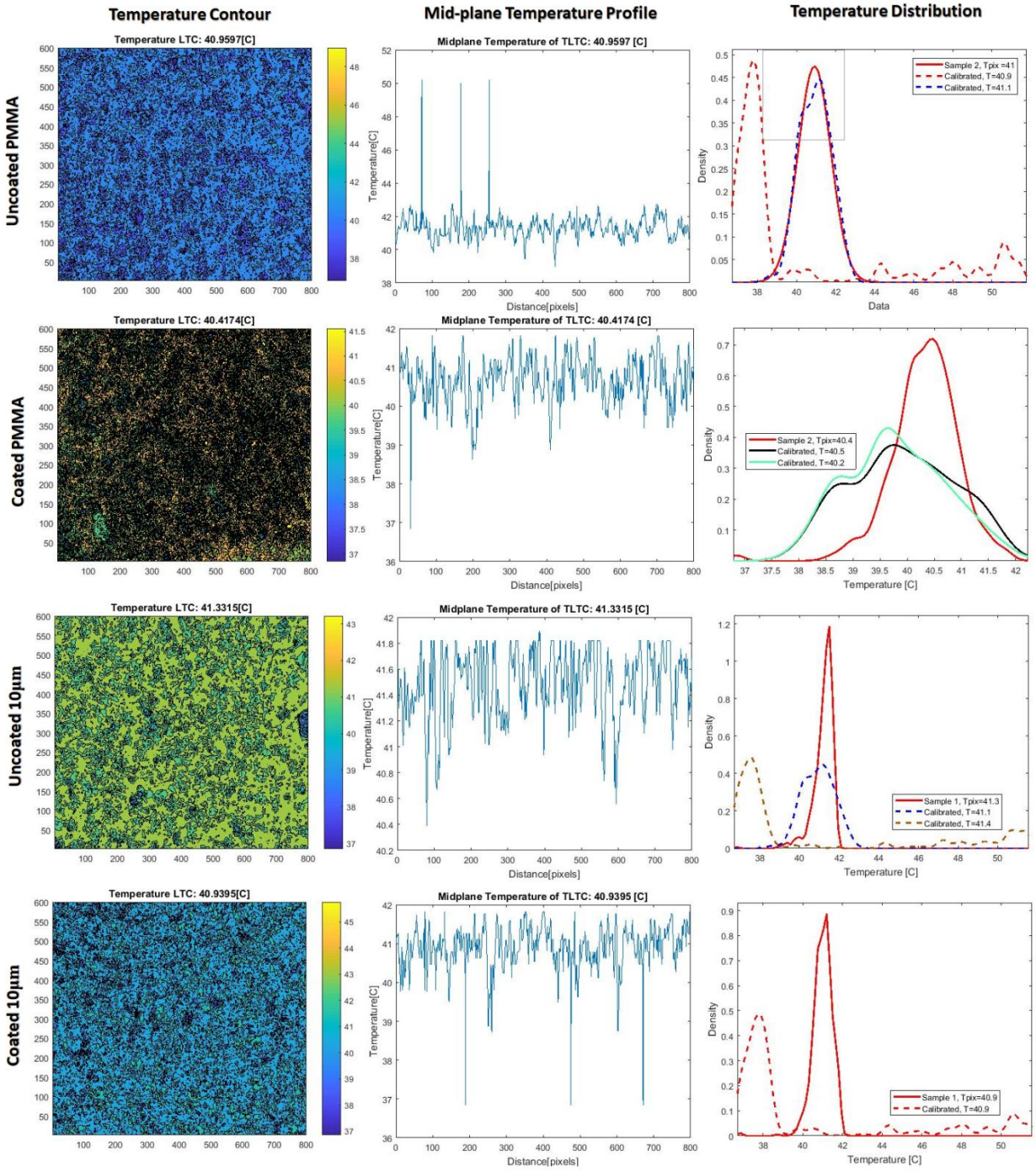
Temperature Contour
Mid-plane Temperature Profile
Temperature Distribution
Uncoated PMMA
Coated PMMA
Uncoated 10µm
Coated 10µm
Temperature LTC: 40.9597[C]
Midplane Temperature of TLTC: 40.9597 [C]
Sample 2, Tpix =41
Calibrated, T=40.9
Calibrated, T=41.1
Temperature LTC: 40.4174[C]
Midplane Temperature of TLTC: 40.4174 [C]
Sample 2, Tpix=40.4
Calibrated, T=40.5
Calibrated, T=40.2
Temperature LTC: 41.3315[C]
Midplane Temperature of TLTC: 41.3315 [C]
Sample 1, Tpix=41.3
Calibrated, T=41.1
Calibrated, T=41.4
Temperature LTC: 40.9395[C]
Midplane Temperature of TLTC: 40.9395 [C]
Sample 1, Tpix=40.9
Calibrated, T=40.9
Temperature[C]
Distance[pixels]
Density
Data
Temperature [C]

Vita

Emily Brown is a Masters candidate in the Department of Mechanical Engineering at Louisiana State University. She has been a graduate research assistant under the supervision of Dr. Sunggook Park since the Summer of 2014. She received her Bachelors of Science in Mechanical Engineering from Southeastern Louisiana University in 2014. She was raised in Schriever, Louisiana and hopes to pursue a career outside of the United States post-graduation.